An Experimental and Numerical Study of Normal Particle Collisions in a Viscous Liquid

Thesis by

Xiaobai Li

In Partial Fulfillment of the Requirements

for the Degree of

Doctor of Philosophy

California Institute of Technology

Pasadena, California

2010

(Defended May 19, 2010)

To my grandfather, Chao Hong.

Acknowledgments

This dissertation would not have been possible without the help and advice of a lot of people.

I am deeply grateful to my advisor, Professor Melany L. Hunt, who introduced me to the enchanting world of liquid-solid flows, guided me through the academic challenges with great patience and supported me consistently in every aspect of my research. She shared the happiness during my good times and gave sincere trust and encouragement during my bad times. I learned from her for being not only a good scientist but also a responsible and considerate person.

I also thank Professor Tim Colonius, who has been a great source of answers to my questions regarding numerical methods. The discussions with him by the round table in his office were enjoyable and memorable. He and his former student, Dr. Kunihiko Taira, generously shared their immersed boundary projection method computer code with me. Thank them for helping me start my numerical work from such a high level.

Sincere gratitude is extended to the other defense committee members, Professor John F. Brady and Professor Guillaume Blanquart, for taking their time to read my thesis and offering many valuable suggestions.

I am fortunate to be in a research group with an active, friendly, and open atmosphere. Thank these amiable group members, Fuling Yang, Angel Ruiz-Angulo, Erin Koos, Nathalie Vriend and Esperanza Linares for their nice comments on my research and kind assistance on my experiments.

My thanks also go to my friends, Ling Zheng, Yi Liu, Jie Cheng, Li Liu, Bo Li, Yue Zou and Yong Hao for sharing my joy and sadness, and offering instant help whenever needed. I treasure every minute I have spent with them.

Finally, I save my greatest appreciation to my family members, my wonderful husband Xiaosong,

lovely daughter Isabelle, perfect parents and parents in-laws. I would never have made it this far without their unconditional love and consistent support. Thank them for more than I can ever say.

Abstract

When two solid bodies collide in a liquid environment, the collision process is influenced by viscous effects and the increased pressure in the interstitial liquid layer between the two solid boundaries. A normal collision process is investigated for a range of impact Stokes numbers using both experimental and numerical methods. Experiments of a steel sphere falling under gravity and colliding with a Zerodur wall with Stokes number ranging from 5 to 100 are performed, which complement previous investigations of immersed particle-wall collision processes. The incompressible Navier-Stokes equations are solved numerically to predict the coupled motion of the falling particle and the surrounding fluid as the particle impacts and rebounds from the planar wall. The numerical method is validated by comparing the numerical simulations of a settling sphere with experimental measurements of the sphere trajectory and the accompanying flow-field. A contact model of the liquid-solid and solid-solid interaction is developed that incorporates the elasticity of the solids to permit the rebound trajectory to be simulated accurately. The contact model is applied when the particle is sufficiently close to the wall that it becomes difficult to resolve the thin lubrication layer. The model is calibrated with measured particle trajectories and is found to represent well the observed coefficient of restitution over a range of impact Stokes numbers from 1 to 1000. In addition, the model is modified to simulate the normal collision of two spheres. The effective coefficient of restitution obtained from the simulation shows a strong dependence on the binary Stokes number accordant with other researcher's experimental results. The unique behaviors of the two spheres at low binary Stokes number including target motion prior to contact and group motion after collision are simulated by the current work.

Contents

List of Figures

List of Tables

Chapter 1

Introduction

1.1 Background and Motivation

Liquid-solid flows are involved in a wide variety of geophysical and industrial processes, including nearshore sediment transport, debris surges and landslides, the handling of dredging slurries and hydraulic fracture technologies (see Crowe *et al.*, 1998*a*; Lorenzini & Mazza, 2004). These flows are heterogeneous and the macroscopic behavior of the mixture is not adequately described by continuum theories. The rheology of liquid-solid mixtures depends on many factors, including the hydrodynamic forces, inter-particle interactions, the volume fraction, gravity, and the size and shape of the particles.

Particle-particle and particle-wall collisions play an important role in a liquid-solid flow because they affect particle accumulation and dispersion, and interphase transport and mixing. Compared to a dry collision in which the fluid resistance is negligible and the particle inertia is dominant, the kinetic energy of a particle in a liquid environment is dissipated by viscous stresses in the liquid and by inelasticity during collision. The ratio of particle inertia to viscous forces is quantified through the Stokes number, $St = \frac{1}{9}(\rho_p/\rho_l)Re$, where $Re = \rho_l DU/\mu$ is the particle Reynolds number based on impact velocity U, the particle diameter D, the liquid viscosity μ, and ρ_p and ρ_l are the density of the particle and the liquid, respectively.

By simultaneously accounting for elastic deformation and viscous forces, Davis, Serayssol & Hinch

(1986) established the range of conditions for deformation and rebound of colliding spheres. They found that elasticity of the particle and the impacting surface influences the value of coefficient of restitution, e, defined as the ratio of the rebound to impact velocity. However, the Stokes number determines whether there is a rebound and the trend of e. By measuring the approach and rebound of a particle colliding with a wall in a viscous fluid, Joseph *et al.* (2001) presented the coefficient of restitution as a function of the Stokes number. Below a Stokes number of approximately 10, no rebound of the particle occurs. At a Stokes number greater than 1000, the particle rebound speed is not affected by the surrounding fluid. Hence, the coefficient of restitution, e, increases from 0 at $St \approx 10$ to a dry value, e_d, which occurs for a collision with negligible fluid resistance. In their pendulum-wall collision experiments, they observed a velocity decrease prior to contact as the result of the presence of the wall. The dependence of the coefficient of restitution on the Stokes number was also presented in the work by Gondret *et al.* (2002); in this study, the authors measured the normal trajectory of the particle over multiple bounces. However, they did not observed the velocity decrease as the particle approaches to a horizontal wall under gravity. The work by Joseph & Hunt (2004) examined the oblique collisions between a particle and a wall. Later work by Yang & Hunt (2006) measured the coefficient of particle-particle collisions in a liquid and found a similar dependence on particle Stokes number. However, for Stokes numbers less than approximately 20 the authors observed that the target particle moved prior to impact due to the increase in hydrodynamic pressure as the impacting particle approached within a half a particle diameter.

Computational studies have also considered the problem of particle collisions in a liquid. By fixing the particle velocity at a constant value as it approaches a wall, Leweke, Thompson & Hourigan (2004) computed the flow generated by a particle colliding normally to a surface without rebound; these simulations showed the development of the vortex rings around the particle over a range of Reynolds numbers. TenCate *et al.* (2002) simulated a sphere settling toward a solid wall without rebound and compared with experiment results. Both the spatial structure and the temporal behavior of the flow field were obtained. Ardekani & Rangel (2008) proposed a collision strategy that assumed no liquid is present between the two solid surfaces at collision and used the dry coefficient of

restitution e_d to calculate the instant rebound velocity directly when the distance between particles becomes equal to particle surface roughness height, $h_{\min}$, of order $1\mu m$. To resolve the flow at the length scale of $h_{\min}$, a finer mesh is used near the contact region; the simulation results depend on the mesh size and $h_{\min}$. Their model neglects the elastic deformation of the particles, which occurs over lengths that are comparable with the roughness height according to the elastohydrodynamics analysis in Davis *et al.* (1986).

While extensive work has been done independently, a complete description of an immersed collision process is not readily available. Such a description would include accurate solution of the flow filed, the interaction between the solid particle and the surrounding liquid, and the rebound trajectory of the impact particle. A better understanding of the bulk behavior of a liquid-solid flow would depend critically on such an exact description on a single collision scale. Moreover, a contact model is required to reveal the contact mechanism so that a flow with many particles can be simulated with a simplified contact strategy. The work presented in this thesis provides a first step toward that goal.

1.2 Thesis outline

The primary goal of this thesis is to investigate the collision between two solid surfaces when the effect of the surrounding liquid is non-negligible. Chapter 2 describes the experiments performed for a solid sphere falling under gravity and colliding with a solid wall. The detailed velocity profile before the sphere contacts the wall is presented by using a higher frame rate for the recording camera than used in some previous studies. The coefficient of restitution measured from the experiments are presented as a function of the Stokes number. Chapter 3 introduces the numerical method employed in the current simulations. Chapter 4 presents a contact model for a particle-wall collision based on the hydrodynamic forces and the elastic force on an impact sphere. In Chapter 5, the simulations for an individual particle-wall collision in a viscous liquid are examined with the measured results from the current experiments. The coefficient of restitution calculated from the simulations are compared with the experimental data and the other researchers' result. In Chapter 6, the proposed contact

model is modified to simulate an immersed collision between two solid spheres. The unique sphere behavior before and after a collision at low Stokes numbers are presented. The effective coefficient of restitution and the binary Stokes number are correlated, and the dependance between them is compared with the other researchers' results. Conclusions are summarized in Chapter 7, and the future work is discussed in brief.

Chapter 2

Experiments

One of the first experiments involving a particle colliding with a stationary wall in a viscous liquid environment was performed by McLaughlin (1968) who found that the rebound trajectory was shown to depend on the particle impact Reynolds number. His experiments, however, were performed over a small range of Reynolds numbers. Barnocky & Davis (1988) dropped solid particles of a few millimeters in air onto a solid plate that was covered by a thin liquid layer (about $0.1 \sim 0.5$ mm thick) and observed if the particles rebounded or not. To ensure a rebound, the sphere needs to possess sufficient inertia to overcome the hindering fluid effect for a non-zero velocity upon contact. As the viscosity and the thickness of the liquid layer was increased, a greater critical drop height was need for the occurrence of a particle rebound. They did not measure the coefficient of restitution above the transition but obtained a critical Stokes number for rebound, St_c, from approximately 0.25 to 4 for smooth surfaces. Lundberg & Shen (1992) studied the dependence of the coefficient of restitution upon the fluid viscosity for the collision of a roller attached to a pendulum with a fixed ball covered by a thin layer of viscous oil. They found that for oil with moderate values of viscosity to 0.01 Pa·s, the restitution coefficient is similar to that in a dry collision. However, at higher values of viscosity, the restitution coefficient can become much less. This dependence on viscosity is stronger for softer material where the surface deformation is larger, resulting in an increased contact surface area and thus higher effect of the viscous dissipation. Zenit & Hunt (1999) and Joseph *et al.* (2001) investigated the collisions totally immersed in a viscous fluid with a pendulum-like apparatus that permits a horizontal impact motion towards a vertical wall. A critical Stokes number, $St_c = 10$, for

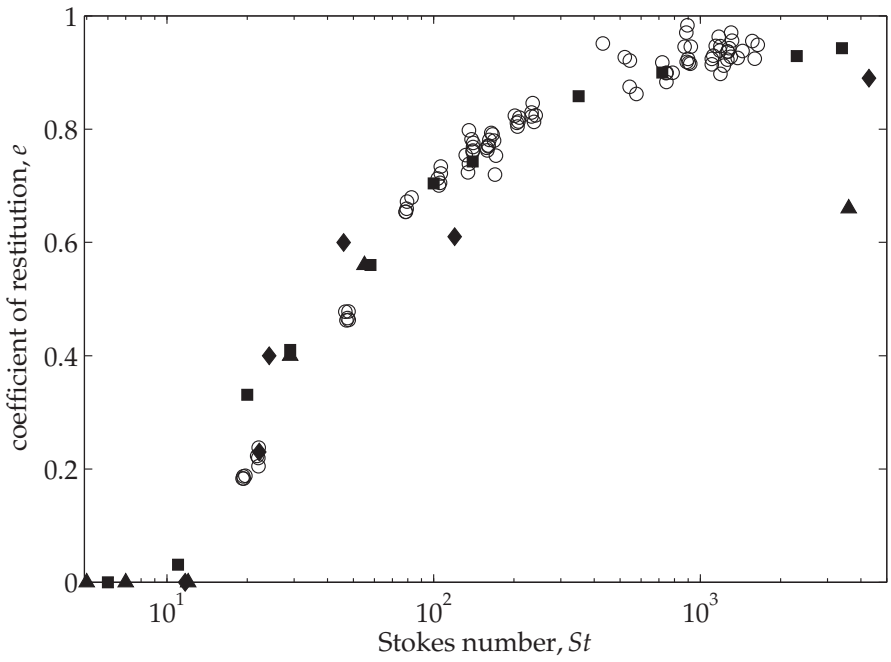

Figure 2.1: Coefficient of restitution, e, as a function of Stokes number. 'o' for steel particles impacting a Zerodur wall in Joseph *et al.* (2001); '♦' for steel ball bearings impacting an anvil in McLaughlin (1968); '▲' and '■' for steel spheres impacting a glass wall in Gondret *et al.* (1999) and Gondret *et al.* (2002).

the bounce transition was observed. The surface roughness of the materials was found to impact the value of coefficient of restitution for $St < 80$. Gondret *et al.* (2002) performed similar experiments to McLaughlin's using a solid sphere falling under gravity in a fluid onto a solid wall. The dependence of the coefficient of restitution upon the particle Stokes number showed similar trend with McLaughlin (1968) and Joseph *et al.* (2001)'s results, as shown in figure (2.1) which is taken from figure (3.7) of Joseph (2003).

For collisions with high Stokes number, the viscous force is small compared with the particle inertia, resulting in a near unity coefficient of restitution. The small value (around 0.7), as shown by the filled triangle at Stokes around 4000, is a result from Gondret *et al.* (1999) who claimed 3 years later that 'the point appears to be underestimated due to the previous data analysis which has been proved to be too crude for high St' (see Gondret *et al.*, 2002) With decreasing Stokes number, the coefficient of restitution drops from unity. When the Stokes number is smaller than a critical value, a restitution coefficient is zero, indicating no rebound happens, at least within the experimental

resolution of the image acquisition system.

The aforementioned experiments mainly focused on coefficient of restitution based on the behavior of a particle right before and after it collides with a wall. In Joseph *et al.* (2001) pendulum experiments, the trajectory and velocity profile were obtained. However, the surrounding flow field coupled with the pendulum motion of the sphere was three dimensional and computationally expensive to be simulated. Gondret *et al.* (2002) presented the rebound trajectory and velocity of a particle falling under gravity and colliding with a wall, which resulted in axisymmetric surrounding flow field; however, the initial trajectory of the particle after it is released was not included. In the experiments performed by TenCate *et al.* (2002), the whole process of a sphere settling toward a wall was recorded. The sphere was released from zero velocity while simultaneously triggering the camera to start filming until the sphere rested on the wall. The experimental results allowed the validation of a solution for the surrounding flow field which is directly coupled with the motion of the sphere during a settling process as described in Chapter 3. However, TenCate *et al.* (2002) did not include results for Stokes numbers greater than the critical value.

Thus, new experiments were performed to record a complete collision process in a viscous liquid including the trajectory of a particle as it accelerates from zero velocity after release, collides with a wall, rebounds and falls again until it comes to rest. The new experimental results provide a calibration for a proposed contact model described in Chapter 4 which captures the collision and rebound processes. Moreover, the experimental trajectories of the collisions with different Stokes numbers are compared with the simulated results. A detailed description of the motion of a particle especially when it is about to collide with a wall is obtained by using a CCD camera with a higher frame rate.

2.1 Experiment setup

2.1.1 Experiment apparatus

The experiment setup is shown schematically in figure (2.2). The experiments are performed in a glass rectangular tank with length×width×height as $600 \times 350 \times 450$ mm that contains a mixture of glycerol and water. A steel sphere with diameter $D = 9.5$ mm is dropped from an electromagnetic release mechanism that is fixed on the top of the tank. A trigger pad is used to cut off the current in the electromagnetic mechanism releasing the steel sphere from zero velocity under quiescent ambient fluid condition. The circular release surface with diameter 52 mm is immersed in the liquid a certain depth (> 50 mm) under the free surface of the liquid, and the effect of the liquid free surface on the experiment is ignored. A cylinder-shaped Zerodur block with diameter 150 mm and height 100 mm is placed coaxially below the release mechanism from a certain distance as a target wall. Zerodur is a hard glass-like material and it can be polished to a high accuracy to minimize the effect of wall roughness on the experiments. A level is used to make sure the top surface of the Zerodur is horizontal. The release surface is kept parallel to the top surface of the Zerodur block. The sphere is dropped from the center of the release surface and falls along the axis of the Zerodur block. The dimension of the glass tank is large compared with the sphere diameter so that the flow field around the moving sphere can be considered as axisymmetric as long as the particle Reynolds number $Re = \frac{DV}{\nu}$ is less than 250. Moreover, the large dimensions of the tank allow the use of the far field boundary condition in the following simulation.

A high speed videography system (a high speed camera, a control/display monitor and a record trigger) is used to capture the particle dynamic behavior. Figure (2.3) shows an example image on the monitor with a control menu on the right. The camera frame rate is set to be 4000 frames per second so that the time interval between two successive frames is 0.25 ms. Under this frame rate, the resolution is 160 pixels wide by 140 pixels high. More details of the motion of a particle, especially when it is about to collide with the wall, can be obtained by using this higher frame rate. The shutter speed is 1× which allows the camera to capture as much light as possible. The filming

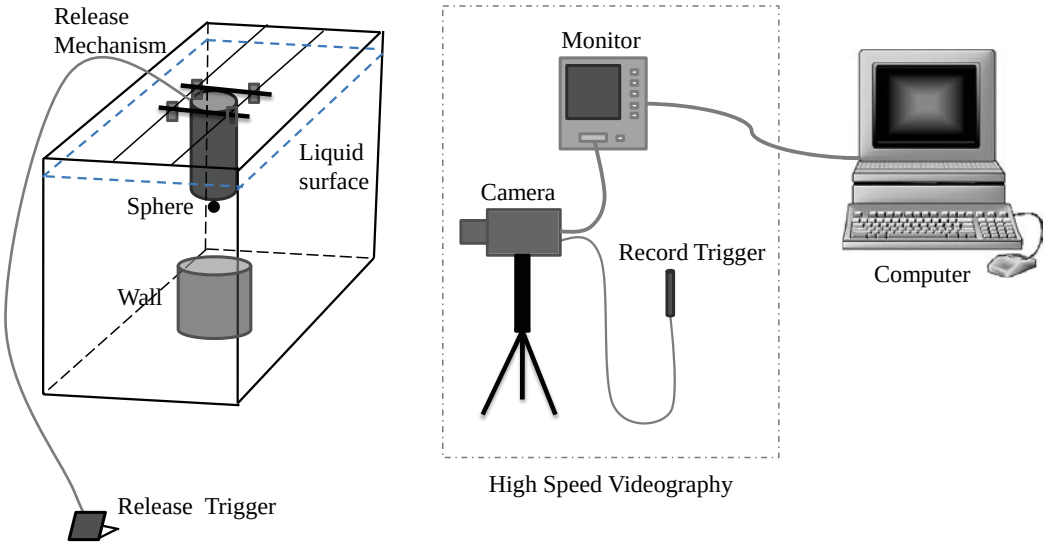

Figure 2.2: Schematic experiment setup

starts prior to the release of the sphere to avoid missing the initial part of the collision process since the release pad and the record trigger are controlled manually and separately. During playback, the frame rate is set at 30 frames per second because this is the rate at which MATLAB can digitize a video. The video recorded by the videography system is transferred into a computer as an output '.avi' file by using software 'VirtualDub' which captures the video playing on the control/display monitor.

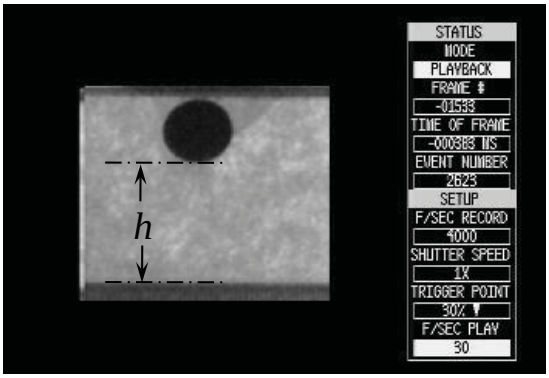

Figure 2.3: The image shown on the control/display monitor. h is the gap between the sphere and the wall.

2.1.2 Material properties

Steel spheres with diameter 9.5 mm are used in the experiments. The target wall is made of Zerodur. The properties of the solid material are listed in Table (2.1) including solid density, ρ_p, Young's modulus, E, Poisson's ratio, ν.

Material	ρ_p(kg/m^3)	E(GPa)	ν
steel	7780	200	0.33
Zerodur	2530	91	0.24

Table 2.1: Properties of the sphere and the wall used in the collision experiments

Aqueous glycerol solutions were used as the surrounding fluid for the experiments. Glycerol is completely miscible with water, which allows for a large range of viscosities to be explored by changing the mixture proportions. Also, the viscosity of the mixture varies significantly with temperature. Therefore, the liquid temperature is measured before each collision by a digital thermocouple thermometer. The apparent specific gravity of the liquid is measured by a hydrometer. Based on the measured temperature and apparent specific gravity, the concentration of the mixture can be found from the datasheets presented in Joseph (2003) that are readily available at Dow Chemical Synthetic Glycerin Products. Finally, the density and the viscosity of the liquid can be found from the datasheets based on the temperature and the concentration.

2.2 Experimental data process

The output video '.avi' file is first converted into DivX format by using software 'YasaVideoConverter'. The size of the video after conversion is much smaller (about 40 times) than the original one, but the quality is good. Then this DivX video can be read by MATLAB at a frame rate 30 fps and converted into images in '.jpg' form. Figure (2.4) presents the images extracted from a recorded video for event 2623. The time interval between the successive images shown in the figure is 34.25 ms. In figure (2.4), (a) shows the initial state in which the velocity of the particle just starts to fall and the flow field is static; (b) shows the particle moving under gravity towards the wall at a distance from the release surface; (c) is the moment when the particle collides with the wall and the distance

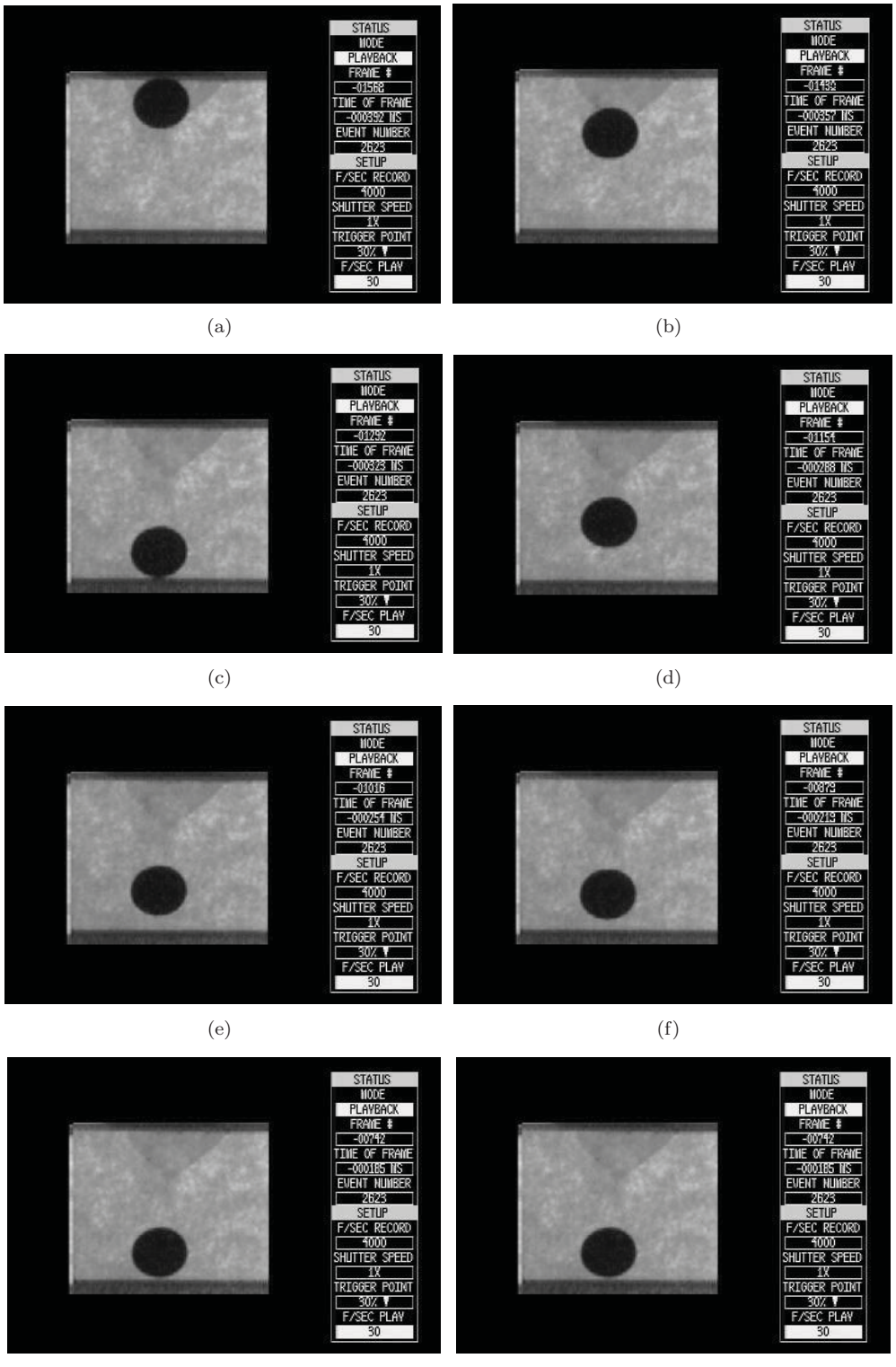

Figure 2.4: Images extracted from the recorded video

between the particle and the wall is zero; (d) shows the particle rebounding and approaching the maximum height; (e) shows the particle falling again toward the wall; (f) is the particle reaching the maximum height during the second rebound; (g) and (h) show the particle settling toward the wall and resting there.

To find the trajectory of a sphere, the images are analyzed with a template matching method that is widely used in digital image processing for finding incidence of a pattern or object within an image. For a single image, a region typically recognized as the sphere is manually cropped and saved as a template $T(x_t, y_t)$ where (x_t, y_t) represent the coordinates of each pixel in the template; then, the center of this template is moved over each point (x, y) in the image, and the normalized cross-correlation is calculated as

$$\frac{1}{n-1}\sum_{x,y}\frac{(F(x,y)-\bar{F})(T(x,y)-\bar{T})}{\sigma_T\sigma_T}$$

where n is the number of pixels in the template T and a subimage F. The position with the highest result is the best match and is considered as the position of the center of the sphere in the image. Applying this technique to a series of images (the same template can be used for images extracted from one video), the trajectory of the sphere can be found by relating the position of the sphere to the corresponding time for each image. For an example, the trajectory of the sphere in event 2623 is plotted in figure (2.5). The images shown in figure (2.4) are marked on the trajectory correspondingly. The position of the sphere plotted on the figure is the result of the position of the sphere center found from the above template matching technique minus the radius of the sphere. The unit is converted from 'pixel' to 'mm' by letting the template pixel correspond with the diameter of the sphere.

The velocity of the sphere calculated as the time derivative of the trajectory $\triangle h/\triangle t$ between the two successive images is plotted in figure (2.6). Large variations are obtained since the time interval 0.25 ms is small (compared with 2 ms in the experiments of Gondret *et al.* (2002) and 5∼10 ms in Joseph *et al.* (2001)), which amplifies the uncertainty of the experiment. Several steps have been

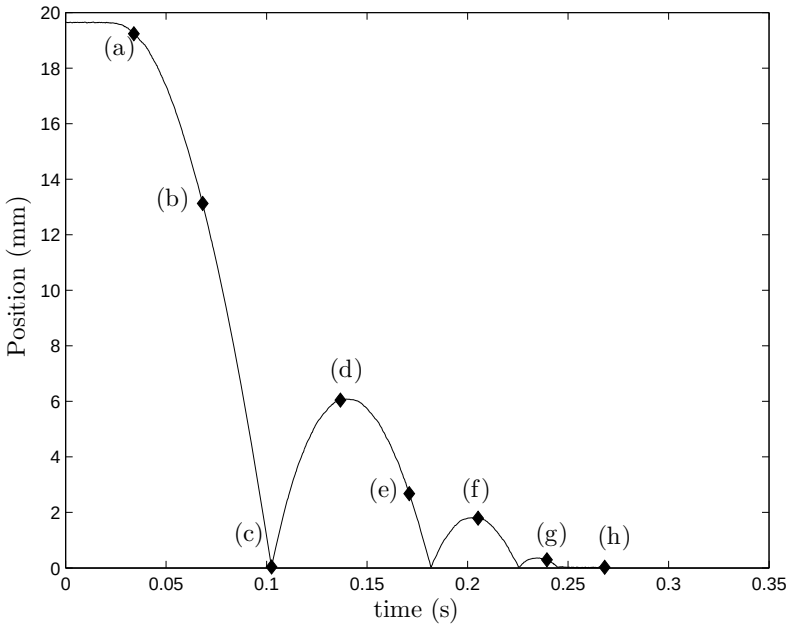

Figure 2.5: The trajectory of the sphere in event 2623. The diamond points show the corresponding position for the images in figure (2.4).

taken to diminish the vibration. First, for each collision process, the measurements were done three times which means that under the same condition, the sphere was dropped three times and three videos were recorded. The final trajectory is the average of the three trajectories obtained from the three videos. Then, for this averaged trajectory, when using the time derivative $\triangle h/\triangle t$ with $\triangle t = 2$ ms, the calculated velocity is much smoother, shown as the points in figure (2.7). An alternative is to fit the averaged trajectory with a high order (6th order) polynomial, $h = P(t)$, which keeps the characteristic shape of a trajectory but removes outlying points. Then, the velocity can be obtained by differentiating the polynomial and calculating the differential $V = \frac{dh}{dt}$ at different time step. The result of the alternative is shown by the lines in figure (2.7). Compared with the results given in Gondret *et al.* (2002)'s paper, the velocity profile in figure (2.7) shows not only the velocity of a sphere when it is about to collide with a wall and rebound, but also the acceleration process from zero initial velocity.

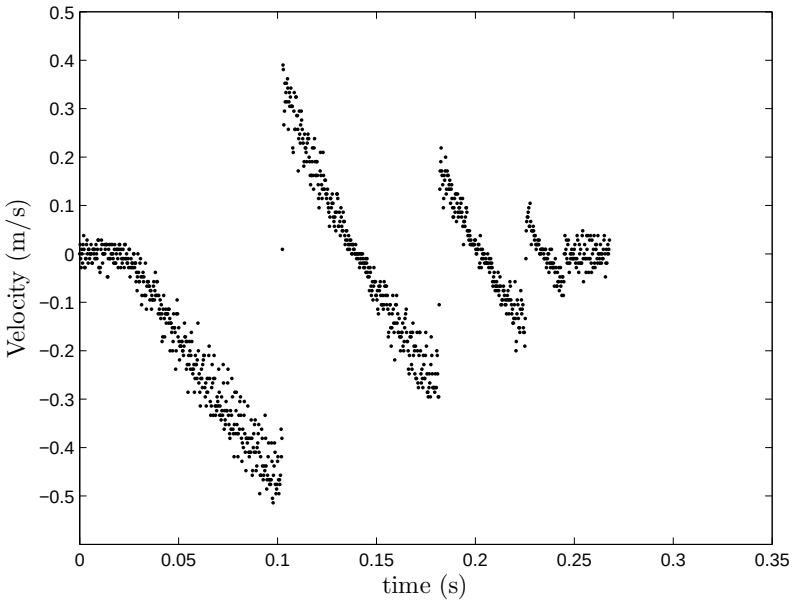

Figure 2.6: The velocity of the sphere in event 2623 calculated by using central difference of the trajectory with time interval 0.25 ms.

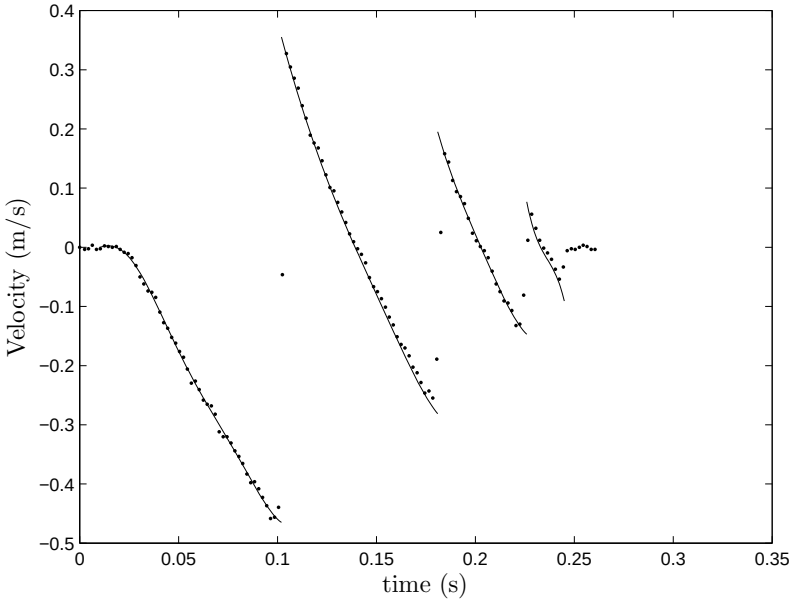

Figure 2.7: The velocity of the sphere in event 2623 calculated by using central difference of the trajectory with time interval 2 ms represented by points; the velocity profile calculated by fitting the experimental trajectory with polynomials represented by lines.

2.3 Experimental results

Collisions with different impact Stokes numbers were performed by placing the wall at different distances from the release surface. The apparent specific gravity of the liquid and the room temperature are measured for each experiment. A typical value of the apparent specific gravity is 1.205 when the room temperature is 20^oC. Thus, the concentration of the mixture is found to be 78% glycerol by weight, and the corresponding density and the viscosity of the liquid for that experiment are 1203 kg/m^3 and 50.2×10^3 Pa·s. After applying the above data process techniques, the trajectory and velocity of a sphere are obtained for each collision. The impact Reynolds number $Re = \frac{DV}{\nu}$ is calculated based on the impact velocity of the sphere which is the averaged value of the velocity obtained from the differential of the fitting polynomial over the 2 ms before collision. Because of the small values of $h(t=0)/D$, where h is the gap between the particle and the wall as defined in figure (2.3), the particle does not achieve its terminal velocity before it contacts the wall. Thus, the particle Reynolds number is related to the fall distance. The Stokes number of each collision, $St = \frac{1}{9}\frac{\rho_p}{\rho_l}Re$, is the particle Reynolds number times a constant (approximately 0.7) since the density ratio of the sphere and the liquid is a constant.

A listing of the experimental cases and associated parameters are given in Table (2.2). In all the cases, the particle bounced at least twice. The impact Stokes number for each first collision was larger than 10. The maximum height achieved in the rebound motion is lower than the initial height, which is the result of viscous losses and inelasticity.

Case	$h(t=0)$	$h(t=0)/D$	Re_I	St_I	Re_{II}	St_{II}	Re_{III}	St_{III}	Re_{IV}	St_{IV}
1	5.5mm	0.58	53	38	26	19	9	7	-	-
2	10.5mm	1.10	75	54	39	28	20	15	-	-
3	15.2mm	1.60	90	65	50	36	25	18	-	-
4	19.6mm	2.06	104	75	58	42	35	25	12	8
5	25.3mm	2.66	113	81	65	46	37	26	12	9
6	28.4mm	2.98	123	88	69	50	42	30	13	9
7	35.7mm	3.75	127	92	70	51	43	31	15	10

Table 2.2: Experiments with particle Reynolds numbers and Stokes numbers at the first impact (I), the second impact (II), the third impact (III) and the forth impact (IV).

2.3.1 Trajectories for the sphere

The trajectories for a sphere dropped from different distances are compared in figure (2.8). Ideally, the initial falling process from the release surface for each case should coincide. The deviation results from the uncertainty of the experiments; the maximum error is less than 3%. In examing the rebound, the maximum height achieved in the first rebound increases as the initial drop height increases; the time duration from the first collision to the second collision also increases with drop height.

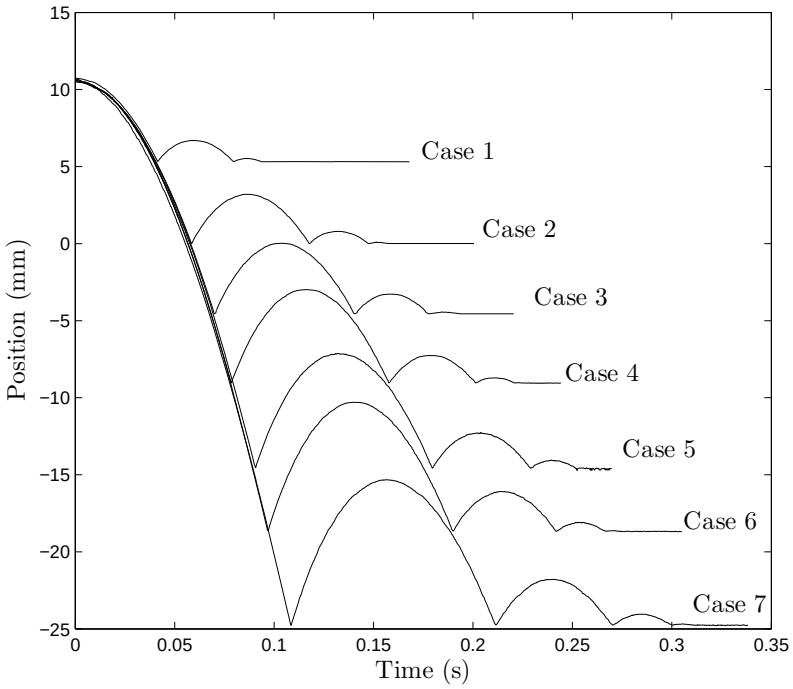

Figure 2.8: Particle trajectories for the given different cases described in Table (2.2).

The measured trajectories are used to calibrate and validate a contact model proposed in the Chapter 4.

2.3.2 Velocity decrease prior to the collision

A velocity decrease is observed when the velocity of the particle is plotted as a function of the gap between the particle and the wall as shown in figure (2.9). The velocity is calculated as the time

derivative of the fitting curve. In figure 2.9(a), the sphere starts from zero velocity at a certain distance away from the wall. It accelerates under gravity and approaches the wall. When it is about to collide with the wall, the velocity decreases. Figure 2.9(b) shows the enlarged detail part: the velocity starts to decrease when the gap decreases below 0.12D. This unique behavior of the impacting sphere does not occur in a dry collision process when the surrounding medium effect is negligible. Joseph *et al.* (2001) observed this velocity decrease prior to the collision in their pendulum-wall collision experiments since there was negligible gravitational acceleration in the horizontal collision between a pendulum and a vertical wall. Gondret *et al.* (2002) who performed the similar experiments of a settling sphere did not obtain the velocity decrease because they used a lower frame rate for the recording camera, 500 fps. When picking data with 500 fps (2 ms interval between two successive points), the detailed behavior of the impacting sphere is missed, especially when it is close to the wall. The velocity decrease cannot be observed, as shown in figure (2.10). Thus a higher frame rate is required to capture this unique behavior of the impacting sphere in a liquid environment.

This velocity decrease is more obvious for a settling process with a smaller Reynolds number. Using the current experiment setup and changing the liquid to pure glycerol, for which the viscosity of the liquid increases to 1.15 Pa·s^{-1} (more than 20 times higher), the same sphere released from zero velocity settles toward the Zerodur wall and rests there without rebound. The Reynolds number of the sphere based on the terminal velocity is $Re = \frac{D\tilde{V}_\infty}{\nu} = 0.67$. The corresponding trajectory is plotted in figure (2.11). The existence of the solid wall interrupts the falling of the sphere, and the effect of the surrounding liquid with this additional solid boundary makes the sphere come to rest in front of the wall.

When plotting the velocity as a function of the gap between the sphere and the wall, the critical distance when the velocity starts to decrease is about one diameter, as shown in figure (2.12). The solid line shown in the figure (2.12) is a calculation of the velocity of a sphere falling in the same surrounding liquid environment without the existence of the solid wall. The falling velocity is

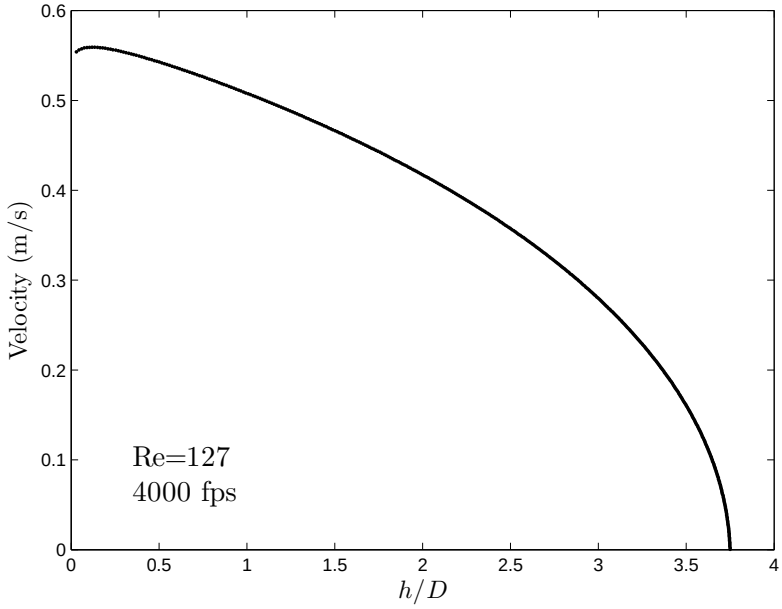

(a)

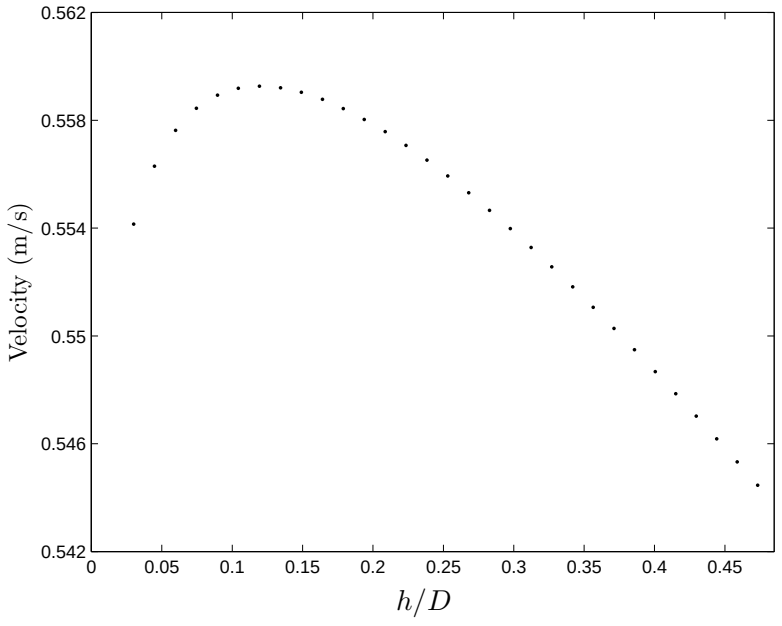

(b)

Figure 2.9: Velocity of the impacting sphere in case 7 with the frame rate 4000 fps. (b) shows the enlarged detail part of (a) when the sphere is about to collide with the wall.

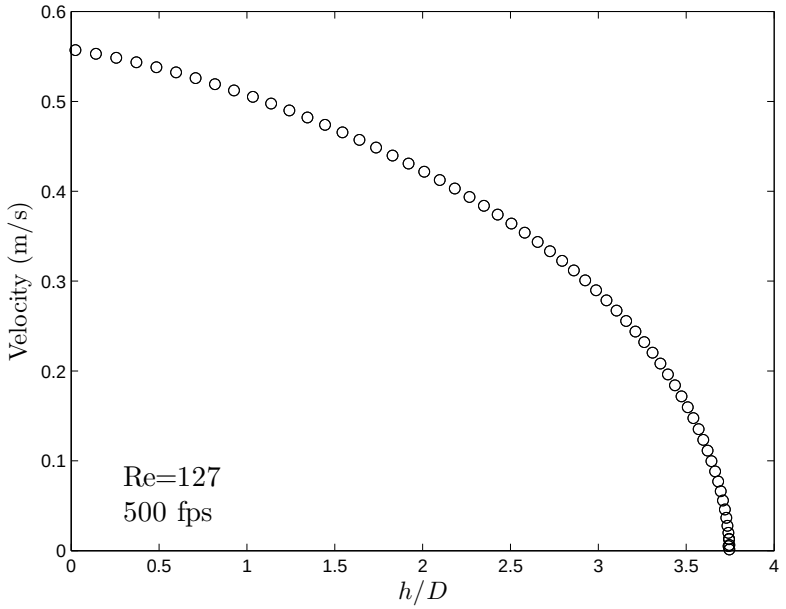

Figure 2.10: Velocity of the impacting sphere in case 7 with the frame rate 500 fps.

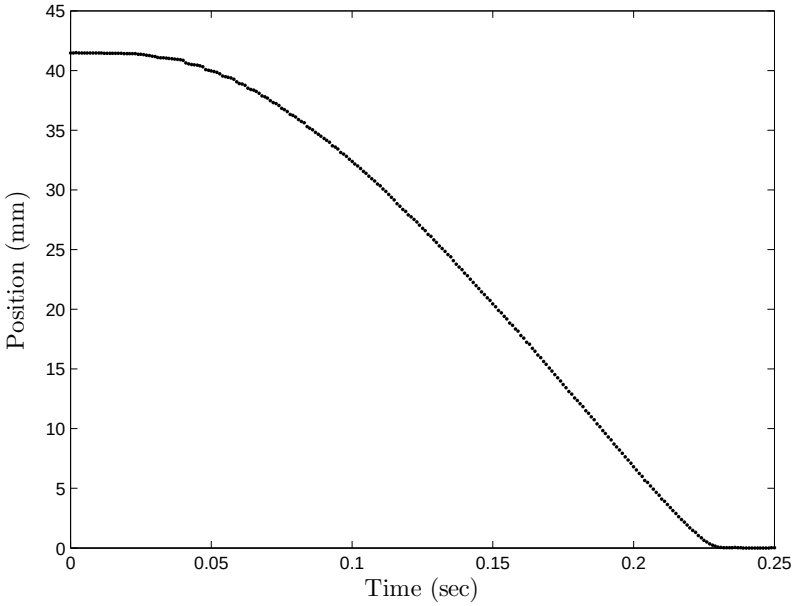

Figure 2.11: Trajectory of a sphere settling on the wall.

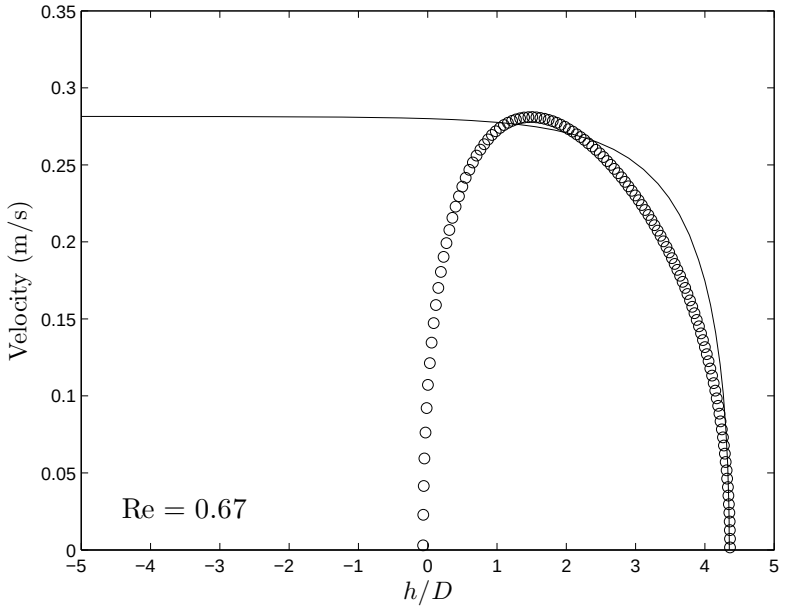

Figure 2.12: Velocity of a sphere settling on the wall with $Re = 0.67$ as a function of the gap between the sphere and the wall.

calculated analytically by solving the equation of motion for a sphere with a low Reynolds number:

$$m_p \frac{d\tilde{V}}{d\tilde{t}} = m_p g - m_l g - F_D$$

where $F_D = 6\pi\mu a V$ is the Stokes drag for the sphere and a is the radius of the sphere. The motion equation can be simplified as an ordinary differential equation for the velocity $\tilde{V}$:

$$\frac{d\tilde{V}}{d\tilde{t}} = g(1 - \frac{\rho_l}{\rho_p}) - \frac{6\pi\mu a}{\frac{4}{3}\pi a^3 \rho_p}\tilde{V}.$$

The velocity of the particle measured from the experiment follows the analytical trend when the gap is large ($h/D > 1$). The deviation is resulted from the omission of the added mass and history force in the equation of the particle motion. When the velocity is increasing, the added mass and history force have noticeable influence on the motion of the particle. These two forces disappear after the terminal velocity is achieved. It is obvious in the figure (2.12) that the velocity decreases after the distance between the sphere and the wall is less than one diameter.

2.3.3 Coefficient of restitution

The coefficient of restitution of each collision, e, is calculated as the ratio of the averaged rebound velocity to the averaged impact velocity over 2 ms time interval. Figure (2.13) shows the semi-log relation between e and the particle impact Stokes number, St, and the result is compared with the observations for steel sphere and Zerodur wall reported by Joseph *et al.* (2001) and Gondret *et al.* (2002). The results from the current experiments present more data for Stokes number ranging from 1 to 100 which is deficient in the previous literature.

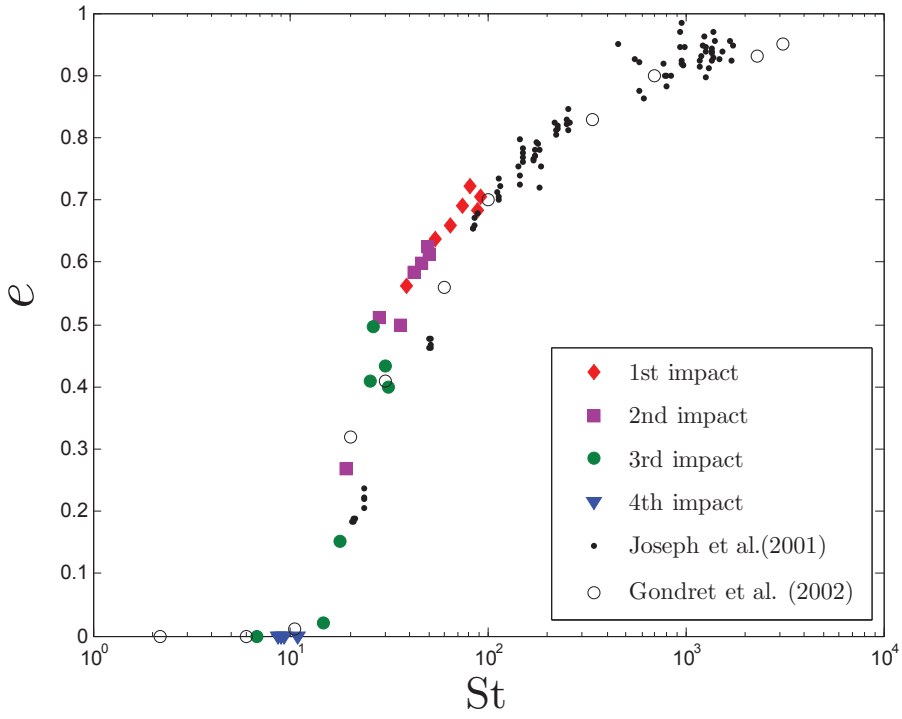

Figure 2.13: Coefficient of restitution for the first and second collisions.

As shown in figure (2.13), the coefficient of restitution is a function of the particle impact Stokes number and agrees with the previous conclusion found by other researchers. For Stokes number less than 10 (all the 4th impacts and one third impact), the coefficient of restitution is zero and there is no visible rebound. As Stokes number increases, the value of e increases with large slope for Stokes number ranging from 10 to 100.

For the Stokes numbers ranging from 20 to 50, the results reported by Joseph *et al.* (2001)

are lower than the current experimental results and the results in Gondret *et al.* (2002). This can be explained by the technique used to evaluate the coefficient of restitution. The coefficient of restitution is calculated as a ratio of the rebound velocity to the impact velocity. The rebound and impact velocities in the current experiments and in Gondret *et al.* (2002) are calculated as the time derivative of the measured trajectory $\triangle h/\triangle t$ with time interval $\triangle t = 2$ ms. The rebound and impact velocities in Joseph *et al.* (2001) were taken as the slopes of the fitted lines over 5 to 10 points (depending on the framing rate that varies from 500 fps to 2000 fps) on the position-time diagram as shown in figure (3.3) so that the obtained velocities are averaged values over 5$\sim$10 ms time interval. The actual collision duration is typically 0.01 ms (measured by Gondret *et al.* (2002) with a piezoelectric sensor). Thus, the coefficient of restitution obtained from all of the experiments is an effective macroscopic value. An average over a longer time interval attenuates the fact that the velocity decreases under the effect of the interstitial liquid so that it produces a larger impact velocity and a lower coefficient of restitution. The difference is more obvious when the liquid is more viscous with Stokes numbers lower than 50. Thus, to capture the actual slowdown for a rapid collision, the time interval cannot be too long. However, the time interval cannot be too short either. The experimental technique, such as the recording rate, limits the minimum time interval. A more important reason is a time interval shorter than 2 ms does not reflect the real approaching velocity but pronounces only the decelerating particle motion.

Chapter 3

Numerical method

To fully resolve the flow field around moving particles and to make a direct coupling between the particles and the fluid motion, an immersed boundary method computer code for axisymmetric flow is developed in cylindrical coordinates based on a fast immersed boundary projection method.

3.1 Immersed boundary method

The immersed boundary method, a popular numerical method for simulating incompressible flow with fluid-structure interaction, was introduced by Peskin in 1970's (see Peskin, 1972). In the present study, the immersed boundary method is used because it is good at handling a moving or deforming body with complex surface geometry. In this method, the flow field is solved on an Eulerian coordinate system that does not need to conform to the solid boundaries. Typically, a Cartesian mesh is used. The solid boundaries are represented by a set of Lagrangian points which can move freely through the fixed Cartesian mesh. Over those Lagrangian points, appropriate forces are applied to enforce the non-slip boundary condition. The forces exist in the continuous Navier-Stokes equations as singular functions, and convolutions with Dirac delta functions are used to exchange information between the Eulerian grid and the Lagrangian points. The computational domain with Eulerian grid discretization and immersed boundary formulation is shown in figure (3.1).

The immersed boundary method was first used to simulate blood flow patterns around heart valves by considering the solid surfaces as flexible elastic membranes with a constitutive rela-

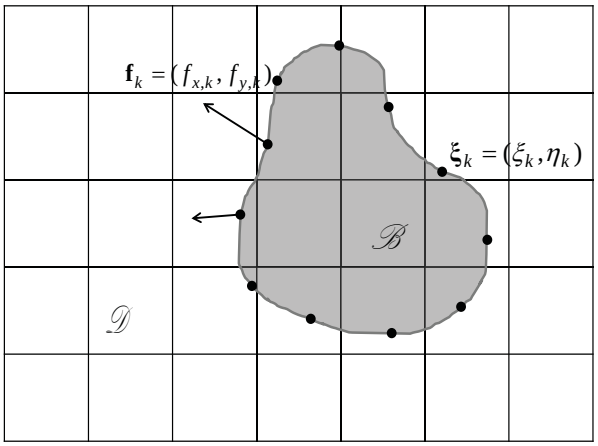

Figure 3.1: Two-dimensional computational domain $\mathscr{D}$ with Eulerian grid and immersed boundary formulation,$\mathscr{B}$, for a body. Lagrangian points, $\boldsymbol{\xi}_k$, are shown along $\partial\mathscr{B}$ with filled dots where boundary forces, $\mathbf{f}_k$, are applied.

tion (see Peskin, 1972); Hooke's law relates the forces to the motion of the Lagrangian points. Beyer & LeVeque (1992) and Lai & Peskin (2000) extended it to rigid surfaces by taking the spring constant to be a large value. However, the above techniques need an appropriate choice of gain (stiffness), which has an obvious influence on the numerical results. A large value of gain in a constitutive relation limits the choice of the time step and a small gain leads to slip error at the solid surface. Higher order extensions are developed to get better results, see Mittal & Iaccarino (2005) for a general review.

3.2 Immersed boundary projection method

To circumvent the tuning parameters in immersed boundary method, an alternative is to consider the boundary forces as Lagrangian multipliers. Similar to the method in which the discretized pressure is treated as Lagrange multiplier to satisfy the continuity constraint (see Chang *et al.*, 2002), the values of the boundary forces are chosen to satisfy the non-slip constraint (see Glowinski *et al.*, 1998). Based on this idea, Taira & Colonius (2007) developed an immersed boundary projection

method to solve the incompressible Navier-Stokes equations with boundary forces as given below:

$$\frac{\partial \mathbf{u}}{\partial t} + \mathbf{u}\cdot\nabla\mathbf{u} = -\nabla p + \frac{1}{Re}\nabla^2\mathbf{u} + \int_s \mathbf{f}(\boldsymbol{\xi}(s,t))\delta(\boldsymbol{\xi}-\mathbf{x})ds \tag{3.1}$$

$$\nabla\cdot\mathbf{u} = 0 \tag{3.2}$$

$$\mathbf{u}(\boldsymbol{\xi}(s,t)) = \int_{\mathbf{x}} \mathbf{u}(\mathbf{x})\delta(\mathbf{x}-\boldsymbol{\xi})d\mathbf{x} = \mathbf{u}_B(\boldsymbol{\xi}(s,t)) \tag{3.3}$$

where $\mathbf{u}$, p and Re are the suitably non-dimensionalized velocity vector, pressure and the Reynolds number, respectively. Spatial variable $\mathbf{x}$ represents position in the flow field, $\mathscr{D}$, and $\boldsymbol{\xi}$ denotes coordinates along the immersed boundary, $\partial\mathscr{B}$, with a velocity of $\mathbf{u}_B$. The third term on the right hand side of equation (3.1) is the boundary force added at the Lagrangian points.

The equations are discretized with a staggered-mesh finite volume formulation. By using appropriate interpolation and regularization operators and certain time marching schemes for the viscous term and the convective terms, the equations can be written as a system of algebraic equations:

$$\begin{bmatrix} A & G & -H \\ D & 0 & 0 \\ E & 0 & 0 \end{bmatrix} \begin{pmatrix} q^{n+1} \\ \phi \\ f \end{pmatrix} = \begin{pmatrix} r^n \\ 0 \\ u_B^{n+1} \end{pmatrix} + \begin{pmatrix} bc_1 \\ bc_2 \\ 0 \end{pmatrix} \tag{3.4}$$

where q^{n+1} and ϕ are the discretized velocity flux and pressure vectors; $A = \frac{1}{\Delta t}M - \alpha_L L$ results from the implicit treatment of the vector term, Δt is the discrete time step, and M and L are the mass matrix and discrete Laplacian operator; G and D are the discrete gradient and divergence operators and are related as $G = -D^T$. The operators H and E are the regularization and interpolation operators resulting from the regularized Dirac delta function in equations (3.1) and (3.3). They are introduced to smear the singular boundary force over a few cells and interpolate velocity values defined on the staggered grid onto the Lagrangian points, respectively. Hf corresponds to the last term in equation (3.1) with $f = (f_x, f_y)^T$. $Eq^{n+1} = u_B^{n+1}$ enforces the non-slip constraint. A superscript for time level is not placed on ϕ and f because they are treated as Lagrange multipliers that do not play a direct role in time advancement but minimize the system energy and satisfy

the kinematic constraints. After introducing a transformed force, $\tilde{f}$, the operators are related as $Hf = -E^T\tilde{f}$. The choice of E and H will be discussed in detail later in section 3.4. Here r^n, bc_1 and bc_2 are the explicit terms in the momentum equation, the boundary condition vector resulting from the Laplacian operator, and the boundary condition vector generated from the divergence operator, respectively. Thus, the linear system (3.4) can be written as:

$$\begin{bmatrix} A & G & E^T \\ G^T & 0 & 0 \\ E & 0 & 0 \end{bmatrix} \begin{pmatrix} q^{n+1} \\ \phi \\ \tilde{f} \end{pmatrix} = \begin{pmatrix} r^n \\ 0 \\ u_B^{n+1} \end{pmatrix} + \begin{pmatrix} bc_1 \\ -bc_2 \\ 0 \end{pmatrix} \tag{3.5}$$

By grouping the pressure and the force variables as λ and reorganizing the sub-matrices in the following form:

$$Q \equiv [G, E^T], \quad \lambda \equiv \begin{pmatrix} \phi \\ \tilde{f} \end{pmatrix}, r_1 \equiv r^n + bc_1, \quad r_2 \equiv \begin{pmatrix} -bc_2 \\ u_B^{n+1} \end{pmatrix},$$

it becomes an algebraic system of equations that is recognized as a Karush-Kuhn-Tucker system:

$$\begin{bmatrix} A & Q \\ Q^T & 0 \end{bmatrix} \begin{pmatrix} q^{n+1} \\ \lambda \end{pmatrix} = \begin{pmatrix} r_1 \\ r_2 \end{pmatrix}. \tag{3.6}$$

A fractional step method can be used to solve the overall system. After performing an LU decomposition, equation (3.6) becomes:

$$\begin{bmatrix} A & 0 \\ Q^T & Q^T B^N Q \end{bmatrix} \begin{bmatrix} I & B^N Q \\ 0 & I \end{bmatrix} \begin{pmatrix} q^{n+1} \\ \lambda \end{pmatrix} = \begin{pmatrix} r_1 \\ r_2 \end{pmatrix} + \begin{pmatrix} -\frac{\Delta t^N}{2^N}(LM^{-1})^N Q\lambda^{n+1} \\ 0 \end{pmatrix}$$

where, B^N is the Nth order Taylor series expansion of A^{-1} and can be made symmetric and positive definite with appropriate choices of Δt and N. There is an Nth order splitting error in the second term of the right hand side which is the leading order error resulting from the truncation in B^N so

a third-order expansion for B^N is required, see Taira & Colonius (2007).

The matrices can be recombined such that an intermediate velocity q^* is formed as

$$\begin{pmatrix} q^* \\ \lambda \end{pmatrix} = \begin{bmatrix} I & B^N Q \\ 0 & I \end{bmatrix} \begin{pmatrix} q^{n+1} \\ \lambda \end{pmatrix}$$

Finally, three steps are performed to solve the whole system:

$$Aq^* = r_1 \tag{3.7}$$

$$Q^T B^N Q\lambda = Q^T q^* - r_2 \tag{3.8}$$

$$q^{n+1} = q^* - B^N Q\lambda \tag{3.9}$$

Equations (3.7) and (3.8) can be solved by using conjugate gradient method since the matrices in these equations are symmetric and positive definite. The third equation is the projection step resulting in the solution of the whole system. In this method, the divergence-free constraint and the non-slip boundary condition can be satisfied to an arbitrary accuracy implicitly at the next time level, and the CFL number is only limited by the choice of the time marching schemes of the viscous and convective terms. The method is second order accurate in time and better than first order accurate in space in L_2 norm.

To apply the above method and the relative code (courtesy of Kunihiko Tiara) in simulating the evolution of the flow field during a wet collision process, the motion of the particle needs to be known prior to the simulation. As a first step, the motion of the sphere was described with experimental data. In the pendulum-wall collision experiments performed by Joseph *et al.* (2001), the trajectory of a sphere before and after colliding with a stationary wall in a glycerol-water mixture was recorded by a CCD camera. As an example, during a collision process at St = 186, the position of the sphere center can be plotted as functions of time, as shown in figure (3.2).

In the experiment record, the time interval between two neighbor points was $dt = 0.001$ s because the frame speed of the camera was 1000 fps. Based on the points near the wall, the impact and

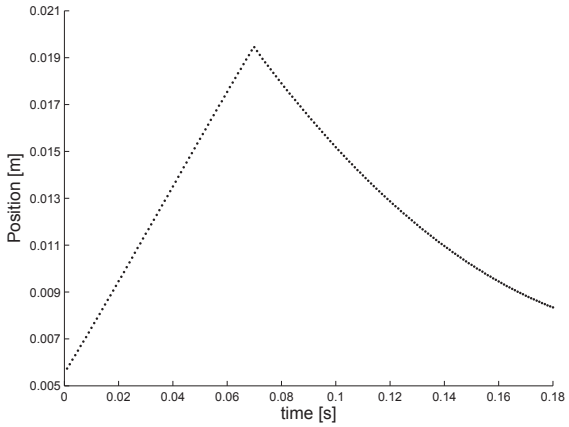

Figure 3.2: Trajectory of a steel particle with diameter 7.39mm during the collision process in a mixture of glycerol and water with specific density 1.143, viscosity 7.305cp. The points are the positions of the center of the sphere at different time.

rebound velocities were obtained as shown in figure (3.3).

The collision position of the sphere center x_c is taken to be the intersection of the two lines fitting the trajectory before and after the collision. Because of the uncertainty in the location of the wall, the position of the wall was determined artificially. Leweke, Thompson & Hourigan (2004) took the minimum distance between the sphere and wall as $0.005D$ when they calculated the collision with $\mathrm{Re} \geq 1000$. Both experimental and computational tests were conducted in Leweke *et al.* (2004) to verify that this had negligible influence on the predictions. For our cases with $\mathrm{Re} < 250$, as a first try, the minimum distance between the sphere and the wall was taken as $0.02D$. So, the wall position was taken as $x_c + 0.5D + 0.02D$ in our cases. With linear interpolation, more points were inserted into the trajectory so that the time interval was decreased to $dt = 0.25$ ms. The simulation was performed for different cases with different Stokes numbers. For example, in one case with $\mathrm{St} = 186$, the initial grid geometry is sketched in figure (3.4). Then, for every time step, the positions of the Lagrangian points on the particle surface are updated according to the experiment record. The collision happened at the 279th time step which corresponds to the maximum value of the position x_c in figure (3.3).

An accurate description of the evolvution of the flow field was obtained. Figure (3.5) presents the streamline configuration before and after the collision. The direction of the streamline around

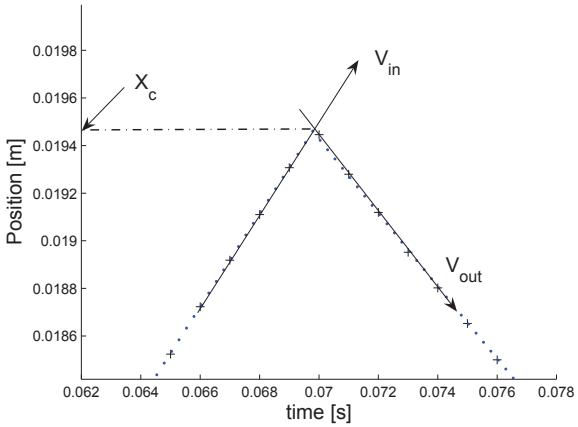

Figure 3.3: Details of the trajectory close to the wall. "+" represents the recorded position. "·" represents the interpolated point. The arrows give the impact and the rebound velocities before and after the collision. The intersection of the arrows is considered as the final collision point, x_c.

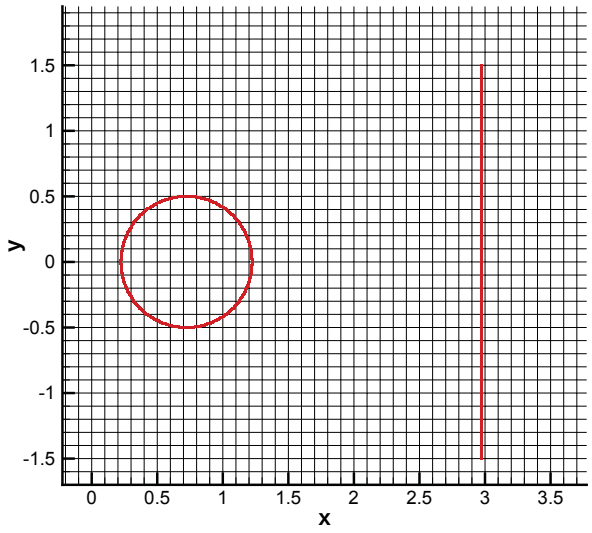

Figure 3.4: Initial grid geometry of the case with St= 186.

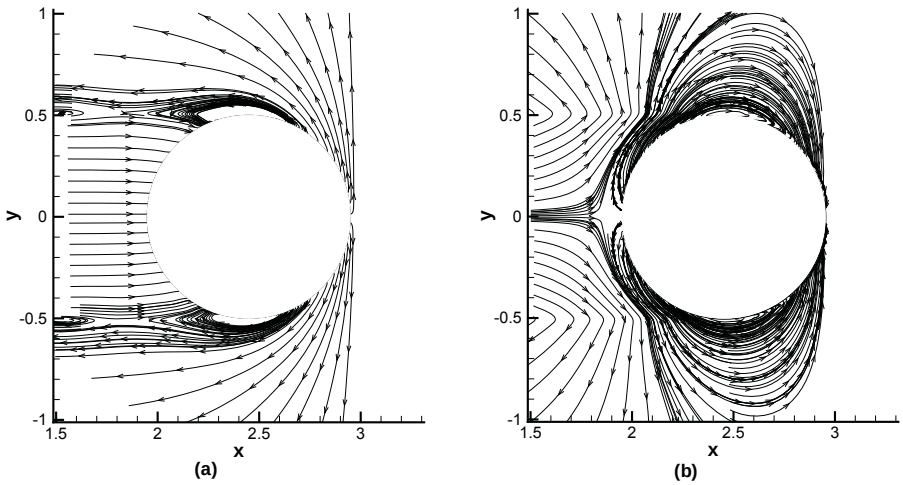

Figure 3.5: (a) Stream line distribution 0.25 ms before the collision. (b) Stream line distribution 0.25 ms after the collision.

the particle and close to the wall changes after the collision, resulting in a high shear stress in those regions. The distribution of the vorticity field before and after the collision is shown in figure (3.6).

The shear stress generated along the wall changes with time, as shown in figure (3.7). The variables are non-dimensionalized with the diameter of the sphere. As the solid body approaches the wall the amplitude of the shear stress along the wall increases and the position corresponding to the maximum shear stress moves toward the final contact point. After the collision, as the solid body moves away from the wall, the surrounding liquid reenters the growing gaps between the solid body and the wall. Thus, the shear stress changes to opposite direction and its magnitude decreases as the gap increases.

Because the simulation is two dimensional, it is impossible to quantitatively verify whether the simulated results are right. Experimentally, it is difficult to perform an experiment in which a two dimensional cylinder collides with a planar wall exactly parallel as it impacts the wall and rebounds. When trying to apply the numerical method to a three dimensional case, the limitation of this method makes it unfeasible. To solve equation (3.8), the conjugate gradient method requires a large number of iterations to make the convergence error small to satisfy the divergence-free and no-slip constraints. Thus, in a three dimensional case, a significantly longer time is required to yield a

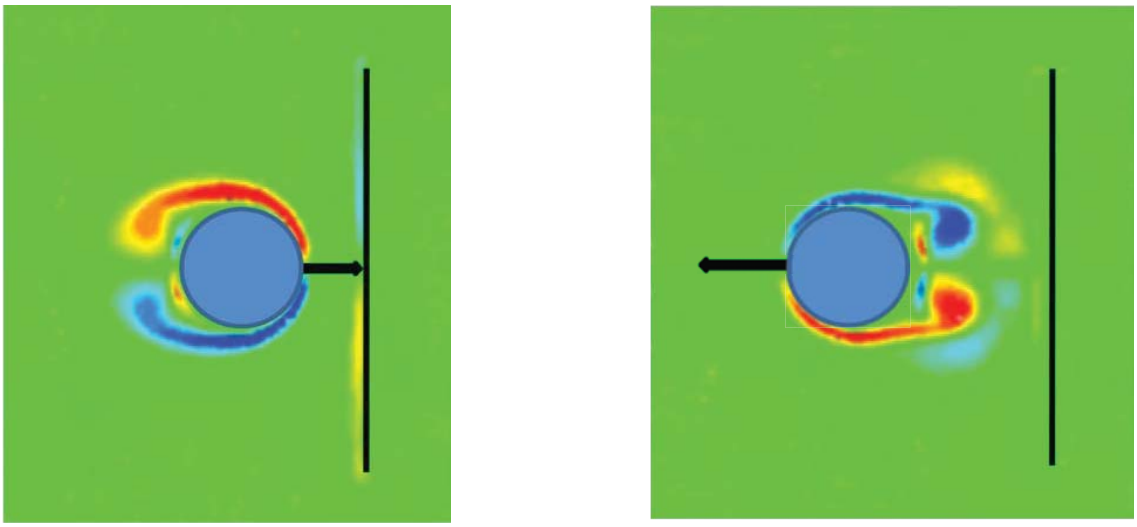

Figure 3.6: Vorticity distribution of the flow field before and after the collision.

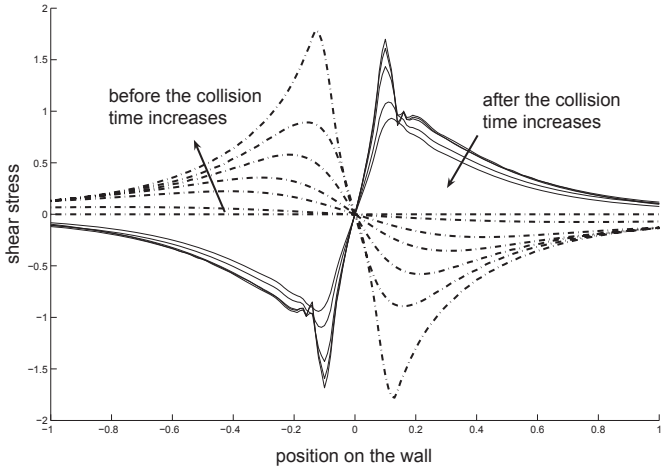

Figure 3.7: Shear stress distributions along the wall. The dash-dot and solid lines represent the shear stress distributions before and after the collision, respectively.

suitable solution.

3.3 Fast immersed boundary projection method

To improve the above numerical method, Colonius & Taira (2008) used a null space approach and a multi-domain technique to develop a fast immersed boundary projection method.

To eliminate the most computationally expensive component of the projection method, the pressure Poisson solver for equation (3.8), the nullspace approach is used by applying discrete curl operator, C, to the Navier-Stokes equations, such that

$$q = Cs, \quad \gamma = C^T q.$$

where q, s and γ are the discrete velocity flux vector, streamfunction and circulation. Here, C is a constructed null space for the discrete divergence operator. Thus:

$$DC \equiv 0$$

which corresponds to the relation $\nabla \cdot \nabla \times \equiv 0$. Hence,

$$Dq^{n+1} = DCs^{n+1} \equiv 0$$

which means the divergence-free constraint can be automatically satisfied.

When using a uniform Cartesian mesh and simply boundary conditions, the discrete Laplacian can be diagonalized by a sine transform. Thus, after applying the implicit trapezoidal rule on the viscous term with $\alpha_L = \frac{1}{2}$ and second-order Adam-Bashforth method on the convective term, the transformed system of equations has only one linear system that need to be solved. This system with a positive definite and symmetric left-hand side operator can be solved by conjugate gradient method. Moreover, by applying this curl operator to the momentum equation, the pressure variable is eliminated so that the dimension of equation (3.8) is dramatically decreased from $N \times N$ to

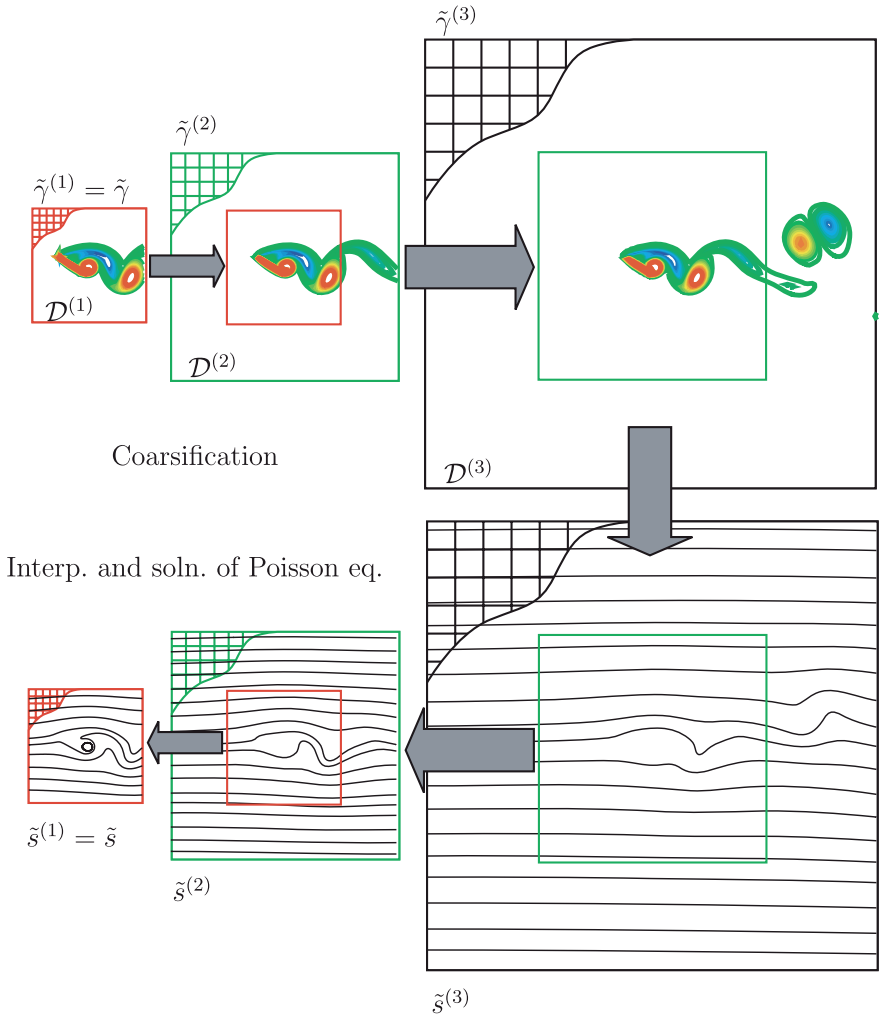

Figure 3.8: Schematic of a 3-level multi-domain solution of the Poisson equation. The figure is taken from figure 5 in Colonius & Taira (2008).

$N_f \times N_f$, where N is the Eulerian grid size and N_f is the number of boundary forces which is two times the number of Lagrangian points in a two dimensional case. $N_f \ll N$. Many fewer iterations are required than the original modified Poisson equation. Thus, this approach saves significant computation time.

However, applying uniform grid over the whole computational domain with simple boundary conditions results in low computational efficiency if the grid size is fine everywhere as that for the region of interest. Thus, to achieve high efficiency with uniform grid and simultaneously get sufficient resolution at the region of interest, a multi-domain technique is employed, as shown in figure (3.8).

A series of computation domains are used. The solution in a larger domain with simplified far-field boundary conditions and coarser grid is interpolated along the inner boundary of a smaller domain and provides the boundary condition for the smaller domain with finer grid. Thus, the domain of interest is solved with high efficiency but still enough resolution and with boundary values known in a simple form. Colonius & Taira (2008) should be consulted for further details.

3.4 Modification for axisymmetric system

The purpose of this study is to understand the contact mechanism of an immersed collision process. A normal collision is good enough to capture the essence of the relevant physics. An axisymmetric flow field surrounding the sphere particle and the horizontal wall resulted from a normal collision is simpler to solve than the three-dimensional problem. To apply the fast immerse boundary projection method to an axisymmetric system, modifications are made to the Navier-Stokes equations and the algorithms to solve the discrete linear systems.

3.4.1 Discrete Navier-Stokes equations for axisymmetric system

For an axisymmetric incompressible flow in cylindrical coordinates, the velocity $\mathbf{u}(u_z, u_r, 0)$, the vector potential $\mathbf{B}(0, 0, \psi/r)$ and the vorticity $\mathbf{w}(0, 0, \omega)$ are related as $\mathbf{u} = \nabla \times \mathbf{B}$, $\mathbf{w} = \nabla \times \mathbf{u}$, and $\mathbf{w} = -\nabla^2 \mathbf{B}$. The relation between the scalar variables (u_z,u_r) and streamfunction ψ are:

$$u_z = \frac{1}{r}\frac{\partial \psi}{\partial r}, \quad u_r = -\frac{1}{r}\frac{\partial \psi}{\partial z}.$$

With those additional radial factors, the corresponding discrete variables have new relations:

$$q = \hat{R}^{-1} C R s \tag{3.10}$$

where, $C = \begin{bmatrix} \frac{\partial}{\partial r} \\ -\frac{\partial}{\partial z} \end{bmatrix}$ is the discrete curl operator, $R = \mathrm{diag}(R_{i,j})$ is a diagonal matrix of the radial coordinates of the vertices of the cells where the discrete streamfunction s is defined and

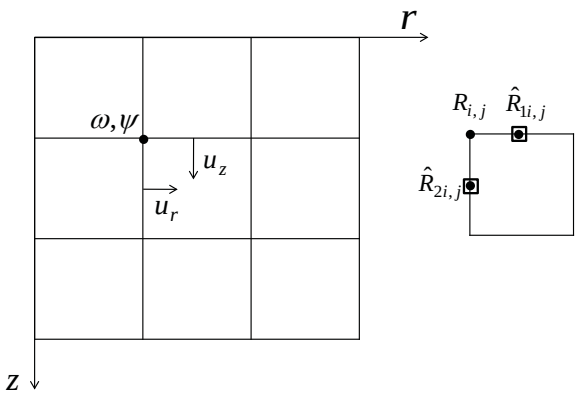

Figure 3.9: Location of Eulerian variables on cylindrical coordinates and the definition of matrices $\hat{R}$ and R.

$\hat{R} = \begin{bmatrix} \mathrm{diag}(\hat{R}_{1i,j}) & 0 \\ 0 & \mathrm{diag}(\hat{R}_{2i,j}) \end{bmatrix}$ is a diagonal matrix of the radial coordinates of the center points on the cell edges where the discrete velocity flux q is defined. Figure (3.9) shows the configuration of the Eulerian variables defined on cylindrical grids for an axisymmetric system (z,r) and the definition of matrices R and $\hat{R}$.

The relation between streamfunction ψ and vorticity ω gives:

$$\omega = -\frac{\partial}{\partial r}\left(\frac{1}{r}\frac{\partial \psi}{\partial r}\right) - \frac{\partial^2}{\partial z^2}\left(\frac{\psi}{r}\right).$$

Then, discretely, the circulation γ corresponding to ω is related to s as:

$$\gamma = -C^T \hat{R}^{-1} C R s. \tag{3.11}$$

So that

$$s = -(C^T \hat{R}^{-1} C R)^{-1} \gamma. \tag{3.12}$$

since $C^T \hat{R}^{-1} C R$ is a square matrix and can be inverted. Thus, combining equation (3.10) and (3.12) yields:

$$q = \hat{R}^{-1} C R (C^T \hat{R}^{-1} C R)^{-1} \gamma, \tag{3.13}$$

Now, considering the Navier-Stokes equation of momentum with the immersed boundary forces:

$$\frac{\partial \mathbf{u}}{\partial t} + \mathbf{u} \cdot \nabla \mathbf{u} = -\nabla p + \frac{1}{Re}\nabla^2 \mathbf{u} + \int_s \mathbf{f}(\boldsymbol{\xi}(s,t))\delta(\boldsymbol{\xi} - \mathbf{x})ds$$

with the relation

$$\mathbf{u} \cdot \nabla \mathbf{u} = \nabla(\frac{1}{2}\mathbf{u}^2) - \mathbf{u} \times (\nabla \times \mathbf{u}),$$

and

$$\nabla^2 \mathbf{u} = \nabla(\nabla \cdot \mathbf{u}) - \nabla \times (\nabla \times \mathbf{u}) = -\nabla \times (\nabla \times \mathbf{u}),$$

which incorporates incompressible condition $\nabla \cdot \mathbf{u} = 0$, the momentum equation can be rewritten as:

$$\frac{\partial \mathbf{u}}{\partial t} + \nabla(p + \frac{1}{2}\mathbf{u}^2) = \mathbf{u} \times \mathbf{w} - \frac{1}{Re}\nabla \times \mathbf{w} + \int_s \mathbf{f}(\boldsymbol{\xi}(s,t))\delta(\boldsymbol{\xi} - \mathbf{x})ds.$$

After applying a curl operator, it becomes:

$$\frac{\partial \mathbf{w}}{\partial t} = \nabla \times (\mathbf{u} \times \mathbf{w}) - \frac{1}{Re}\nabla \times (\nabla \times \mathbf{w}) + \nabla \times \int_s \mathbf{f}(\boldsymbol{\xi}(s,t))\delta(\boldsymbol{\xi} - \mathbf{x})ds$$

Then, the semi-discrete circulation form of the Navier-Stokes equations is:

$$\frac{d\gamma}{dt} = C^T N(q) - \beta C^T \hat{R}^{-1} C R \gamma + C^T H f + b c_\gamma. \tag{3.14}$$

where C^T is the discrete curl operating on the variables defined at the centers of cell edges, C is the discrete curl operating on the variables defined at the vertices of cells, β is a constant equal to $1/(Re\Delta z^2)$, where Δz is the uniform grid spacing and $\Delta r = \Delta z$, and bc_γ is the inhomogeneous term depending on the particular boundary conditions. $N(q)$ denotes discretized non-linear term $(\mathbf{u} \times \mathbf{w})$, which is calculated as:

$$\begin{vmatrix} \hat{e_z} & \hat{e_r} & \hat{e_\theta} \\ u_z & u_r & u_\theta \\ 0 & 0 & \omega \end{vmatrix} = u_r \omega \hat{e_z} - u_z \omega \hat{e_r}$$

Because the velocity variables are defined on the center of a cell edge and the vorticity is defined at the vertices of a cell, as shown in figure (3.9), then, in z direction:

$$(u_r\omega)_{i,j} = \frac{1}{2}(\bar{u}_{r(i,j+1)}\omega_{i,j+1} + \bar{u}_{r(i,j)}\omega_{i,j})$$

in r direction:

$$(u_z\omega)_{i,j} = \frac{1}{2}(\bar{u}_{z(i+1,j)}\omega_{i+1,j} + \bar{u}_{z(i,j)}\omega_{i,j})$$

where i and j are the indices for grids in z and r direction, respectively. The bar values are the averages at the center of an edge calculated as:

$$\bar{u}_{z(i,j)} = \frac{1}{2}(u_{z(i,j)} + u_{z(i,j-1)}),$$

and

$$\bar{u}_{r(i,j)} = \frac{1}{2}(u_{r(i,j)} + u_{r(i-1,j)})$$

from the values at the vertices. Thus, the nonlinear term finally is still defined at the vertices of cells.

The regularization operator, H, is related to the delta function and its form will be given as following together with the interpolation operator E. For the delta function, in two dimensional problems, a discrete form that is proposed by Roma *et al.* (1999) is used in Taira & Colonius (2007). A similar form is used here for an axisymmetric system in cylindrical coordinates:

$$d(r) = \begin{cases} \frac{1}{6\Delta r}\left[5 - 3\frac{|r|}{\Delta r} - \sqrt{-3(1-\frac{|r|}{\Delta r})^2 + 1}\right] & \text{for } 0.5\Delta r \le |r| \le 1.5\Delta r; \\ \frac{1}{3\Delta r}\left[1 + \sqrt{-3\left(\frac{r}{\Delta r}\right)^2 + 1}\right] & \text{for } |r| \le 0.5\Delta r; \\ 0 & \text{otherwise.} \end{cases} \tag{3.15}$$

where Δr is the cell width of the staggered grid in the r-direction. This discrete delta function is specifically designed for use on staggered grids. In this form, the delta function is supported

over only three cells which is an advantage for computational efficiency. Taira & Colonius (2007) compared the results for the current formulation with other discrete functions and did not find significant differences.

Then, for a two-dimensional axisymmetric case, discretizing the convolution of $\boldsymbol{u}$ and δ in equation (3.3) yields

$$u_k = \Delta z \Delta r \sum_i u_i d(z_i - \xi_k) d(r_i - \eta_k) \tag{3.16}$$

where u_i is the discrete velocity vector defined on the staggered grid (z_i,r_i) and u_k is the discrete boundary velocity at the kth Lagrangian point(ξ_k,η_k). Using α to denote the factor preceding the summation, the interpolation operator in equation (3.16) is defined as

$$\hat{E}_{k,i} = \alpha d(z_i - \xi_k) d(r_i - \eta_k). \tag{3.17}$$

Letting $E \equiv \hat{E} R^{-1}$ for use of the velocity flux, $q^{n+1} = Ru^{n+1}$, the non-slip boundary condition can be represented as

$$\hat{E}_{k,i} {u_i}^{n+1} = E_{k,i} {q_i}^{n+1} = u_{B_k}^{n+1} \tag{3.18}$$

The regularization operator, H, is a discrete version of the convolution operator in equation (3.1) that passes information from the Lagrangian points, $\boldsymbol{\xi}_k$, to the neighboring Eulerian grid points, $\boldsymbol{x}_i$. In a similar manner as E, H is defined as

$$H_{i,k} = \beta \hat{M}_i d(z_i - \xi_k) d(r_i - \eta_k) = \frac{\beta}{\alpha} \hat{M}_i \hat{E}_{k,i}^T, \tag{3.19}$$

where β is the numerical integration factor proportional to the interval between two neighboring Lagrangian points. The diagonal matrix $\hat{M}$ is used for consistency with the fractional step formulation.

To relate the regularization operator with the interpolation operator in a similar manner as

mentioned in section 3.2, a transformed forcing function $\tilde{f}$ is introduced so that

$$Hf = -E^T \tilde{f}.$$

Thus, the original boundary force can be retrieved by $f = -(EH)^{-1} E E^T \tilde{f}$. Because of the uniform grid with $\Delta z = \Delta r$, the relation simplifies to $f = -\frac{1}{\Delta z^2} \frac{\alpha}{\beta} \tilde{f}$.

So, the final semi-discrete momentum equation in circulation form, equation (3.14) can be written as:

$$\frac{d\gamma}{dt} + C^T E^T \tilde{f} = C^T N(q) - \beta C^T \hat{R}^{-1} C R \gamma + b c_\gamma. \tag{3.20}$$

After applying the second order Adam-Bashforth method to the nonlinear convective term:

$$C^T N(q) \rightarrow C^T \left[\frac{3}{2} N(q)^n - \frac{1}{2} N(q)^{n-1} \right]$$

and implicit trapezoidal rule to the viscous term:

$$\beta C^T \hat{R}^{-1} C R \gamma \rightarrow \beta C^T \hat{R}^{-1} C R \frac{1}{2} (\gamma^{n+1} + \gamma^n),$$

the fully discrete system is

$$(I + \frac{\Delta t}{2} L)\gamma^{n+1} + \Delta t C^T E^T \tilde{f} = (I - \frac{\Delta t}{2} L)\gamma^n - \Delta t C^T \left[\frac{3}{2} N(q)^n - \frac{1}{2} N(q)^{n-1} \right] + \Delta t b c_\gamma \tag{3.21}$$

where $L = \beta C^T \hat{R}^{-1} C R$ is the discrete Laplacian operator for an axisymmetric system in cylindrical coordinates.

Now consider the boundary condition for the Navier-Stokes equations:

$$\int_{\mathbf{x}} \mathbf{u}(\mathbf{x}) \delta(\mathbf{x} - \boldsymbol{\xi}) d\mathbf{x} = \mathbf{u}_B(\boldsymbol{\xi}(s,t))$$

Using the relation (3.13), the discrete form is written as:

$$Eq^{n+1} = E\hat{R}^{-1}CR(C^T\hat{R}^{-1}CR)^{-1}\gamma^{n+1} = u_B^{n+1} \tag{3.22}$$

After combining the equation (3.21) and (3.22), the linear system for axisymmetric case is:

$$\begin{pmatrix} I + \frac{\Delta t}{2}L & \Delta t C^T E^T \\ E\hat{R}^{-1}CR(C^T\hat{R}^{-1}CR)^{-1} & 0 \end{pmatrix} \begin{pmatrix} \gamma^{n+1} \\ \tilde{f} \end{pmatrix} = \begin{pmatrix} rhs \\ u_B^{n+1} \end{pmatrix} \tag{3.23}$$

where rhs is a simplified denotation for the right hand side of equation (3.21).

Following the idea of the fast immersed boundary projection method and applying LU decomposition to the coefficient matrix yields:

$$\begin{pmatrix} I + \frac{\Delta t}{2}L & \Delta t C^T E^T \\ EQ & 0 \end{pmatrix} = \begin{pmatrix} I + \frac{\Delta t}{2}L & 0 \\ EQ & -EQ(I + \frac{\Delta t}{2}L)^{-1}\Delta t C^T E^T \end{pmatrix} \begin{pmatrix} I & (I + \frac{\Delta t}{2}L)^{-1}\Delta t C^T E^T \\ 0 & I \end{pmatrix}$$

where $Q = \hat{R}^{-1}CR(C^T\hat{R}^{-1}CR)^{-1}$ for simplification. After defining the intermediate variable:

$$\begin{pmatrix} \gamma^* \\ \tilde{f} \end{pmatrix} = \begin{pmatrix} I & (I + \frac{\Delta t}{2}L)^{-1}\Delta t C^T E^T \\ 0 & I \end{pmatrix} \begin{pmatrix} \gamma^{n+1} \\ \tilde{f} \end{pmatrix}, \tag{3.24}$$

the three steps to solve the linear system for axisymmetric case are:

$$(I + \frac{\Delta t}{2}L)\gamma^* = rhs, \tag{3.25}$$

$$EQ(I + \frac{\Delta t}{2}L)^{-1}\Delta t C^T E^T \tilde{f} = EQ\gamma^* - u_B^{n+1}, \tag{3.26}$$

$$\gamma^{n+1} = \gamma^* - (I + \frac{\Delta t}{2}L)^{-1}C^T E^T \tilde{f}. \tag{3.27}$$

To solve the above system, consider sine transform which is denoted as:

$$\hat{\gamma} = S\gamma \quad \leftrightarrow \quad \gamma = S\hat{\gamma},$$

where the circumflex denotes the Fourier coefficients.

In the current simulation, the grid is uniform and Dirichlet boundary condition is used: the velocity normal to the boundary is zero and the vorticity is zero. It is appropriate at the axis of symmetry, $r = 0$, since $u_r \mid_{r=0} \equiv 0$ and $\omega = \frac{\partial u_r}{\partial z} - \frac{\partial u_z}{\partial r} \equiv 0$ resulting from $\frac{\partial}{\partial r} \equiv 0$. For the other three boundaries, the error caused by using such kind of simplified far-field boundary conditions in smaller computational domains is minimized by applying a multi-domain technique as mentioned in section 3.3, see Colonius & Taira (2008) for a detailed description and discussion of the technique.

Hence, first type of sine transform in Fortran fast fourier transform library which is odd around $k = -1$ and odd around $k = n$ is used. The relation of the sine transform pair means that the sine transform can be normalized so that it is identical to its inverse, $S^{-1} = S$. So, $SS = I$.

For a Poisson equation:

$$Lx = b$$

after applying a sine transform, it becomes:

$$SLx = Sb$$

It can be written as:

$$SLSSx = Sb$$

Let $T \equiv SLS$, $\hat{x} = Sx$, and $\hat{b} = Sb$, then

$$T\hat{x} = \hat{b}$$

Here, T for an axisymmetric system in cylindrical coordinates can be reordered to become a tri-

diagonal matrix

$$\begin{pmatrix} b_2 & c_2 & & & 0 \\ a_3 & b_3 & c_3 & & \\ & a_4 & b_4 & \ddots & \\ & & \ddots & \ddots & c_{N-1} \\ 0 & & & a_N & b_N \end{pmatrix}$$

with

$$\begin{aligned} a_j &= \frac{j-2}{j-3/2}, \quad j = 3, 4, \cdots, N \\ b_j &= -2 + 2\cos\left(\frac{i-1}{M}\pi\right) - \frac{j-1}{j-1/2} - \frac{j-1}{j-3/2}, \quad j = 2, 3, \cdots, N \qquad (3.28) \\ c_j &= \frac{j}{j-1/2}, \quad j = 2, 3, \cdots, N-1 \qquad (3.29) \end{aligned}$$

where N and M are the grid size in r direction and z direction, respectively.

Thus, the Poisson equation and the first step (3.25) with this tri-diagonal system can be solved by a routine code.

But, the resulting matrix in the second step (3.26) is not symmetric; hence, the conjugate gradient method cannot be used. Although general minimal residual method(GMRES) method can be applied to solve this non-symmetric system, a large number of iterations are required and the numerical method is not efficient as before.

3.4.2 Non-slip boundary condition for axisymmetric system

A modification of the representational form for the non-slip boundary condition is proposed for solving an axisymmetric system based on the fast immersed boundary projection method. Considering the axisymmetric flow surrounding a moving sphere and a wall in cylindrical coordinates, an additional radial weight factor is inserted into equation (3.3) making new boundary conditions for

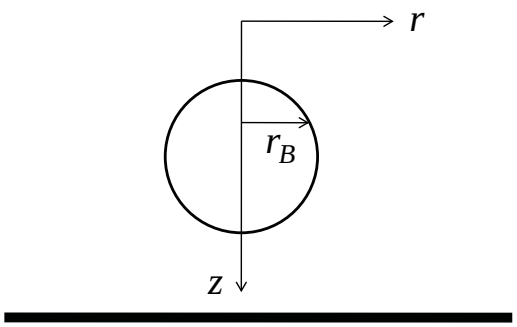

Figure 3.10: The configuration of the cylindrical coordinates for the axisymmetric flow surrounding a moving sphere and a wall.

an axisymmetric system in cylindrical coordinates as:

$$r\boldsymbol{u}(\boldsymbol{\xi}(s,t)) = \int_{\boldsymbol{x}} r\boldsymbol{u}(\boldsymbol{x})\delta(\boldsymbol{x}-\boldsymbol{\xi})d\boldsymbol{x} = r_B\boldsymbol{u}_B(\boldsymbol{\xi}(s,t)), \tag{3.30}$$

where r_B is defined as shown in figure (3.10).

Thus, the discrete form given in equation (3.22) is changed to:

$$E\hat{R}q^{n+1} = ECR(C^T\hat{R}^{-1}CR)^{-1}\gamma^{n+1} = r_B u_B^{n+1}; \tag{3.31}$$

And the corresponding system of algebraic equations is:

$$\begin{pmatrix} (I+\frac{\Delta t}{2}L) & C^TE^T \\ ECR(C^T\hat{R}^{-1}CR)^{-1} & 0 \end{pmatrix}\begin{pmatrix} \gamma^{n+1} \\ \tilde{f} \end{pmatrix} = \begin{pmatrix} rhs \\ r_B u_B^{n+1} \end{pmatrix} \tag{3.32}$$

After applying the projection approach to decompose the matrix, the coefficient matrix becomes:

$$\begin{pmatrix} (I+\frac{\Delta t}{2}L) & 0 \\ ECR(C^T\hat{R}^{-1}CR)^{-1} & -ECR(C^T\hat{R}^{-1}CR)^{-1}(I+\frac{\Delta t}{2}L)^{-1}C^TE^T \end{pmatrix}\begin{pmatrix} I & (I+\frac{\Delta t}{2}L)^{-1}C^TE^T \\ 0 & I \end{pmatrix} \tag{3.33}$$

Using the definition for the intermediate variable γ^* given in equation (3.24), the new three steps to solve the system are:

$$((I+\frac{\Delta t}{2}L)\gamma^* = rhs, \tag{3.34}$$

$$ECR(C^T\hat{R}^{-1}CR)^{-1}(I+\frac{\Delta t}{2}L)^{-1}C^TE^T\tilde{f}=ECR(C^T\hat{R}^{-1}CR)^{-1}\gamma^*-r_Bu_B^{n+1}\Delta z, \tag{3.35}$$

$$\gamma^{n+1}=\gamma^*-(I+\frac{\Delta t}{2}L)^{-1}C^TE^T\tilde{f}. \tag{3.36}$$

The first equation (3.34) is exactly the same as before and can be solved with a routine solver for a tri-diagonal matrix. The current second step, equation (3.35), can be solved with conjugate gradient method since its coefficient matrix is symmetric positive definite as proven below:

$$\begin{aligned}(C^T\hat{R}^{-1}CR)^{-1}(I+\frac{\Delta t}{2}L)^{-1} &= [(I+\frac{\Delta t}{2}L)(C^T\hat{R}^{-1}CR)]^{-1}\\ &= [C^T\hat{R}^{-1}CR+\frac{\Delta t}{2}C^T\hat{R}^{-1}CRC^T\hat{R}^{-1}CR]^{-1}\\ &= R^{-1}[C^T\hat{R}^{-1}C+\frac{\Delta t}{2}C^T\hat{R}^{-1}CRC^T\hat{R}^{-1}C]^{-1}\end{aligned} \tag{3.37}$$

R and $\hat{R}$ are positive diagonal matrices, thus $\left(\hat{R}^{-1}\right)^T=\hat{R}^{-1}$. Then

$$\left(C^T\hat{R}^{-1}C\right)^T=C^T\hat{R}^{-1}C.$$

So, $C^T\hat{R}^{-1}CRC^T\hat{R}^{-1}C$ must be symmetric positive definite. Thus, the coefficient matrix of (3.35)

$$ECR(C^T\hat{R}^{-1}CR)^{-1}(I+\frac{\Delta t}{2}L)^{-1}C^TE^T=EC[C^T\hat{R}^{-1}C+\frac{\Delta t}{2}C^T\hat{R}^{-1}CRC^T\hat{R}^{-1}C]^{-1}C^TE^T$$

must be symmetric and positive definite.

The whole axisymmetric flow field can be solved accurately with high efficiency if the solid boundary velocity is known.

3.5 Verification of the modification for axisymmetric system

To validate the cylindrical coordinate modifications, the code was run to solve different problems with and without immersed boundaries in the flow field. The simulated results are compared with theoretical results and the results reported by other researchers.

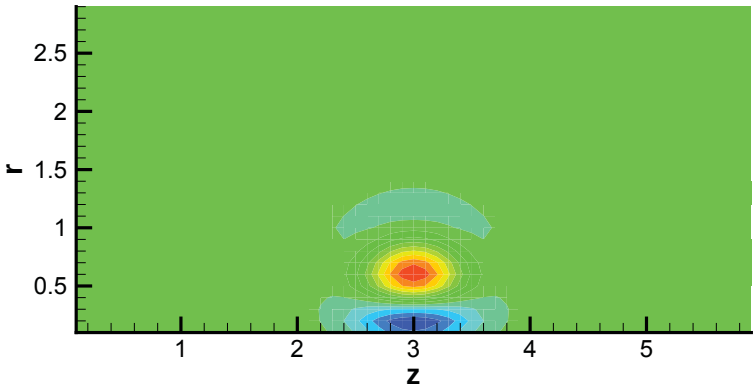

Figure 3.11: The known vorticity field.

3.5.1 Verification of the solution for the Poisson-like equation

The first step in the resulting linear system, equation (3.34), is a Poisson-like equation with the Laplacian operator in cylindrical coordinates for axisymmetric system. To verify the solution of this Poisson-like equation, the code was run to solve a streamfunction from a Poisson equation with a known vorticity field. The equation to be solved is:

$$-\nabla^2\psi = \omega$$

with an arbitrary picked vorticity field:

$$\omega = -8r(1 + 63r^2 + 8r^4 + 8r^2z^2 - 48zr^2)\exp\left(-4[r^2 + (z-3)^2]\right).$$

The theoretical result of the streamfunction can be calculated analytically as:

$$\psi = r^3\exp\left(-4[r^2 + (z-3)^2]\right).$$

The distribution of the vorticity field is shown in figure (3.11). The numerical result of the streamfunction compares favorably with the analytical result as shown in figure 3.12(b) and 3.12(a).

The computational domain is taken to be [0,6]×[0,3]. The L^2 norm of the difference between the numerical and analytical results is calculated and plotted as a function of the Eulerian grid size, N.

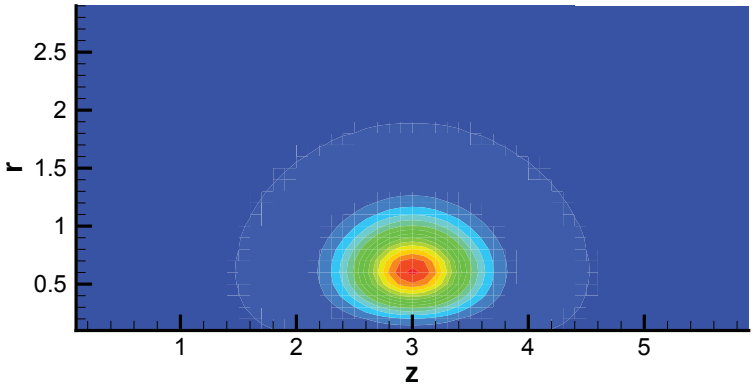

(a) theoretical

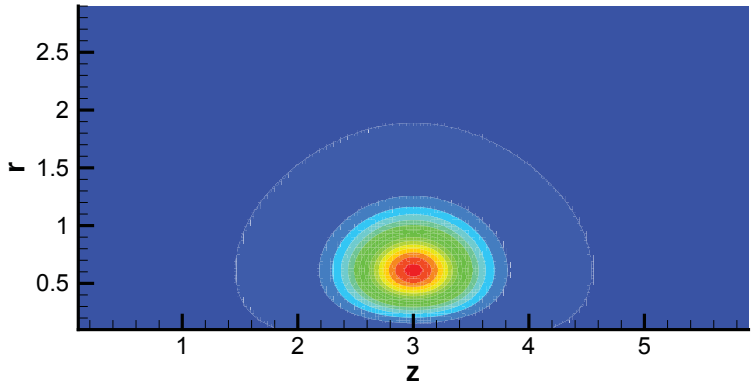

(b) numerical

Figure 3.12: The streamfunction distribution.

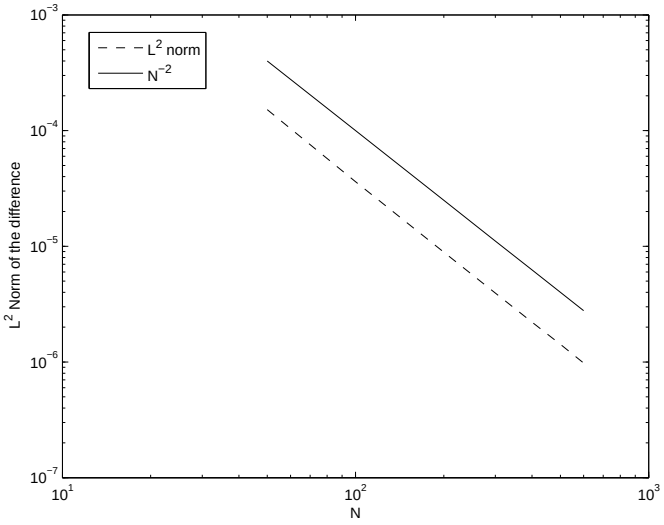

Figure 3.13: The L^2 norm of the difference between the numerical and analytical result of the vorticity field. The solid line is the L^2 norm as a function of the grid size. The dashed line is N^{-2}.

Figure (3.13) shows that the second order accuracy is achieved in L^2 norm.

Thus, the solution of the Poisson-like equation 3.34 obtained in the same manner can also be trusted with second order accuracy.

3.5.2 Verification of the solution with immersed boundaries

Simulations of flow passing a stationary sphere of unit diameter are performed to verify the solution with immersed boundaries in the flow field. In an axisymmetric domain with initial uniform flow, U_∞, a set of Lagrangian points along a half circle with its center at ($z = 3$,$r = 0$) is introduced to represent the sphere. There are two different configurations for setting the Lagrangian points, as shown in figure (3.14). In figure 3.14(a), there are Lagrangian points on the axisymmetric z axis, and in figure 3.14(b) there is no Lagrangian point on z axis. In those two configurations, the intervals between the Lagrangian points are identical and equal to a cell size in Eulerian grid, $\Delta s \approx \Delta z = \Delta r$. Simulations with these two different configurations for Reynolds number $Re = 100$ are both performed and the results are compared in Table (3.1).

The simulated results of wake dimensions and drag coefficient at a steady state for different Reynolds numbers, $Re = U_\infty D/\nu = 100, 200$ are compared with the simulated results reported in

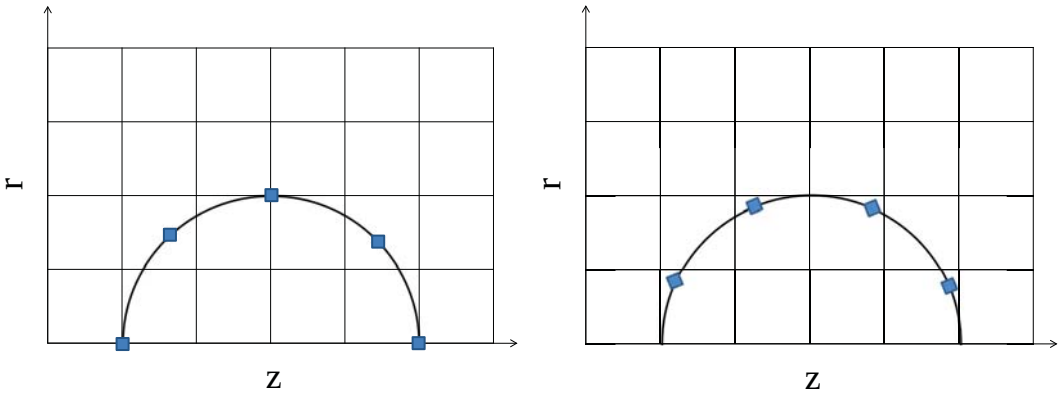

(a) with Lagrangian points on z axis (b) w/o Lagrangian points on z axis

Figure 3.14: The configuration of the setting of Lagrangian points.

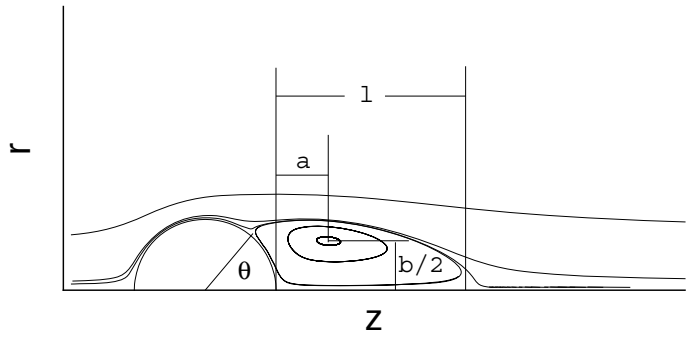

Figure 3.15: The characteristic dimensions of the wake structure. The parameters, l, a, and b represent the length of the recirculation zone, distance from the sphere to the center of the wake vortex, and the gap between the centers of the wake vortices, respectively. θ is the separation angle.

Taira (2008) and Johnson & Patel (1999). The good agreement is shown in Table (3.1). The size of the wake is characterized by the characteristics lengths, l, a, b, and θ (non-dimensionalized by the diameter) defined in figure (3.15). The grid resolution and the time step are set to $\Delta z = \Delta r = 0.02$ and $\Delta t = 0.005$, the same as the setting in the other two reports.

According to our simulations, with or without Lagrangian points on the z axis does not make obvious difference. No Lagrangian point on the z axis is used in the following simulation unless otherwise stated.

The characteristics lengths of wake are close to the reported values, except that the separation angle, θ, is smaller. This discrepancy comes from the fact that the Lagrangian multipliers adding to the boundary points disturb the development of the boundary layers and the disturbance leads

		l	a	b	θ	C_D
$Re = 100$	with Lagrangian pts on axis	0.867	0.249	0.579	47.6°	1.10
	w/o Lagrangian pts on axis	0.871	0.249	0.600	46.8°	1.10
	Johnson & Patel (1999)	0.88	0.25	0.60	53°	1.10
	Taira (2008)	0.91	0.28	0.59	50°	1.14
$Re = 200$	w/o Lagrangian pts on axis	1.400	0.370	0.712	51.0°	0.78
	Johnson & Patel (1999)	1.46	0.39	0.74	63°	0.80
	Taira (2008)	1.38	0.37	0.69	61°	0.82

Table 3.1: Comparison of the simulation results of steady-state wake dimensions and drag coefficient from flow over a sphere.

to a smaller separation angle.

The force exerted by the surrounding liquid on the solid body is calculated based on the boundary forces in the simulation. In equation (3.1), the boundary forces as Lagrangian multipliers are smeared by the discrete delta function to the neighboring Eulerian grids. The resulting body forces are integrated over the whole flow field as:

$$f_z = \sum_{i,j} f_{zi,j} \pi (r_j^2 - r_{j-1}^2) \Delta z \tag{3.38}$$

where f_z is the force in z direction. As for an axisymmetric flow, the r direction force is zero. Then the drag coefficient, C_D can be calculated. As shown in Table (3.1), the results obtained from the axisymmetric simulations with Reynolds number $Re = 100, 200$ are found to be in accord with the values reported by other researchers.

Thus, the evolution of the flow field can be simulated accurately when the position and velocity of the immersed boundaries are prescribed. The force exerted by the liquid flow on the immersed body can be calculated from the simulation.

3.6 The evolution of the flow coupled to the motion of the particle

After knowing the effect of liquid force on a moving solid body, the evolution of the flow field and the motion of the sphere are coupled by writing Newton's law in the z direction for a falling sphere as shown in figure (3.10) as:

$$m_p \frac{d\tilde{V}}{d\tilde{t}} = \tilde{f}_{\text{SIM}} + m_p g + \tilde{f}_b, \tag{3.39}$$

where $\tilde{V}$ is the velocity of the sphere which is considered to be a uniform value for $\boldsymbol{u}_{\text{B}}$ in equation (3.30) over the whole sphere surface; m_p is the mass of the sphere, g is the gravitational acceleration and $\tilde{f}_{\text{SIM}}$ is the liquid-solid interaction force in vertical direction calculated from the flow solution using equation (3.38); $\tilde{f}_b$ is the vertical buoyancy force resulting from the hydrostatic pressure gradient which is not included in $\tilde{f}_{\text{SIM}}$. Rotation of the sphere is not considered in this process.

The position and the velocity of the sphere are the boundary conditions for the Navier-Stokes equations. For the flow field surrounding a falling sphere with diameter D, the Navier-Stokes equations are non-dimensionalized with characteristic length $L_o = D$ and time $t_o = \sqrt{D/g}$ so that the non-dimensional parameter, Reynolds number, is defined as $Re_D = \frac{D\sqrt{Dg}}{\nu}$ where ν is the kinematic viscosity of the liquid. After introducing the density ratio, $\tau = \frac{\rho_p}{\rho_l}$, where ρ_p is the density of the particle and ρ_l is the density of the liquid, the equation of the motion can be non-dimensionalized as:

$$\frac{dV}{dt} = \frac{1}{\tau}(f_{\text{SIM}} + \tau - 1) \tag{3.40}$$

where f_{SIM} is the non-dimensional force exerted by the surrounding fluid and can be calculated from f_z.

The coupled evolution of the flow field and the motion of the sphere are integrated in time using a second order Runge-Kutta method. Starting from nth time step with known variables, γ^n, ${u_B}^n$, ${x_B}^n$ and ${f_z}^n$, the variables at the $(n+1)$th time step come be found from the following process.

1. Calculate f_{SIM} from f_z at nth time step,

2. Solve equation (3.34) for γ^*:

$$(I + \frac{\Delta t}{2}L)\gamma^* = rhs(\gamma^n, x_B^n)$$

3. Calculate $u_B^{n+\frac{1}{2}}$, $x_B^{n+\frac{1}{2}}$, and the corresponding operator $E^{n+\frac{1}{2}}$ and $E^{T^{n+\frac{1}{2}}}$ as:

$$u_B^{n+\frac{1}{2}} = u_B^n + \frac{\Delta t}{\tau}(f_{\text{SIM}} + \tau - 1)$$

$$x_B^{n+\frac{1}{2}} = x_B^n + \Delta t u_B^n$$

4. Solve equation (3.35) for $\tilde{f}^*$ and calculate f_z^* and f_{SIM}^*:

$$E^{n+\frac{1}{2}}CR(C^T\hat{R}^{-1}CR)^{-1}(I + \frac{\Delta t}{2}L)^{-1}C^T E^{T^{n+\frac{1}{2}}}\tilde{f}^* = E^{n+\frac{1}{2}}CR(C^T\hat{R}^{-1}CR)^{-1}\gamma^* - r_B u_B^{n+\frac{1}{2}}$$

5. Calculate u_B^{n+1}, x_B^{n+1}, and the corresponding operator E^{n+1} and $E^{T^{n+1}}$:

$$u_B^{n+1} = u_B^n + \frac{\Delta t}{\tau}(\frac{1}{2}(f_{\text{SIM}} + f_{\text{SIM}}^*) + \tau - 1)$$

$$x_B^{n+1} = x_B^n + \Delta t\frac{1}{2}(u_B^n + u_B^{n+\frac{1}{2}})$$

6. Solve equation (3.35)for $\tilde{f}$ and calculate f_z at $(n+1)$th time step:

$$E^{n+1}CR(C^T\hat{R}^{-1}CR)^{-1}(I + \frac{\Delta t}{2}L)^{-1}C^T E^{T^{n+1}}\tilde{f} = E^{n+1}CR(C^T\hat{R}^{-1}CR)^{-1}\gamma^* - r_B u_B^{n+1}$$

7. Solve equation (3.36) for γ^{n+1}

$$\gamma^{n+1} = \gamma^* - (I + \frac{\Delta t}{2}L)^{-1}C^T E^T\tilde{f}.$$

Thus, starting from $t = 0^+$ with an acceleration of the effect of the gravity and buoyancy force,

the particle moves automatically in the flow field. The kinetic behavior of the particle and also the evolution of the flow field introduced by the moving body can both be calculated from the simulation.

3.7 Validation of the coupled solution

To validate the coupled algorithm, the simulation results are compared with the experimental results by TenCate *et al.* (2002). In the experiment, a sphere settled toward the bottom of a vessel full of silicon oil. The trajectory and associated flow field are measured from the moment of release until rest at the bottom of the container vessel. The sphere with a diameter $D = 15$ mm was initially suspended at an initial distance 120 mm. The density of the sphere is $\rho_p = 1.12 \times 10^3$ kg·m^{-3} and the density of the liquid is $\rho_l = 0.96 \times 10^3$ kg·m^{-3}. The dynamic viscosity of the surrounding liquid is $\mu_f = 0.058$ Pa·s. The Reynolds number based on the ultimate velocity V_∞ is $Re = 31.9$. Simulations with the above input parameters are performed.

The trajectory and the velocity profiles are compared in figure (3.16). The circles in the figure are digitized from figure 8 in TenCate *et al.* (2002). The comparison shows that the simulation coupling the evolution of the flow field and the motion of the sphere predicts the same motion of the sphere as found in the experiment. Note that the Stokes number at impact $St = 4.1$ is small and the particle does not rebound from the wall. In the current simulations, similar results are found with two different grid sizes supporting the convergence of the method.

Figure (3.17) shows the comparison of the spatial structure of the flow field at the moment when the sphere is a half sphere diameter from the wall. The velocity magnitude contours show good agreement between the experimental and the simulated flow field.

A time series of the fluid velocity at a particular point in the flow domain are compared in figure (3.18). This point is one diameter from the wall and one diameter from the center of the sphere. The radial and axial velocity components are given on the top and bottom in the figure, respectively. The evolution of the velocity components show that a vortex passes the point and the wake of the sphere follows after the sphere comes to rest. The good agreement indicates that the numerical method accurately captures not only the dynamic behavior of the sphere but also the evolution of

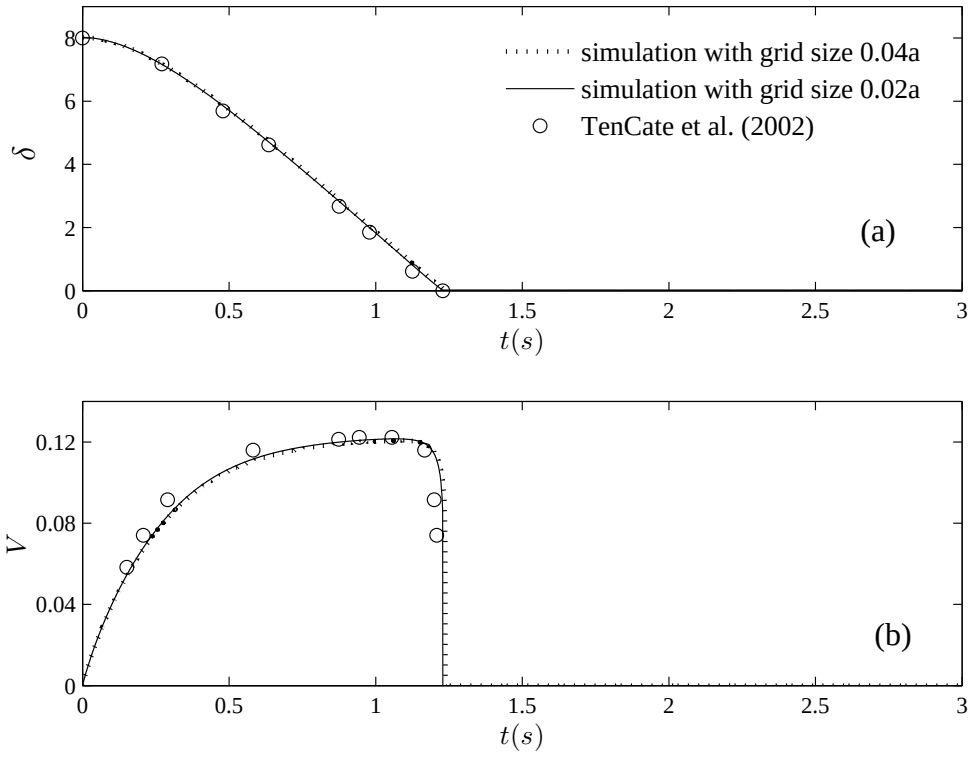

Figure 3.16: Comparison of (a) trajectory and (b) velocity profiles for the experiments of TenCate *et al.* (2002), et al. and the current simulations for a sphere falling on to a surface; the Stokes number based on the settling velocity is 4.1.

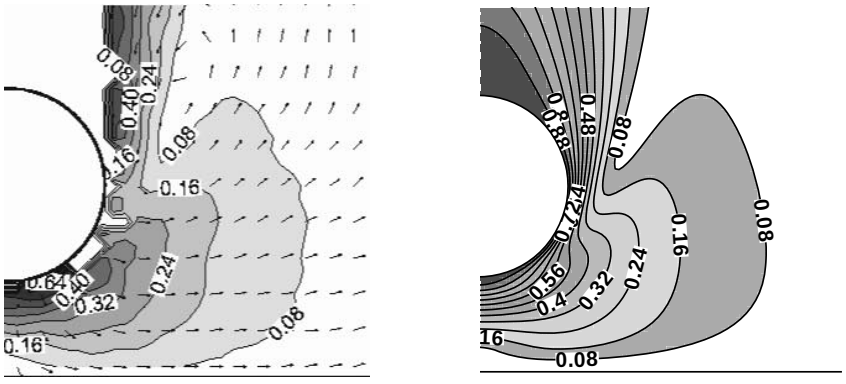

(a) (b)

Figure 3.17: Comparison of (a) the PIV experiment data from TenCate *et al.* (2002) and (b) the simulated result of flow field when the sphere is a half sphere diameter from the wall. Contour indicates the normalized velocity magnitude.

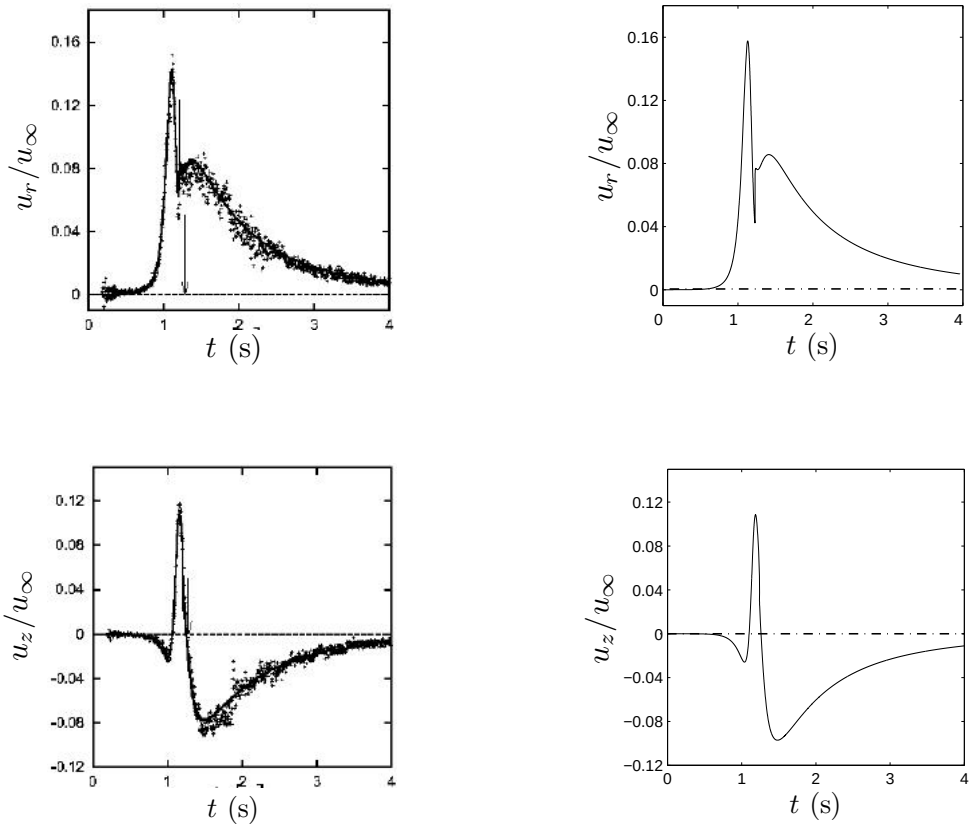

Figure 3.18: Comparison of time series of the fluid velocity at a point located one diameter from the wall and one diameter from the center of the sphere. The data on the left are the experimental results and the lattice Boltzmann simulation from TenCate *et al.* (2002) and the right are the results from the current simulation.

the flow field.

Chapter 4

Contact model

The numerical method described in Chapter 3 computes the motion of a sphere and the evolution of the surrounding flow field before the sphere collides with a wall. To simulate the collision process, a contact model is required to capture the contact mechanism of an immersed collision process. In the beginning of this chapter, the physics of a lubricated impact of a steel sphere on a glass plate is introduced briefly. Then, a contact model is developed to deal with the two difficult points in numerical simulations, the thin lubrication layer effect and the elastic deformation of the solid parts. The liquid-solid interaction forces for a sphere moving in a viscous liquid with steady/unsteady velocity are briefly reviewed especially for the case when there is another solid boundary, such as a solid wall. Based on the analytical formulas that are presented and well proven by previous researchers, a liquid-solid interaction force is proposed to incorporate the lubrication effect when a sphere is close to a wall. The elasticity of the solid materials is incorporated by applying an elastic-like force on a sphere when the distance between the sphere and the wall diminishes below a threshold value. The new force term is defined based on Hertz elastic theory and includes the inelastic effect to dissipate the kinetic energy of the sphere during collision.

4.1 Physics of a lubricated impact of a sphere on a wall

People investigated the contact mechanism of a lubricated impact of a sphere on a wall by coupling the fluid dynamics and the elastic solid mechanics. The results of a steel ellipsoidal sphere impacting on a glass plate given by Al-Samieh & Rahnejat (2002) are represented in figure (4.1). The shape

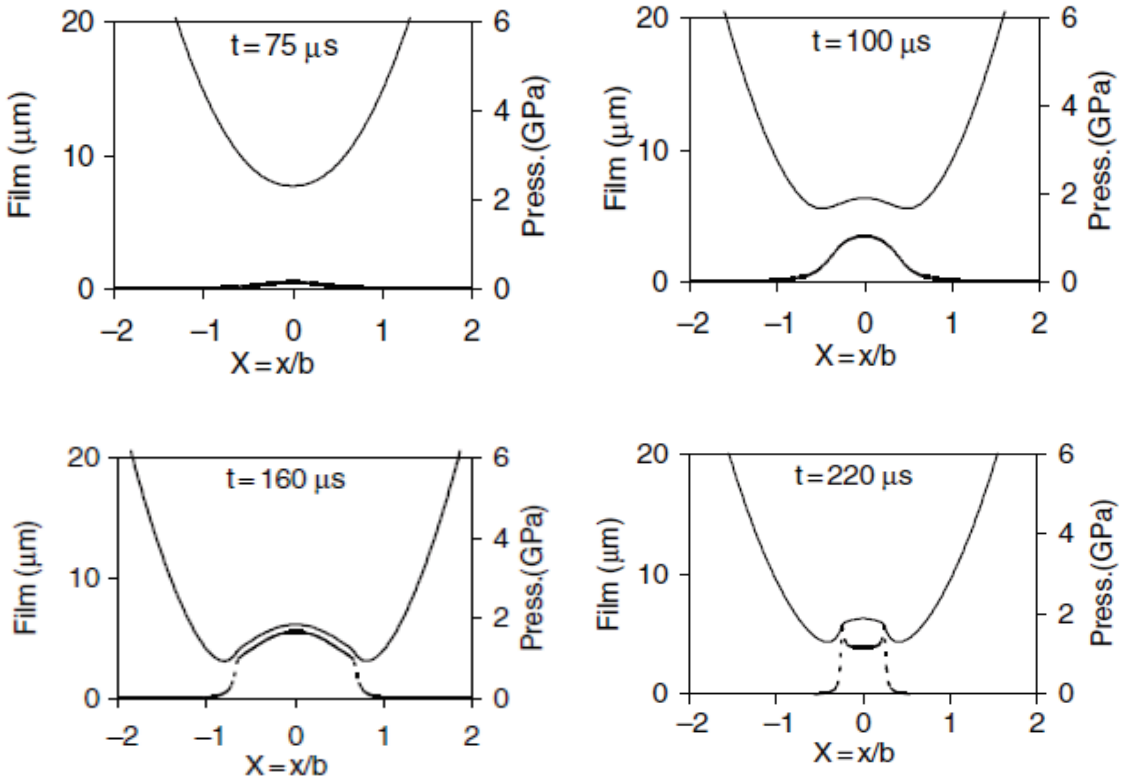

Figure 4.1: Physics of a lubricated impact of a sphere on a wall. The shape of the elastic sphere and the pressure distribution in the interstitial liquid layer are presented together at different time steps.

of the elastic sphere is presented together with the pressure distribution in the interstitial liquid layer. As the sphere approaches the plate, high pressure building up in the lubrication layer deforms the elastic body and makes the sphere rebound before it actually contacts the plate. This can be considered to be the essential physics during an immersed collision process.

As shown in figure (4.1), the liquid layer is very thin (about several micrometers) and hard to be resolved in a numerical simulation. Using a finer grid can delay but not prevent the problem. Also, the particle and wall are rigid in the current simulations; hence, the elasticity of the materials is not included. As a result, the simulations do not include the energy stored in the elastic deformation of the sphere and the wall, which is critical to the rebounding of an impacting sphere. To deal with those problems, a contact model is developed to capture the collision process: the effect of the liquid layer is incorporated by using a liquid-solid interaction force term; the elastic deformation of the solid parts is incorporated by using an elastic force term.

4.2 Liquid-solid interaction force with wall effect

The interaction between a moving solid particle and the surrounding fluid has been studied by different researchers. A thorough review can be found in Michaelide (1997). Three types of hydrodynamic forces are most widely discussed and established. The Stokes drag force is an expression for the force exerted on a sphere steadily moving in an unbounded viscous liquid. The unsteady forces due to acceleration of the relative velocity of a body can be divided into two parts: the added mass force and the history force. The added mass force accounts for the inertia added to a solid body because of an acceleration or deceleration relative to the fluid. The history force addresses the temporal delay of the boundary layer development when the relative velocity between the particle and the surrounding fluid varies in time. When there is an additional solid boundary, the hydrodynamics forces are influenced because the fluid is restricted by the second solid boundary. Prior studies have developed correction terms for the gap between the two solid boundaries on the three forces. Yang (2006) summarized and simplified the analytical formulas for the hydrodynamic forces including the wall effect and validated the formulas with experimental results. The forces and the simplified formulas are briefly introduced in the following subsections and are applied in the contact model.

4.2.1 Stokes drag force

For a sphere of radius, a, with a steady velocity, U, moving through an incompressible fluid with viscosity, μ, when the Reynolds number is small, Stokes (1880) derived a drag force as $\tilde{f}_D = 6\pi a\mu U$. From experimental results for Reynolds number greater than one, a coefficient, $\phi(Re)$, is multiplied as a correction factor to account for the inertia effect. Hence, the drag force is computed as:

$$\tilde{f}_D = 6\pi a\mu U\phi(Re) \tag{4.1}$$

with

$$\phi(Re) = 1 + 0.15Re^{0.687} \tag{4.2}$$

for $1 < Re < 800$; a complete list of $\phi(Re)$ for a sphere over a range of Reynolds numbers can be found in Clift *et al.* (1978).

When a sphere moves close to a wall, the existence of the second boundary restricts the evolution of the fluid flow surrounding the sphere. Brenner (1961) developed a correction term for Stokes drag by solving the quasi-steady Stokes equation; the viscous drag force is represented as $\tilde{f}_D = 6\pi a\mu U\lambda(\delta^*)$, where $\delta^* = h/a$ is the non-dimensional gap scaled by the radius of the sphere. A '*' mark is used to distinguish from the previous non-dimensional gap $\delta = h/D$ scaled by the diameter. The value of $\lambda(\delta^*)$ increases with diminishing gap and converges to the classical lubrication theory when $\delta^* = 0$.

For flow at higher Reynolds number, the convective acceleration of the liquid between the two solid boundaries becomes important and a small gap Reynolds number, $Re_h = hU/\nu$, is defined. Cox & Brenner (1967) extended the correction term and incorporated the gap Reynolds number as:

$$\lambda(\delta^*, Re_h) = \frac{1}{\delta^*}\left[1 + \frac{1}{5}(1 \pm \frac{1}{4}Re_h)\delta^* \log\frac{1}{\delta^*}\right] \tag{4.3}$$

where a plus sign in front of the gap Reynolds number is used for an approaching sphere and a negative sign is used when the sphere rebounds from the wall. Then, the wall-modified viscous drag can be written as:

$$\tilde{f}_D = 6\pi a\mu U\lambda(\delta^*, Re_h). \tag{4.4}$$

Thus, for a sphere moving toward a solid wall, the drag force can be calculated by using equation (4.1) with (4.2) when it is far from the wall and equation (4.4) with correction term (4.3) when it is close to the wall. The transition is made at the position where two different correction terms converge to a single value.

4.2.2 Added mass force

Friedrich Bessel proposed the concept of added mass in 1828 to describe the motion of a pendulum in a fluid (see Stokes, 1851). The period of such a pendulum increased relative to its period in a

vacuum (even after accounting for buoyancy effects), indicating that the surrounding fluid increased the effective mass of the system. Added mass, also known as 'virtual' mass is the inertia added to a body because it must move some volume of surrounding fluid as it accelerates or decelerates since the body and fluid cannot occupy the same physical space simultaneously. A recent paper by Bagchi & Balachandar (2003) can be consulted for a detailed discussion.

To find the added mass force with the wall effect, the kinetic energy in the fluid phase when a solid sphere moves towards a wall at velocity $U(t)$ is calculated (see Milne-Thomson, 1968) as:

$$T = \frac{1}{4} m_l U^2(t) \left[1 + 3W(\delta^*)\right],$$

where $m_l = 4/3\pi a^3 \rho_l$ is the mass of the liquid displaced by the sphere and $W(\delta^*) = \sum_{n=1}^{\infty} \left(\frac{\mu_n}{\mu_0}\right)$. The infinite sum term results from a series of dipole images accounting for the wall in the upstream flow. The upstream flow is considered to be potential flow since the vorticity is confined to boundary layer for the particle Reynolds numbers beyond the Stokes flow regime. The functions μ_n with $n = 0, 1, \cdots$ depend on sphere center-to-wall distance $l = (\delta^* + 1)$.

When using the time rate of change of the total kinetic energy in the fluid phase as the work done by a moving sphere, the added mass force can be calculated as:

$$\tilde{f}_{AM} = -\frac{1}{U}\frac{dT}{dt} = -\frac{1}{2} m_l \frac{dU}{dt} - \frac{3}{2} m_l W(\delta^*) \frac{dU}{dt} - \frac{3}{4} m_l U \frac{dW(\delta^*)}{dt}. \tag{4.5}$$

The first term involving dU/dt on the right hand side is the conventional added mass term for a sphere moving in an unbounded flow. The last two terms account for the wall effect. With the relation $dW(\delta^*)/dt = (dW/d\delta^*)(d\delta^*/dt)$ and $d\delta^*/dt = (1/a)dh/dt = -U/a$, the third term can be written as $(3/4)m_l(U^2/a)(dW/d\delta^*)$.

Yang (2006) analyzed the expression of the wall correction terms in detail and approximated the infinite sum with a finite sum. After compared with experimental results from a pendulum collision,

Yang presented $W(\delta^*)$ in the second term of equation (4.8) and $dW/d\delta^*$ in the third term as:

$$W_7(\delta^*) = \frac{1}{8l^3} + \frac{1}{(4l^2-1)^3} + \frac{1}{(8l^3-4l)^3} + \frac{1}{(16l^4-12l^2+1)^3} + \frac{1}{(32l^5-32l^3+6l)^3} + \frac{1}{(64l^6-80l^4+24l^2-1)^3} + \frac{1}{(128l^7-192l^5+80l^3-8l)^3}; \tag{4.6}$$

$$\frac{dW}{d\delta^*} = \begin{cases} \dfrac{1}{128l^2(l^2-1)(2l^2-1)^3} - \dfrac{3l(4l^2-3)}{2(l^2-1)(4l^2-1)^4} + \dfrac{l}{2(l^2-1)(4l^2-1)^3} \\ \quad - \dfrac{8l^4-8l^2+1}{128l^4(l^2-1)(2l^2-1)^4} + \dfrac{1}{16l^2(l^2-1)} - \dfrac{2l^2-1}{16l^4(l^2-1)} & \text{for } l > 2; \\ 0.24 - \frac{2.3\times10^{-4}}{\delta^{*1/2}} - 0.31\delta^{*1/2} + 0.066\delta^* + 0.098\log\delta^* - \frac{2.06\times10^{-4}\log\delta^*}{\delta^{*1/2}} & \text{for } l \le 2 \end{cases} \tag{4.7}$$

where $l = \delta^* + 1$ is the non-dimensionalized sphere center-to-wall distance.

Then, the added mass force exerted on the sphere as it approaches to a wall can be calculated as

$$\tilde{f}_{AM} = -\frac{1}{2}m_l\frac{dU}{dt} - \frac{3}{2}m_l W(\delta^*)\frac{dU}{dt} + \frac{3}{4}m_l\frac{U^2}{a}\frac{dW(\delta^*)}{d\delta^*}. \tag{4.8}$$

with the wall effect terms defined in equations (4.6) and (4.7).

4.2.3 History force

The history force, also known as Basset force, describes the force due to the lagging boundary layer development with changing relative velocity (acceleration or deceleration) of a body moving through a viscous fluid (see Crowe *et al.*, 1998*b*). It is a direct consequence of non-constant vorticity generation at an unsteady solid surface, which affects the boundary layer development as compared to the growth on a surface moving with constant velocity. The varying boundary layer interacts with the unsteady surface motion resulting in a viscous force that is not accounted for by a quasi-steady drag. The history force is difficult to implement and is commonly neglected for practical reasons; however, it can be substantially larger than the added mass force when the body is accelerated at a high rate.

After solving the creeping flow with a low Reynolds number, Boussinesq (1885) and Basset (1888)

found the total hydrodynamic force for a sphere moving with velocity $U(t)$ in an unbounded viscous liquid as:

$$f = -6\pi\mu a U(t) - \frac{1}{2} m_l \frac{dU}{dt} - 6\pi\mu a^2 \frac{1}{\sqrt{\pi\nu}} \int_0^t \frac{dU}{d\tau} \frac{d\tau}{\sqrt{t-\tau}}. \tag{4.9}$$

where the first two terms are the steady drag force and the added mass force. The third term is the history force, which is calculated as a time integral that depends on the acceleration history of the sphere and a time kernel $K(t-\tau) = (t-\tau)^{-1/2}$. The time kernel describes the local dissipation mechanism and diminishes the effect of the history force due to the earlier sphere acceleration. Coimbra *et al.* (2004) confirmed the decay rate 1/2 for Stokes flows by their experiments involving an oscillating flow over a stationary sphere in which the flow unsteadiness was limited to high frequency and small amplitude.

To extend the history force for a moderate Reynolds number flow, numerical simulations were performed to investigate the unsteady hydrodynamic forces on a solid sphere. When preserving the forms of drag force and the added mass force, Mei & Adrian (1992) developed a new time kernel $K_{MA}(t-\tau, Re)$ for the history force through regular perturbation with low frequency. The term $K_{MA}(t-\tau, Re)$ has a form in which a faster decay as $(t-\tau)^{-2}$ is dominant when the Reynolds number is higher. Thus the history force has a shorter memory of flow disturbance at early times, as compared to $(t-\tau)^{-1/2}$ for low Reynolds number.

Kim, Elghobashi & Sirignano (1998) further extended Mei and Adrian's results by including unsteadiness from low to high frequencies and small to large amplitudes. A new time kernel is proposed as

$$K(t-\tau, Re) = \left\{ \left[\frac{\pi(t-\tau)\nu}{a^2} \right]^{1/2C_1} + G(\tau) \left[\frac{\pi |U(t)|^3 (t-\tau)^2}{2a\nu g_H^3(Re)} \right]^{1/C_1} \right\}^{-C_1} \tag{4.10}$$

where $g_H(Re) = 0.75 + C_2 Re$ is a fitted function, $C_1 = 2.5$ and $C_2 = 0.126$. $G(\tau)$ is a weight function of the primary and the secondary flow acceleration number, with $M_1(\tau) = (2a/U^2)|dU/d\tau|$ and $M_2(\tau) = (2a^2/|U^3|)|d^2U/d\tau|^2$, as $G(\tau) = 1/\left[1 + \beta(\tau)\sqrt{M_1(\tau)}\right]$. A second fitted function, $\beta(\tau) = C_5/\{1 + \phi_r^{1+C_4}/[C_3(\phi_r + \phi_r^{C_4})]\}$, depends on the acceleration ratio, $\phi_r(\tau) = M_2(\tau)/M_1(\tau)$

with $C_3 = 0.07$, $C_4 = 0.25$, $C_5 = 22.0$. This time kernel covers both of the previous results for creeping flow and for moderate Reynolds number flow with a complete range of oscillating conditions.

As summarized by Yang (2006), various history kernels have been proposed that focus on the long-time behavior of the history force beside the above citations. Different velocity variations, including an impulsive start or stop, constant acceleration, and a step velocity change, have been employed to evaluate the unsteady drag on a solid body (see Hinch, 1993; Lovalenti & Brady, 1993; Lawrence & Mei, 1995; Chaplin, 1999). The history kernels for the different flows have different forms: $K(t-\tau) \sim e^{-(t-\tau)}$, $(t-\tau)^{-n}$, or $(t-\tau)^{-n}e^{-(t-\tau)}$ with $n > 1/2$. However, experimental result that can validate the long-term history force behavior is absent.

The influence of the existence of a solid wall on the history force exerted on a moving sphere was investigated by Yang (2006) based on a similar technique as used for the added mass force. Based on a wall-modified potential function, a modified history force different from the no-wall results was formulated by examining the effect of the potential pressure field on the boundary layer development as:

$$\tilde{f}_H = -6\pi\mu a K_H(\delta^*)^{3/2} \int_0^t \frac{dU}{d\tau} K(t-\tau) d\tau \tag{4.11}$$

where $K_H(\delta^*)$ is the the wall-effect factor and it has a form with $l = \delta^* + 1$ as

$$\begin{aligned} K_H(\delta^*) = 1 + \frac{0.375 - 0.03125/(1-2l^2)^3}{l^3} - \frac{3}{(1-4l^2)^3} - \frac{0.015625}{(l-2l^3)^3} \\ + \frac{1}{(1-12l^2+16l^4)^3} + \frac{0.375}{(3l-16l^3+16l^5)^3}. \end{aligned} \tag{4.12}$$

The argumentation factor, to the order of l^{-15}, is found to increase monotonically with diminishing δ^*.

Yang (2006) did pendulum-wall collision experiments and validated the history force with the wall-modified factor (4.12) and also the kernel (4.10). For a particle-wall collision process, a short-term characterization of $\tilde{f}_H$ is more important. Thus, the expression (4.11) with (4.10) and (4.12) is used to calculate the history force exerted on a sphere in the following contact model.

4.2.4 Liquid-solid force term in the contact model

The formulas for the hydrodynamic forces exerted on a sphere moving in a liquid environment developed by Yang (2006) provide a direct and simple source for modeling the liquid-solid interaction force in a numerical simulation for a sphere-wall collision process when the sphere is close to the wall and the resolution is insufficient.

As a first step, the computed results obtained from a numerical simulation for a sphere falling toward a wall under gravity are compared with the results calculated from the theoretical expressions developed by Yang (2006). To obtain the simulated and analytical results, the experimental results from the current experiments described in chapter 2 are used. Sixth order polynomial curves are employed to fit the measured trajectories so that the velocity and acceleration of the sphere at different times can be calculated by differentiating the polynomial. The fitting curves are used to prescribe the motion of the sphere in the numerical simulation. The force obtained from the simulation is still marked as $\tilde{f}_{\text{SIM}}$. For the analytical results, the total hydrodynamic force is calculated as:

$$\tilde{f}_{\text{THR}} = \tilde{f}_D + \tilde{f}_{AM} + \tilde{f}_H \tag{4.13}$$

where $\tilde{f}_D$ is the Stokes drag force calculated from equation (4.1) and (4.4) with the wall correction term (4.3); the added mass force $\tilde{f}_{AM}$ is calculated from equation (4.8) with the wall correction terms (4.6) and (4.7); the history force $\tilde{f}_H$ is calculated from equation (4.11) with the wall correction term (4.12) and the time kernel (4.10). The smooth velocity and acceleration profiles calculated by differentiating the polynomial fitting curves are used in the equations mentioned above. After performing the numerical simulations and the corresponding calculations, the comparison shows that the simulated force matches with the theoretical result well at moderate gap and there is no deviation until the gap becomes small.

As an example, for a sphere moving with a prescribed trajectory obtained from the experimental case 3 with particle impact Reynolds number $Re = 90$, the hydrodynamic forces are plotted as a function of the non-dimensional gap between the sphere and the wall, $\delta = h/D$, as well as its wall

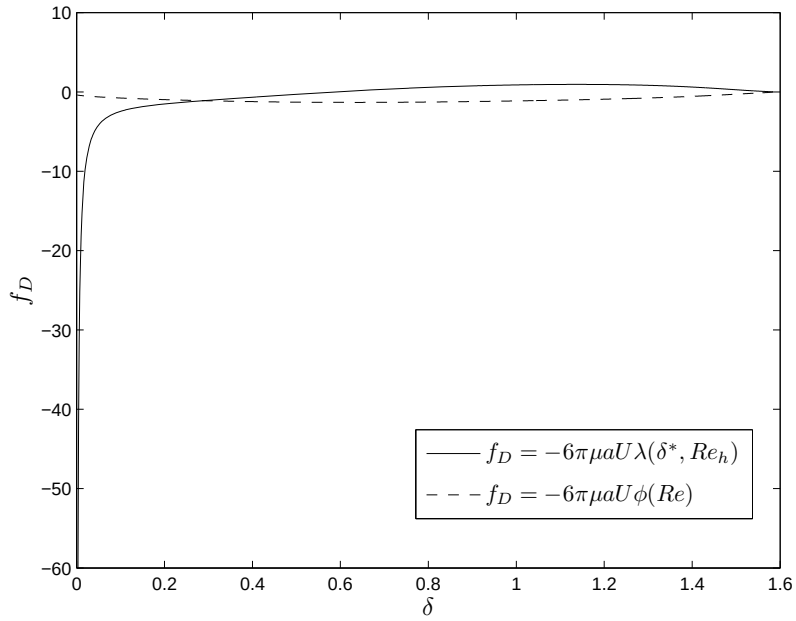

Figure 4.2: The Stokes drag as a function of the gap

correction coefficient.

The Stokes drag forces calculated with the Reynolds number correction and the wall correction are shown in figure (4.2) respectively as solid line and dashed line. The force is non-dimensionalized by $\frac{4}{3}\pi a^3\rho_l g$ and denoted as f_D without the hat tilde. The same non-dimensionalization is performed for all the other forces. The wall correction term for the Stokes drag force, $\lambda(\delta^*, Re_h)$, is plotted in figure (4.3). When the gap is large ($\delta > 0.6$), the calculated result is negative, which is not correct since equation (4.3) is for small gap. As shown in figure (4.2), the results obtained from the two different formulas have a matching range around $\delta = 0.3$ so that the value calculated with the Reynolds number correction is used for $\delta > 0.3$ and the value calculated with the wall correction is used for $\delta < 0.3$. The magnitude of the drag force increases dramatically with the diminishing gap. It plays a dominant role in the hydrodynamic forces exerted on the sphere when it is about to collide with a wall.

Similarly, the non-dimensional added mass force f_{AM} and its wall correction terms $W(\delta^*)$ and $dW(\delta^*)/d\delta^*$ are plotted as a function of the gap as shown in figure (4.4) and (4.5). The non-

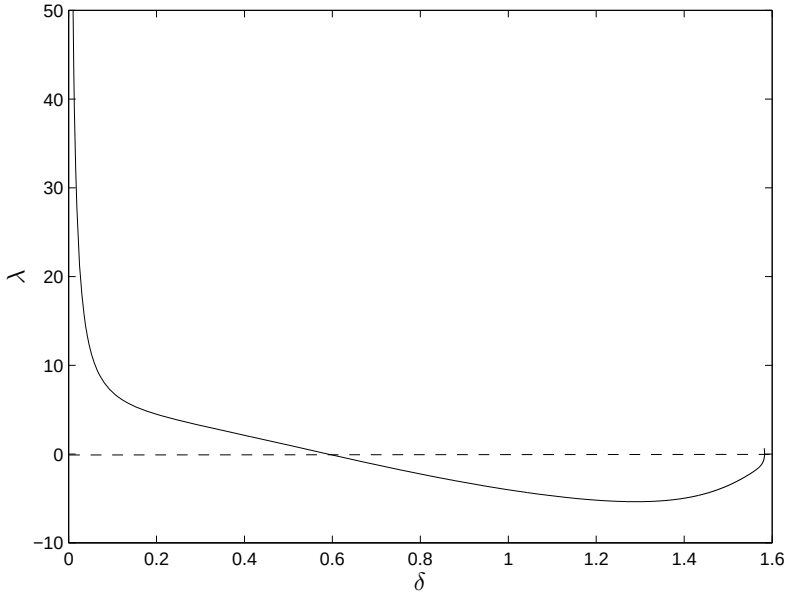

Figure 4.3: Wall correction term for Stokes drag as a function of the gap

dimensional history force f_H and its wall correction term $K_H(\delta^*)$ are plotted in figure (4.6) and (4.7).

After comparing the results in figure (4.2), (4.4) and (4.6), the magnitude of the added mass force and the history force are smaller than the Stokes drag force when the sphere is approaching to the wall. The total force effect as $f_{\text{THR}} = f_D + f_{AM} + f_H$ when the sphere is close to the wall is plotted as a dashed line in figure (4.8).

In the same figure, the simulated result obtained from a numerical simulation by prescribing the motion of the sphere with the measured trajectory from the experiment case 3 is plotted as a solid line. The two results match well when the gap is moderate. The results deviate when the gap is less than 0.1 and there is insufficient resolution in the numerical simulation.

To resolve the flow when the gap is small, a liquid-solid interaction model is proposed that blends the simulated and the theoretical forces whenever the gap decreases below a threshold value, δ_{SL}. The solid-liquid force, $\tilde{f}_{\text{SL}}$ is obtained as

$$\tilde{f}_{\text{SL}} = H\left(\frac{\delta}{\delta_{\text{SL}}}\right)\tilde{f}_{\text{THR}} + [1 - H\left(\frac{\delta}{\delta_{\text{SL}}}\right)]\tilde{f}_{\text{SIM}}, \tag{4.14}$$

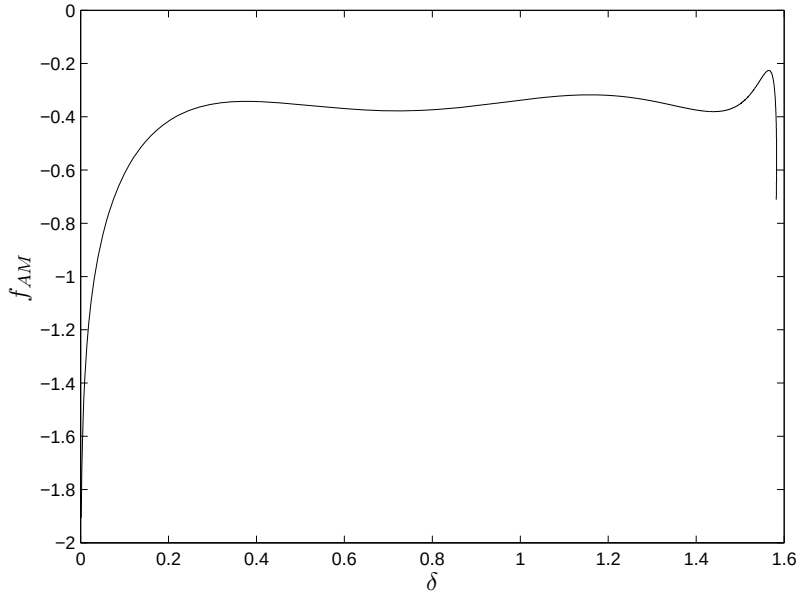

Figure 4.4: The added mass force as a function of the gap

where

$$H\left(\frac{\delta}{\delta_{\text{SL}}}\right) = \frac{1}{1+e^{10\left(\frac{\delta}{\delta_{\text{SL}}}-1\right)}} \tag{4.15}$$

is a smoothed Heaviside function, as shown in figure (4.9). Based on figure (4.8), δ_{SL} is conservatively taken as 0.2. Clearly, the necessary value of δ_{SL} depends on the grid resolution of the fluid simulation. The finer the grid, the smaller the value of δ_{SL} that could be used. On the other hand, it seems reasonable to fix the value at a conservative value independent of the grid resolution.

Thus, for a sphere approaching a wall, the hydrodynamic force exerted on it is computed directly from the simulation when the distance between the sphere and the wall is large ($\delta > 0.4$); the analytical results start to be counted in when $\delta < 0.4$ and the hydrodynamic force has a form:

$$\tilde{f}_{\text{SL}} = \frac{1}{2}\tilde{f}_{\text{THR}} + \frac{1}{2}\tilde{f}_{\text{SIM}}$$

at $\delta = 0.2$; when the sphere is about to collide with the wall, the hydrodynamic forces are taken as the values calculated from the analytical expressions as the gap decreases to zero.

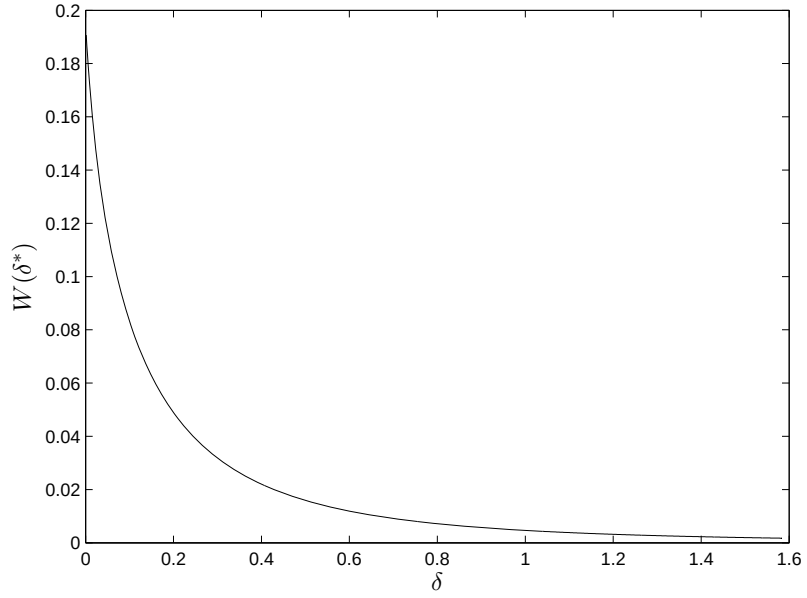

(a)

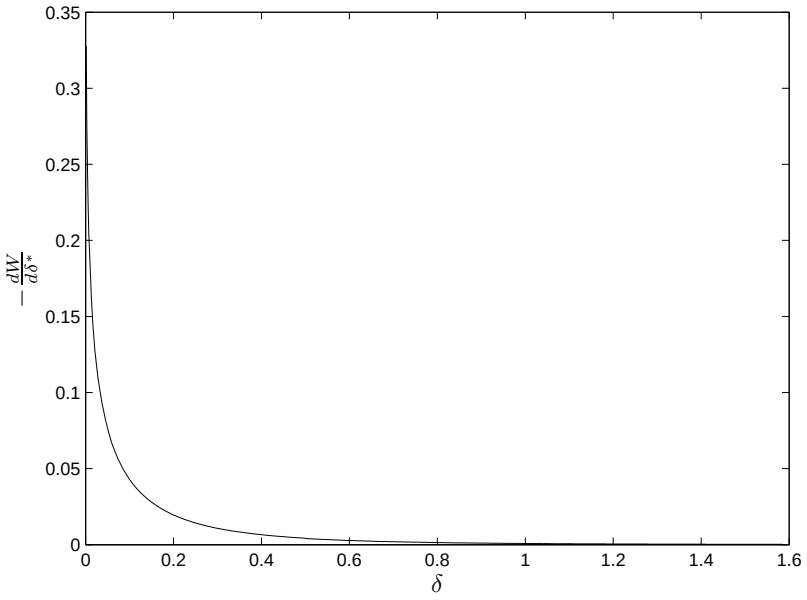

(b)

Figure 4.5: The wall correction term for added mass as a function of the gap

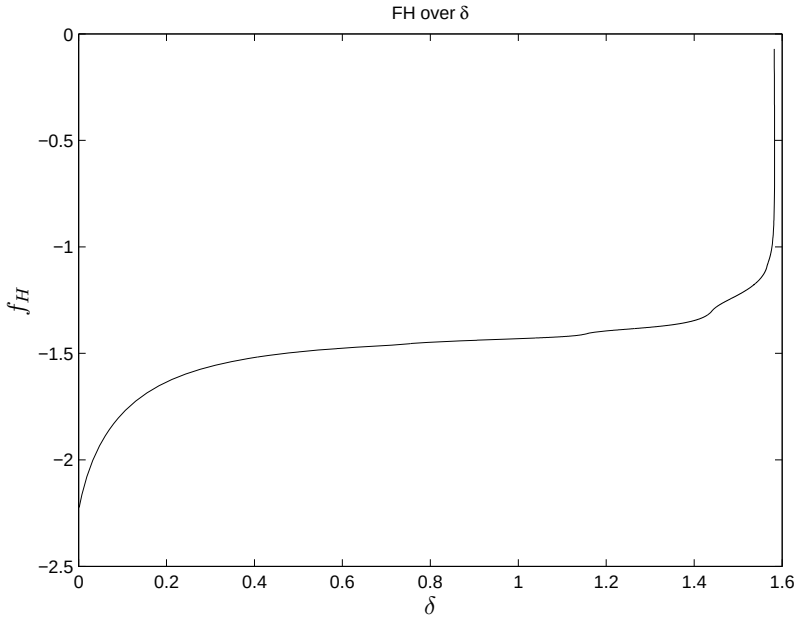

Figure 4.6: The history force as a function of the gap

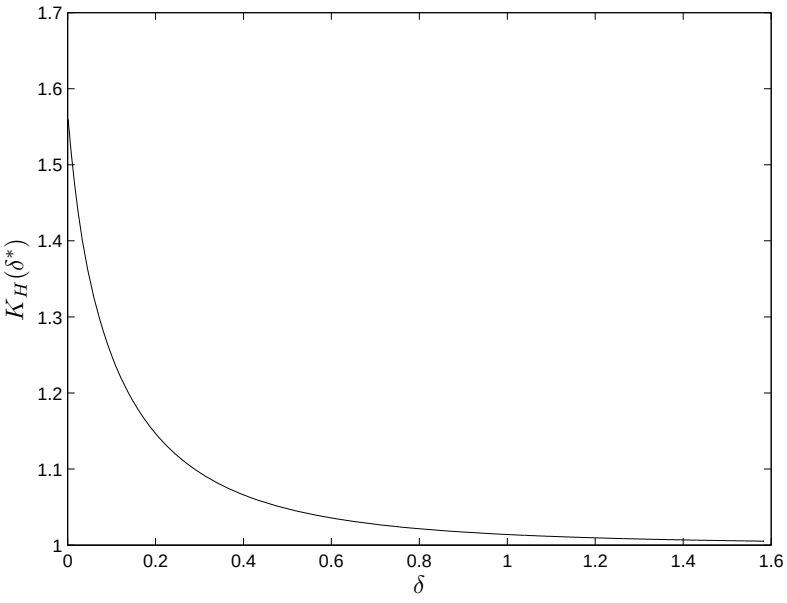

Figure 4.7: The wall correction term for history force as a function of the gap

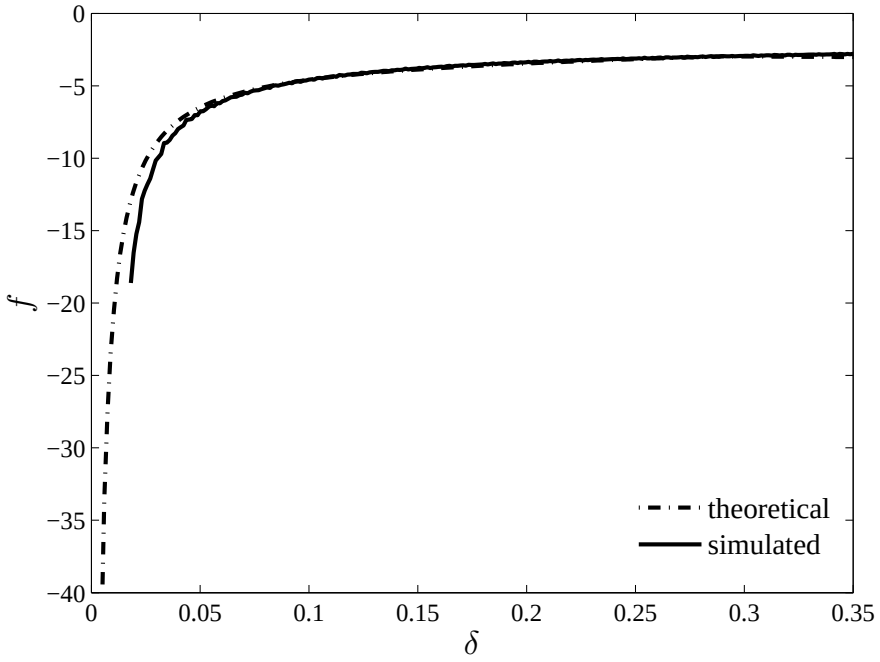

Figure 4.8: The liquid-solid interaction force for a impact process with $Re = 90$.

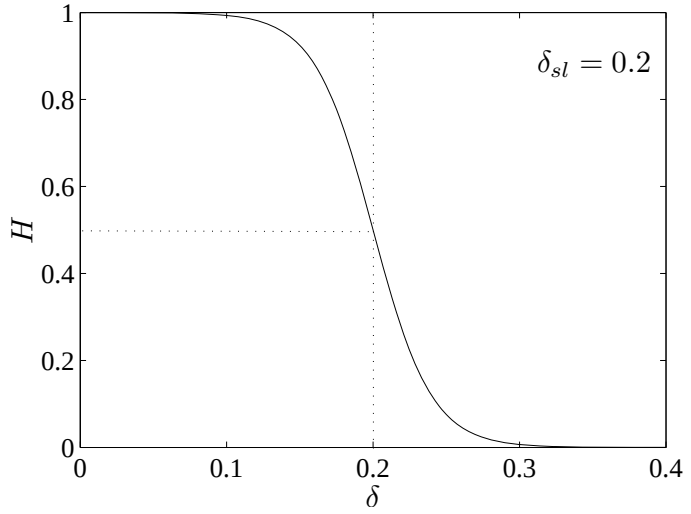

Figure 4.9: The smooth Heaviside function H for $\delta_{\mathrm{SL}} = 0.2$.

4.3 Elastic effect of the solid parts

The hydrodynamic forces discussed in section 4.2 increase rapidly as a sphere approaches a wall and dissipate the kinetic energy of the system. At an extreme, the velocity decreases to zero so that the sphere stops and rests on the wall, as shown in the settling experiments in chapter 2. However, part of the kinetic energy is stored when the incoming velocity is large and the sphere has more inertia. This kinetic energy is transformed into elastic-strain energy so that the sphere deforms and rebound may occur.

In elastohydrodynamic theory, the two deformable solid surfaces are assumed to be smooth and to be separated by a thin incompressible Newtonian fluid layer that prevents the surfaces from actually touching. A large hydrodynamic pressure builds up as the fluid is squeezed out from the gap between the sphere and the wall and causes the elastic solid to deform. Davis, Serayssol & Hinch (1986) first simultaneously accounted for elastic formation and viscous fluid forces by describing the deformation of the sphere following the development of Hertz contact theory of linear elasticity. Lubrication theory is employed to couple the deformation geometry with the pressure profile of the interstitial liquid. They were not able to obtain the analytical solution for the dynamic deformation and viscous forces. Wells (1993) and Lian, Adams & Thornton (1996) proposed their more simplified models where the dynamic deformation of the spheres was assumed to be Hertzian-like and presented approximate analytical solutions for the evolution of the relative particle velocity, force and restitution coefficient.

In the current work, the coupling between the elastic solid mechanics and fluid dynamics is interpreted in another way. The hydrodynamic force building up in the interstitial fluid is incorporated in the liquid-liquid interaction term $\tilde{f}_{\mathrm{SL}}$ since the analytical expressions with the wall correction terms converge to the lubrication theory with diminishing gap between the sphere and the wall. The deformation of the solid surfaces are not included in the numerical simulations. However, the conversion between the kinetic energy and the elastic-strain energy is represented by adding an additional term into the equation of the sphere motion based on the Hertz contact theory. When the gap between the two solid surfaces decreases below a threshold value, the solid elastic term starts to take effect

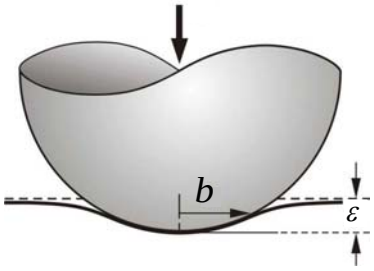

Figure 4.10: Schematic of a contact between a sphere and an elastic half space.

decreasing the impacting velocity and making the sphere rebound.

4.3.1 Hertz contact theory

Hertz contact theory investigates the local stresses that develop as two curved surfaces come into contact and deform slightly under an imposed load. It is named after Heinrich Hertz, who initiated the study of the deformation of solids that touch each other (see Hertz, 1882) and provided many important ideas for the development of contact mechanics.

For an elastic sphere with radius a indenting an elastic half-space to depth ε, with a contact area of radius b, as shown in figure (4.10), the contact force calculated from the Hertz contact theory (see Johnson, 1985) is:

$$W = \frac{4}{3} E^* a^{1/2} \varepsilon^{3/2} \tag{4.16}$$

where $E^* = [(1-\nu_1^2)/E_1 + (1-\nu_2^2)/E_2]^{-1}$ is the reduced modulus based on the Young's Modulus, E, and the Poisson ratio, ν, for the two materials. The indentation depth ε is related to the impacting velocity as $V = \frac{d\varepsilon}{dt}$. The equation of motion of the sphere can be described as:

$$m_p \frac{d^2\varepsilon}{dt^2} = -\frac{4}{3} E^* \sqrt{a} \varepsilon^{3/2} \tag{4.17}$$

Solving this equation with an initial condition $\frac{d\varepsilon}{dt} = V_I$ when $\varepsilon = 0$ yields:

$$\frac{d\varepsilon}{dt} = \sqrt{V_I^2 - \frac{16 E^* \sqrt{a}}{15 m_p} \varepsilon^{5/2}}$$

At the end of the elastic deformation process, the maximum depth is given when $V = \frac{d\varepsilon}{dt} = 0$. So:

$$\varepsilon_{\max} = \left(\frac{15 m_p V_I^2}{16 E^* \sqrt{a}}\right)^{2/5}$$

Thus, the maximum elastic force for a spheres with an impacting velocity V_I is:

$$W_o = \frac{4}{3} E^* \sqrt{a} \left(\frac{15 m_p V_I^2}{16 E^* \sqrt{a}}\right)^{3/5}$$

which can be simplified by applying $m_p = 4/3\pi a^3 \rho_p$ into:

$$W_o = \frac{4}{3} a^2 E^* \left(\frac{5\pi}{4E^*} \rho_p V_I^2\right)^{3/5} \tag{4.18}$$

4.3.2 Elastic effect term in the equation of motion

Based on the expression (4.18) of the maximum Hertz elastic force achieved during a collision process for an elastic sphere and an elastic wall, an elastic force is proposed for the contact model as:

$$\tilde{f}_{\text{ss}} = F\left(\frac{\delta}{\delta_{\text{ss}}}\right) e_d W_o, \tag{4.19}$$

where the subindex $_{\text{ss}}$ indicates the elastic force results from the approaching of the two solid surfaces. The dry coefficient of restitution e_d is taken as 0.97 as mentioned in Chapter 1, which incorporates the inelasticity. The function $F\left(\frac{\delta}{\delta_{\text{ss}}}\right)$ is used to introduce the elastic effect gradually after the gap between the sphere and the wall decreases below a threshold value, δ_{ss}; W_o is the maximum elastic force calculated from equation (4.18) where the impact velocity V_I is taken to be the value when $\delta = \delta_{\text{ss}}$. Different forms of the function $F\left(\frac{\delta}{\delta_{\text{ss}}}\right)$ have been tried and the one that produces the best fit for the particle trajectory has the following form:

$$F\left(\frac{\delta}{\delta_{\text{ss}}}\right) = \begin{cases} \frac{e^{\left(-\frac{\delta}{\delta_{\text{ss}}}\right)} - e^{-1}}{1 - e^{-1}}, & 0 \le \delta \le \delta_{\text{ss}}; \\ 0, & \delta > \delta_{\text{ss}}. \end{cases} \tag{4.20}$$

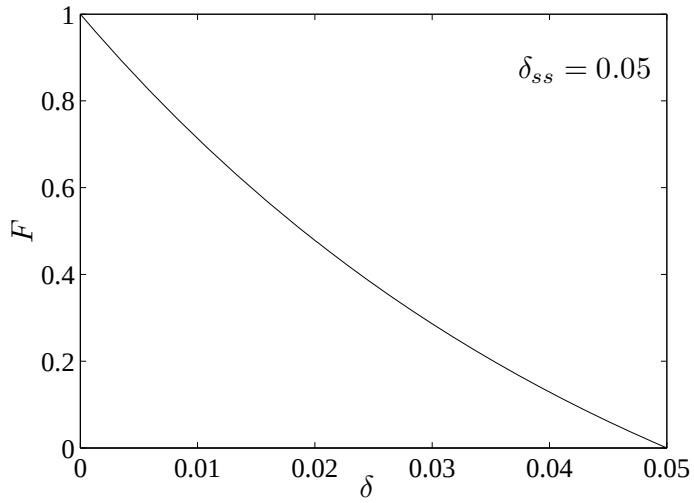

Figure 4.11: F function for $\delta_{\text{ss}} = 0.05$

The dependence of F on the gap is plotted in figure (4.11).

Thus, when the gap is large, there is no elastic effect on the sphere; however, when the gap decreases and approaches zero, the elastic effect increases and approaches the maximum elastic force achieved in a dry collision. This additional elastic force term converts the kinetic energy of the impacting sphere and make it rebound. The non-dimensional parameter δ_{ss}, is the threshold where the elastic force starts to take effect and it plays an important role in the contact model. The choice of the value and physical meaning of δ_{ss} will be discussed in detail in Chapter 5.

At distance $\delta < \delta_{\text{ss}}$, the velocity of the impacting sphere decreases dramatically due to the elastic force and becomes zero when the gap between the sphere and the wall reaches a minimum value. The velocity of the sphere keeps decreasing to negative (opposite direction) value so that the sphere rebounds under the elastic effect until the growing gap exceeds the threshold value δ_{ss}.

4.4 Contact model for normal sphere-wall collisions

After including the liquid-solid interaction force term and the elastic effect term, the final equation of the motion in the vertical direction with the contact model is written as:

$$m_p \frac{d\tilde{V}}{d\tilde{t}} = \tilde{f}_{\text{SL}} + \tilde{f}_{\text{SS}} + m_p g + \tilde{f}_b, \tag{4.21}$$

It can be non-dimensionalized after applying the same characteristic length $L_o = D$ and time $t_o = \sqrt{D/g}$:

$$\tau \frac{dV}{dt} = f_{\text{SL}} + f_{\text{SS}} + \tau - 1, \tag{4.22}$$

where $\tau = \rho_p/\rho_l$ is the density ratio, f_{SL} and f_{SS} are the non-dimensional liquid-solid interaction and elastic forces. After coupling the equation (4.22) with the evolution of the flow field:

$$\frac{\partial \mathbf{u}}{\partial t} + \mathbf{u} \cdot \nabla \mathbf{u} = -\nabla p + \frac{1}{Re} \nabla^2 \mathbf{u} + \int_s \mathbf{f}(\boldsymbol{\xi}(s,t)) \delta(\boldsymbol{\xi} - \mathbf{x}) ds$$

and the boundary condition:

$$r\boldsymbol{u}(\boldsymbol{\xi}(s,t)) = \int_{\boldsymbol{x}} r\boldsymbol{u}(\boldsymbol{x}) \delta(\boldsymbol{x} - \boldsymbol{\xi}) d\boldsymbol{x} = r_B \boldsymbol{u}_B(\boldsymbol{\xi}(s,t)),$$

both the motion of the sphere before and after the collision process can be computed with known input parameters based on the initial distance, the gravitational acceleration, the solid-liquid density ratio, the diameter of the sphere, and the viscosity of the liquid.

Chapter 5

Simulations and results

The numerical method described in Chapter 3 solves the evolution of the flow field and the coupled dynamic behavior of a sphere moving in the flow. When there is an additional solid boundary (a solid wall) existing in the flow field, the impact and rebound behavior of the sphere can be calculated by including the contact model introduced in Chapter 4. The experiments presented in Chapter 2 provide an effective validation for the proposed contact model since the sphere is released from zero velocity under quiescent ambient fluid condition, which makes the initial condition for the simulation easy to enforce. Thus the numerical simulations for the different experimental cases are performed with the corresponding initial conditions and material properties described in Chapter 2. After comparing the calculated trajectory with different δ_{ss} to the measured result in a single case, a unique value for δ_{ss} that results in the best fit to the experimental trajectory is chosen to complete the proposed contact model. The accuracy of the contact model over different Reynolds numbers is discussed by comparing trajectories and calculating the difference on the maximum height achieved in rebound process. Besides the particle trajectories, the velocity profiles, the evolution of the vorticity distribution of the flow field and the coefficient of restitutions are also investigated.

5.1 Simulation setup

To simulate the settling process of a sphere and the evolution of the surrounding flow field as described in the experiments in Chapter 2, a three-level computational multi-domain is used to enforce the same boundary conditions as used in the experiments as shown in figure (5.1). The

releasing surface and the target wall are represented with two segments fixed in the computational domain which make two plates in the axisymmetric system. A half circle which represents the sphere is initially placed $2dz$ away from the releasing surface to avoid a direct contact of the two solid bodies that may cause a singularity problem in simulation, where $dz = dr = 0.01D$ is the uniform grid size for the first level computational domain in figure 5.1(a)) For the second level computational domain (figure 5.1(b)) that is twice the size of the first domain, the grid size is $dz_2 = dr_2 = 2dz = 0.02D$. Similarly, the grid size for the third level domain is $dz_3 = dr_3 = 2^{(3-1)}dz = 0.04D$ (figure 5.1(c)). A far field boundary condition (slip but non-penetrating) is applied at the boundary of the third level computational domain as required by the numerical method. For the symmetric axis $r = 0$, the boundary condition is strictly satisfied. For the other three boundaries, the slip-non-penetrating boundary condition for the large domain with coarser mesh is appropriate since the tank used in the experiments is large and accordant with the third domain.

The coupled systems are non-dimensionalized with characteristic length, the diameter of the sphere, $L_o = D$, and characteristic time $t_o = \sqrt{D/g}$ where $g = 9.8$ m/s^2 is the gravitational acceleration. The Navier-Stokes equations have a non-dimensional parameter $Re_g = D\sqrt{Dg}/\nu$ and the velocity variable can be non-dimensionalized by $\sqrt{Dg}$. For the different experiments described in Table (2.2), the Reynolds number, Re_g, for the Navier-Stokes equations are slightly different since although the same sphere is used in these different cases but the dynamic viscosity of the liquid changes slightly when room temperature varies. The initial distance of the sphere from the target wall is different in the experiments. Correspondingly, the position of the target wall is defined at different value in the simulation for different case. In the equation of the sphere motion, the density ratio of the sphere to the liquid, $\tau = \rho_p/\rho_l$, also varies slightly with the temperature. The simulations start from $t = 0$ when the sphere is $0.02D$ away from the releasing surface with zero velocity and the flow field is static. The effect of gravity and buoyancy results in an acceleration and the sphere starts to move. The motion is coupled with the evolution of the flow field with a second order Runge-Kutta method as discussed in Chapter 3. The analytical formulas with the wall correction terms for the hydrodynamic forces are not used when the sphere is just released from the

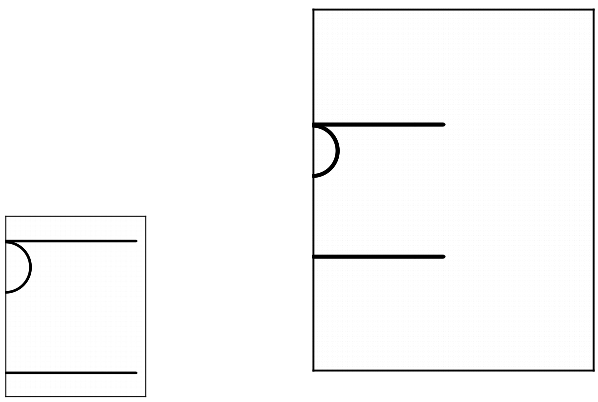

(a) grid level 1

(b) grid level 2

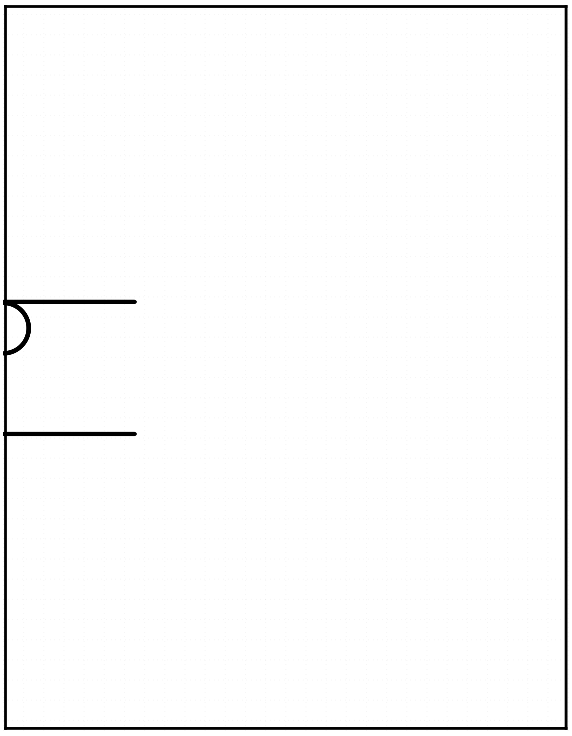

(c) grid level 3

Figure 5.1: The initial setup for the 3-level multi-domain.

releasing surface since the velocity of the sphere is very small, which makes the dominant drag force much smaller than the result when the sphere is about to collide with the target wall.

5.2 Calibration of δ_{ss}

The non-dimensional parameter δ_{ss} from the contact model plays an important role in the simulation for a collision process. As explained in Chapter 4, δ_{ss} is the threshold distance where the elastic-like force starts to take effect. When $\delta < \delta_{ss}$, the elastic-like force becomes dominant since its magnitude is very large compared with the other hydrodynamic forces and gravity. The velocity of the sphere decreases rapidly and becomes negative (sphere moves in opposite direction) under the effect of the elastic-like force. Thus, the value of δ_{ss}, influences the rebound trajectory of the sphere. The effect of δ_{ss} on the collision process is shown in figure (5.2).

In figure (5.2), the computed trajectories from simulations of the experimental case 3 with different values of δ_{ss} are compared. The vertical and horizontal axes represent the dimensionless gap between the sphere and the wall, δ and the dimensionless time, t, respectively. The value of δ_{ss} is taken to be small, ranging from $0.016D$ to $0.020D$, since the elastic force is irrelevant until the two solid surfaces are very close to each other. The first impacting process is not affected by the value of δ_{ss}. However, the rebound trajectory is different. Larger values of δ_{ss} result in smaller maximum height achieved in the rebound process.

To calibrate the value of δ_{ss}, the trajectory measured from the experiment case 3 is compared with the simulated result, as shown in figure (5.3). To distinguish the experimental points, the experimental data are presented in 2 ms time interval omitting the intermediate points. The simulation using $\delta_{ss} = 0.017$ gives the best fit for the first two rebounds. Thus $\delta_{ss} = 0.017$ is used to complete the proposed contact model. The adequacy of this value for the other collisions with different Reynolds numbers is investigated in the following section.

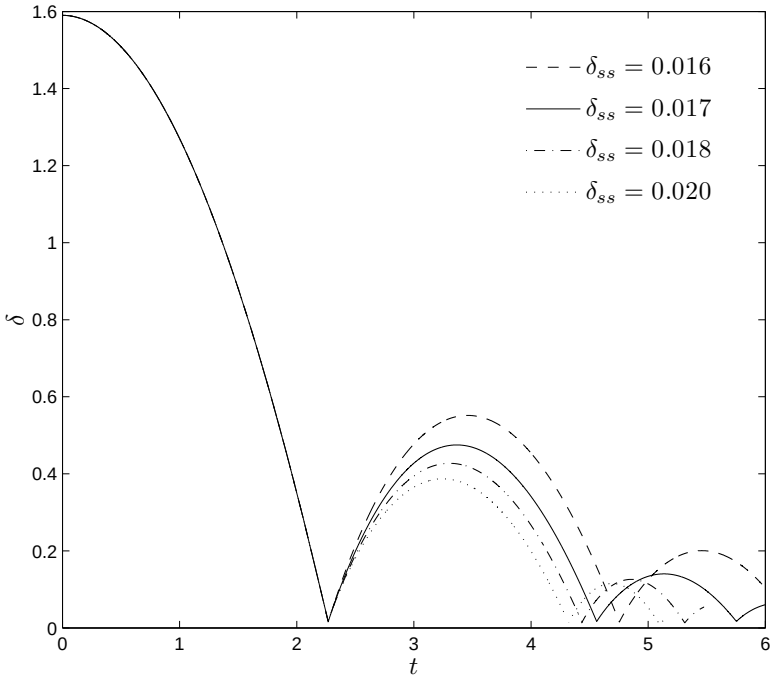

Figure 5.2: The simulated particle trajectories of case 3 with different $\delta_{\rm ss}$

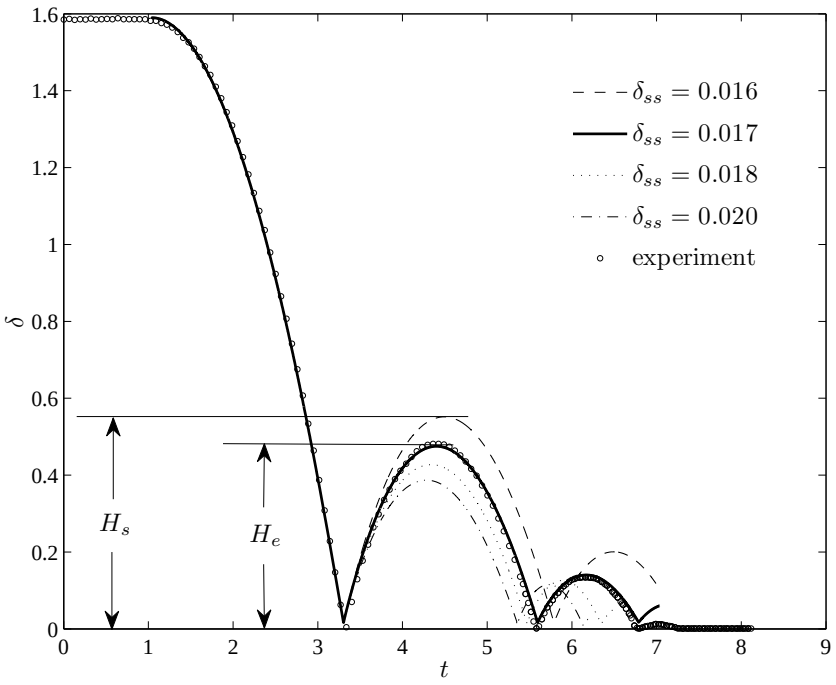

Figure 5.3: Comparison of the simulated trajectory to the measured trajectory of case 3

5.3 Particle velocity profile

The velocity profile for a sphere falling under gravity toward a solid wall in a viscous liquid environment is obtained from a numerical simulation with the contact model. The velocity decreases that have been observed in the current experiments are found in the simulated result.

Figure (5.4) shows the particle velocity in case 3 as a function of the gap between the particle and the wall. The velocity has been non-dimensionalized by $\sqrt{Dg}$. In figure 5.4(a), the particle starts to fall from $\delta = 1.6$ with zero velocity. The velocity increases as the gap decreases. The dashed line is an analytical result when only the gravitational and buoyancy forces are considered under the same initial condition. Thus, the difference between the solid line and the dashed line shows the viscous effect of the surrounding liquid on the motion of the particle. Figure 5.4(b) shows the enlarged details when the particle is about to collide with the wall. The impact velocity begins to decrease well before δ reaches δ_{SS}, where the elastic-like force resulting from the approaching of the two solid surfaces starts to take effect. This decrease in velocity results from the liquid-solid force that increases sharply as the gap, δ, diminishes. The particle decelerates before it rebounds. This phenomenon was observed in the current experiments, and also found in the experiments of Joseph *et al.* (2001) and the simulations of Ardekani & Rangel (2008). As the gap decreases to less than δ_{SS}, the elastic-like force stops the approach of the particle and makes it rebound. The rebound velocity has a sudden decrease after $\delta > \delta_{\text{SS}}$ that is shown in figure 5.4(c). The reason is because the elastic-like force falls to zero and the liquid-solid forces that always resist the sudden change of the relative velocity increases the viscous dissipation as more of the surrounding liquid re-enters the growing gap between the particle and the wall.

5.4 Qualitative flow features

The numerical simulation with the contact model captures not only the dynamics of the particles but also the evolution of the surrounding flow field during the falling and rebounding process. For the experimental case 7, figure 5.5(b) shows the snapshots of the vorticity field of the flow around

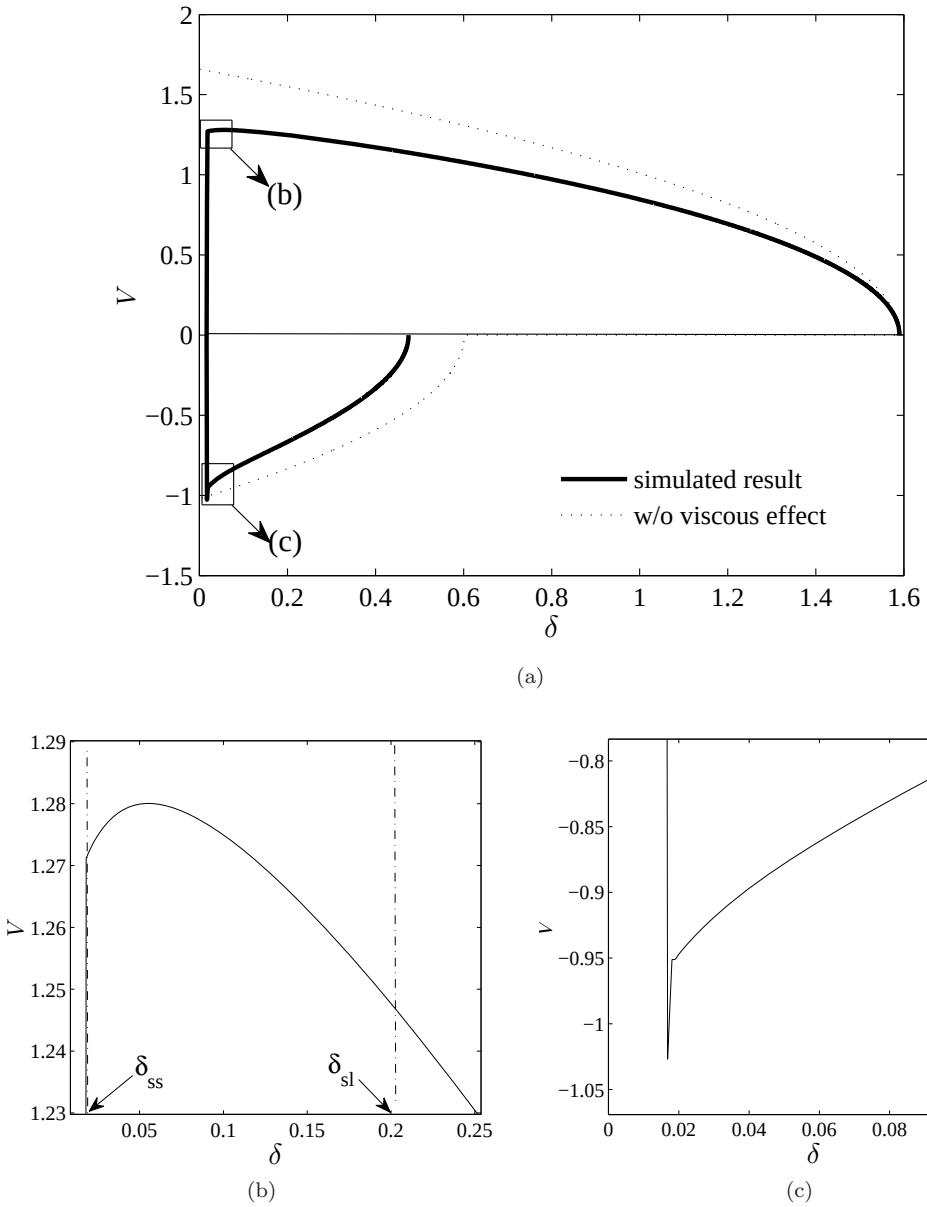

Figure 5.4: Velocity of the incoming and outgoing particle as a function of the gap between the particle and the wall. The solid line is the simulated result for case 3. The dashed line is the analytical result when just considering gravity and buoyancy effect on the particle and no liquid viscous effect. (b) and (c) present the enlarged details of the portions of (a) circumscribed in black rectangular boxes.

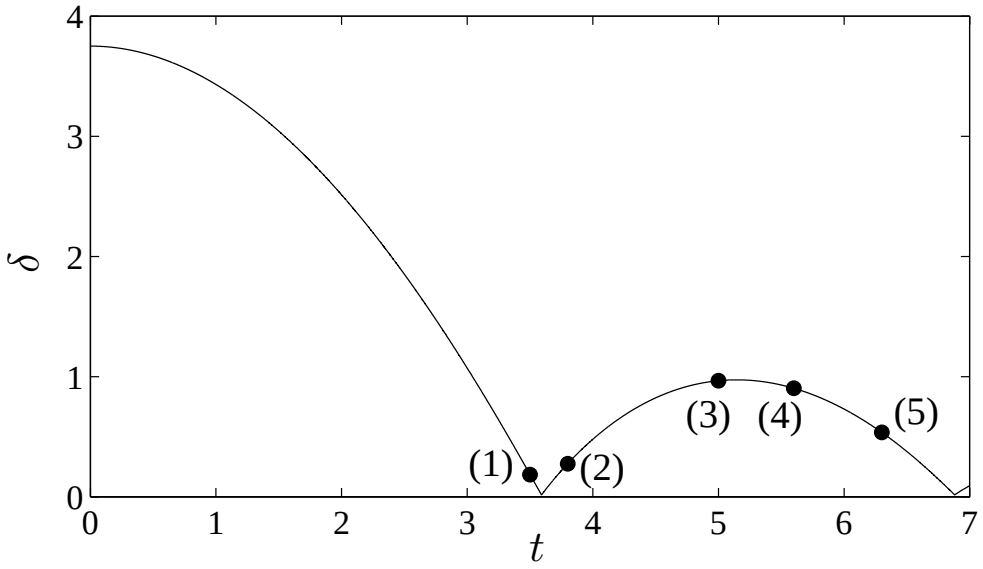

(a) particle trajectory

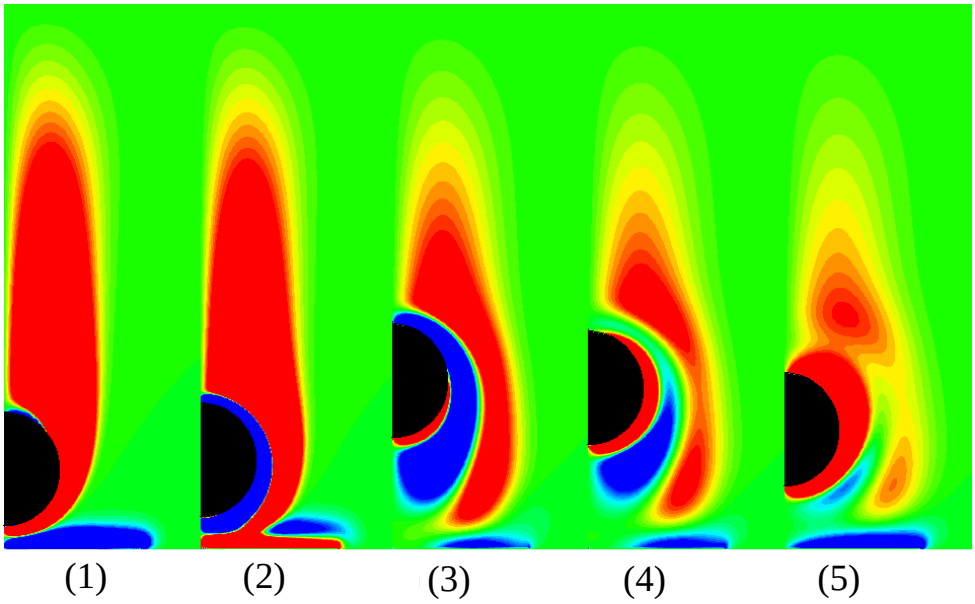

(b) Vorticity field

Figure 5.5: Snapshots of the vorticity field around the sphere at different time. Contour levels from -0.5 to 0.5 in increment of 0.05 are chosen for a good depiction of the weak vorticity field structure. The black semicircular area shows the location of the sphere. A smaller target wall is used and the release surface is omitted in this simulation.

the sphere at different times corresponding to the points on the trajectory in figure 5.5(a). The particle Reynolds number of the first impact is 134. Unlike the study of vorticity dynamics in Thompson, Leweke & Hourigan (2007) that prescribed the velocity of the sphere at a constant value and did not include the rebound, the current simulation solves the vorticity field when the sphere accelerates, decelerates and reverses directions. The first snapshot shows the primary vortex ring generated from the wake vorticity and the opposite-sign vorticity generated at the wall when the particle is just about to collide. The second snapshot is taken during the rebound after the first collision. The vorticity of opposite sign generates at the sphere surface as the rebounding sphere moves upwards through the primary wake ring to form a secondary vortex ring. Near the wall, the new vorticity forms as the result of the liquid re-entering the gap. As the sphere continues moving upwards, the primary vorticity is stretched and expanded as the sphere passes. A vortex-ring dipole forms from the combination of the primary and the secondary vorticity structures. The new positive vorticity attached to the bottom of the sphere shown in the third snapshot is formed because the sphere's velocity decreases to zero as it approaches the maximum height of the first rebound. When the sphere starts to fall again, the attached vorticity becomes a new stronger primary ring. The secondary vorticity is slowly dissipated by the surrounding opposite-sign vortices and the original primary vortex ring propagates radially before being stretched and merged with the new primary vorticity, as shown in the fourth and the fifth snapshots. The complex vorticity structure entangles the particle and dissipates a part of its kinetic energy.

5.5 Validation of the contact model

When the proposed contact model with the picked value $\delta_{\mathrm{ss}} = 0.017$ is applied to the collision processes with different Reynolds numbers in the experimental cases 1-7, the trajectories calculated from the simulation show good agreement with the experimental results for most of the cases. To estimate the deviation, a relative error defined as $\eta = (H_s - H_e)/H_e$ is used where H_s and H_e are the maximum height that the particle reached during rebound in the simulation and in the experiment, respectively, as indicated in figure (5.3).

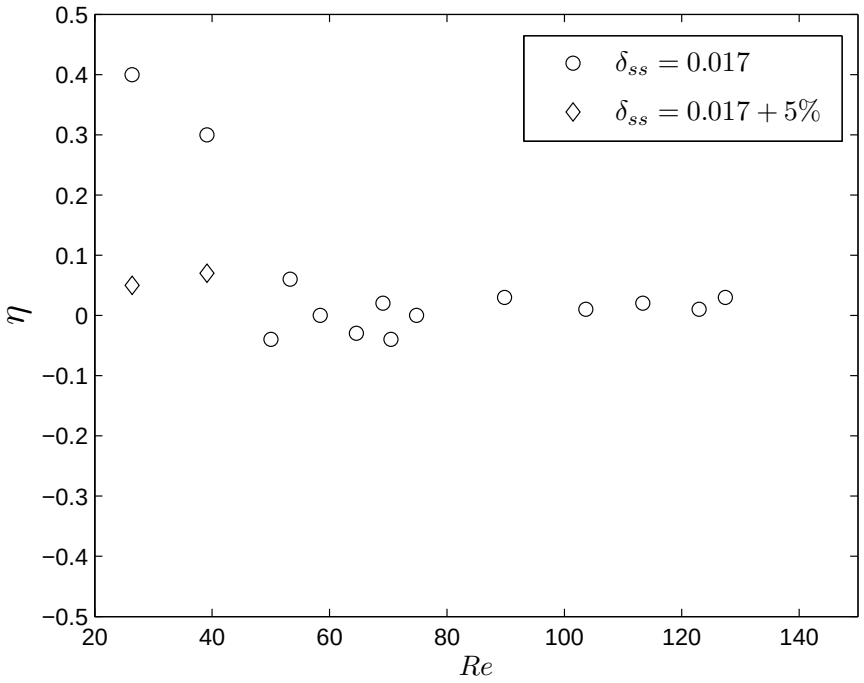

Figure 5.6: Relative error η based on maximum rebound height.

Figure (5.6) shows the relative error for the first and second impacts for each case. For the cases with Reynolds numbers ranging from 50 to 140, the relative error is small and within the uncertainty of the experiments. For smaller Re number, such as $Re = 29$, the simulation with $\delta_{\text{ss}} = 0.017$ results in a higher rebound than found in the experiment. The inaccuracy at low Re numbers is also seen in the third rebound in figure (5.3). To simulate the measured trajectory for lower Reynolds number, larger values of δ_{ss} are tried in different simulations since, as discussed in the previous section, a larger δ_{ss} results in a lower maximum height achieved in a rebound. The results are also shown in figure (5.6), which confirms that the relative error decreases when a larger δ_{ss} is used. With a 5% increase in δ_{ss}, the relative error falls within the uncertainty of the experimental region. The reason is discussed in section 5.7.

5.6 Discussion of the parameter δ_{ss}

In the current simulations, the calculated results are influenced by the value of the non-dimensional parameter δ_{ss} taken in the contact model. For Stokes number larger than 30, the simulations with $\delta_{ss} = 0.017$ produce the good agreement with experimental results for the trajectory and the coefficient of restitution. For Stokes number less than 30 but larger than 10 (runs 18-20 and runs 30-32), the simulation predicts a higher coefficient of restitution when using $\delta_{ss} = 0.017$; a lower coefficient of restitution that agrees with the experimental result is obtained when using $\delta_{ss} = 0.017 + 5\%$. The combined effect of the liquid-solid interaction and the elastic force terms is believed to be the reason. From equations (4.18) and (4.19), the elastic-like force depends on the impact velocity at δ_{ss}. In simulations with Stokes number less than 30, when $\delta_{ss} < \delta < \delta_{sL}$, the particle velocity decreases remarkably because of the effect of the liquid-solid interaction term, as discussed in section 5.3. Thus, a smaller impact velocity results in a smaller elastic force that leads to lower dissipation and a higher rebound velocity. When using $\delta_{ss} = 0.017 + 5\%$ (runs 30-32), the elastic force term is activated earlier where the particle velocity is larger than the value at $\delta_{ss} = 0.017$. As a result, W_o is larger and the larger elastic-like term results in large deceleration. The combined effect of the liquid-solid interaction term and the elastic term provides more dissipation for the collision process. The results of coefficient of restitution for runs 25-28 fall within the experimental uncertainty. This kind of influence is hidden for Stokes number greater than 30 since the particle inertia is larger and the liquid has less viscous effect.

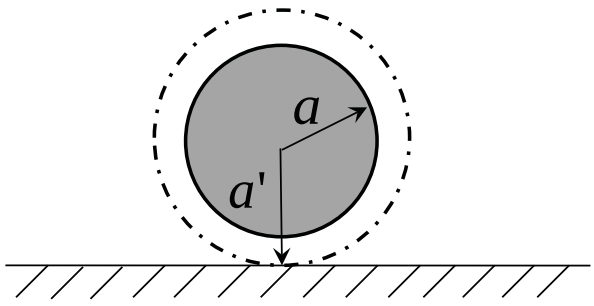

Figure 5.7: Schematic effective radius

The physical meaning of δ_{ss} can be explained by employing a concept of 'effective radius'. As

a sphere is about to collide onto a wall, the hydrodynamic pressure building up in the fluid layer between the two solid surfaces becomes large. Under the extreme pressure, the approaching solid surfaces deform elastically even before the real contact occurs (Davis *et al.* (1986)). Also, it is expected that the fluid may also compress and its density and viscosity may increases. Barnocky & Davis (1989) investigated the influence of pressure-dependent density and viscosity on the elastohydrodynamic collision of two spheres and showed that the pressure buildup during the collision process becomes sufficiently large so that the corresponding viscosity increase causes the interstitial fluid to behave nearly as a solid and to limit the close approach of the surfaces. Thus, the approaching sphere can be considered to have a virtual radius larger than the physical value. When the gap between the sphere and the target wall decreases to $\delta_{\rm ss}$, the virtual sphere with the effective radius $a' = a + \delta_{\rm ss}$ begins to reach the wall. Thus the elastic-like force starts to take effect at that moment so that the combined effect of elasticity and hydrodynamic forces resists the further approaching of the sphere. This effective radius becomes larger (increase from 0.0170 to 0.0178) for the collisions with smaller Stokes numbers (less than 30) in which the liquid is more viscous. In another word, the sphere starts to deform earlier and cannot penetrate as further as before. Similar concept was employed by Nguyen & Ladd (2002) who proposed a hydrodynamics radius for particles approaching another solid boundary to account for the lubrication layer effect; the hydrodynamics radius is $a_{hy} = a + \triangle$ and the value of $\triangle$ varies from 0 to $0.05a$ depending on the viscosity of the fluid and the particle radius a.

5.7 Coefficient of restitution

The coefficient of restitution, defined by the ratio of the rebound velocity V_r to the impact velocity V_i, $e = V_r/V_i$, is an important parameter that describes a collision in which the effects of the interstitial fluid are important. Here, the dependence of the coefficient of restitution on the Stokes number is computed from the simulation to evaluate the proposed contact model for immersed particle-wall collision process. To calculate the coefficient of restitution from the current simulations, consider the comparison between the simulated trajectory and the measured trajectory when the particle

is about to collide the wall shown in figure (5.8). Although the overall profile and the maximum height achieved in the rebound process from the simulation fit the experimental result as shown in figure (5.3), the simulated trajectory deviates from the measured trajectory during the short collision process to avoid the singularity problem arising when the two solid surfaces are too close. The deviation is the result of the proposed contact model.

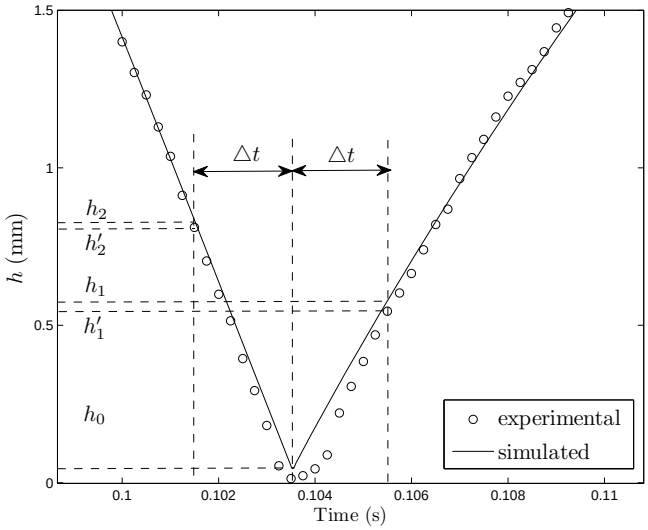

Figure 5.8: Particle trajectory when it is close to the wall

The coefficient of restitution for the simulated trajectory, denoted by e_s, is:

$$e_s = \frac{V_{rs}}{V_{is}} = \frac{(h_1 - h_0)/\triangle t}{(h_2 - h_0)/\triangle t} = \frac{h_1 - h_0}{h_2 - h_0} \tag{5.1}$$

where $\triangle t = 2$ ms; h_0, h_1, and h_2 are the gap values defined in figure (5.8) as the positions of the sphere at 2 ms after and before it reaches the lowest point h_0 in the simulation, respectively.

However, the actual coefficient of restitution for the measured trajectory is:

$$e = \frac{V_r}{V_i} = \frac{h'_1/\triangle t}{h'_2/\triangle t} = \frac{h'_1}{h'_2} \tag{5.2}$$

where h'_1 and h'_2 are the measured position of the sphere at 2 ms before and after it reaches the wall

in the experiment. The two results are different and they can be compared as:

$$\begin{aligned}\frac{e_s}{e} &= \frac{(h_1-h_0)/(h_2-h_0)}{h_1'/h_2'} = \frac{h_1-h_0}{h_1'}\frac{h_2'}{h_2-h_0} \\ &\simeq \frac{h_1h_2-h_2h_0}{h_1h_2-h_1h_0} = \frac{h_1h_2-h_1h_0+h_1h_0-h_2h_0}{h_1h_2-h_1h_0} \\ &= 1+\frac{(h_1-h_2)h_0}{(h_2-h_0)h_1}\end{aligned}$$

where an approximation is taken as $h_2' \simeq h_2$ and $h_1' \simeq h_1$ since the simulated trajectory only deviates from the experimental result when the sphere is very close to the wall. The relation between these gap values are: $h_1 \leq h_2$ since $e = h_1/h_2 \leq 1$; $h_2 > h_0$ otherwise the impact velocity is zero in the simulation. Then

$$\frac{e_s}{e} \leq 1$$

The coefficient of restitution for the simulated trajectory e_s is smaller than the experimental result e.

Thus, to compare with the current experiments and the other researcher's results, the coefficient of the restitution e is calculated as:

$$e = \frac{h_1}{h_2} \tag{5.3}$$

where h_2 and h_1 are the approximation of h_2' and h_1', respectively.

The impact Reynolds number and Stokes number is calculated based on a similar idea. The value of V_i is calculated from the simulation as:

$$V_i = \frac{h_2}{\triangle t}. \tag{5.4}$$

And correspondingly,

$$Re = \frac{DV_i}{\nu}, \tag{5.5}$$

$$St = \frac{m_pV_i}{6\pi\mu a^2} = \frac{1}{9}\frac{\rho_p}{\rho_l}Re. \tag{5.6}$$

The approximation of $h_2' \simeq h_2$ and $h_1' \simeq h_1$ might cause a slight difference between the calculated coefficient of restitution and the value measured from the experiments. To examine the difference, the results obtained by using equation (5.2) and (5.3) are compared in figure (5.9) for the first two impacts in the seven experimental cases described in Table (2.2).

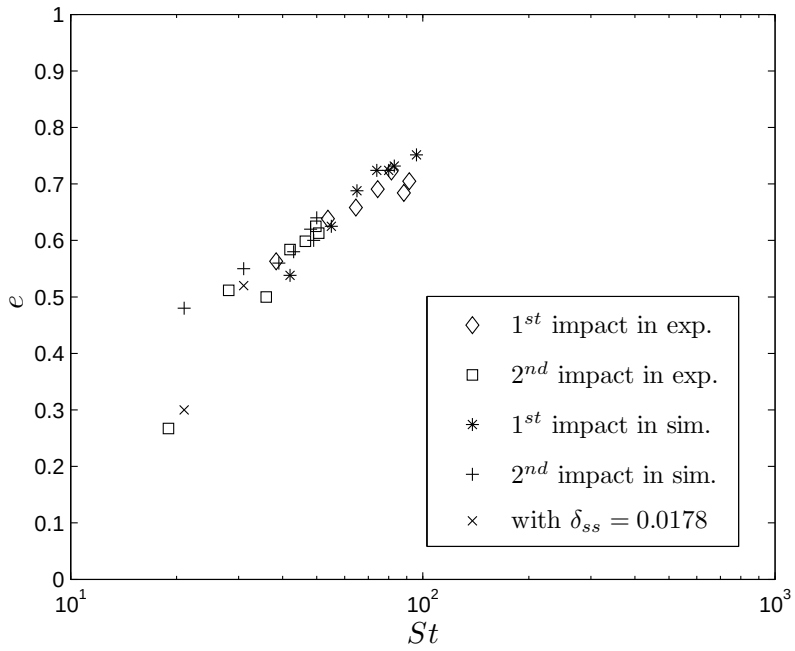

Figure 5.9: The coefficient of restitution for the first two impacts in the cases described in Table (2.2).

Figure (5.9) shows that the two sets of results are close for most of the cases with Stokes number greater than 30. The slight difference on Stokes number results from the approximation of $h_2' = h_2$ in calculating the impact velocity by using equation (5.4). The results for the second impacts of case 1 and 2 with Stokes number smaller than 30 are higher. As discussed in section (5.5), the simulated trajectory deviates from the experimental result when using $\delta_{\rm ss} = 0.017$ in the simulation for the collisions with Reynolds number less than 40 (corresponding Stokes number approximately less than 30). A larger value of $\delta_{\rm ss}$, $\delta_{\rm ss} = 0.017 + 5\%$ results in a trajectory with much lower relative error. When using the simulated trajectory with $\delta_{\rm ss} = 0.017 + 5\%$, the calculated coefficient of restitutions are closer to the experimental value as shown by the two cross points in figure (5.9). Thus, the coefficient of restitution calculated from equation (5.3) based on the simulation result can

run	ρ_l(g·cm^{-3})	μ(cP)	ρ_p(g·cm^{-3})	E(GPa)	ν	comment
1-3	1.17	15.2	7.6	200	0.33	steel sphere, 65% glycerol
4-10	1.20	50.0	7.6	200	0.33	steel sphere, 78% glycerol
11-14	1.20	50.0	11.35	16	0.44	lead sphere, 78% glycerol
15	1.20	50.0	24.0	200	0.33	artificial sphere, 78% glycerol
16	1.20	50.0	36.0	200	0.33	artificial sphere, 78% glycerol
17	1.20	50.0	48.0	200	0.33	artificial sphere, 78% glycerol
18-24	1.22	109	7.6	200	0.33	steel sphere, 85% glycerol
25-29	1.25	523	7.6	200	0.33	steel sphere, 95% glycerol
30-32	1.22	109	7.6	200	0.33	steel sphere, 85% glycerol

Table 5.1: Simulations with different input parameters and the corresponding material description. Runs with the same material properties have different initial distance; thus, the impact Stokes numbers are different. For the viscosity unit, 1 cP = 1×10^{-3} Pa·s.

be considered good approximation for the actual coefficient of restitution that represents the effect of the surrounding liquid on a collision process.

To examine the current contact model over a larger range of impact Stokes numbers and to compare with more experimental results found in the literature, simulations were run for denser particles and glycerol-water mixtures with different viscosity. The input parameters for each of the simulations are described in Table (5.1). For the runs with the same material properties, the initial distance between the sphere and the wall is set to be different so that the impact Reynolds number and Stokes number are different. In runs 15, 16 and 17, a sphere with an artificially large density is used to observe larger values of Stokes number (up to about 1000) while keeping the Reynolds number below 250 to ensure that the flow field remains axisymmetric. For runs 1 to 29, $\delta_{ss} = 0.017$ is used in the contact model. As a comparison, in runs 30, 31 and 32 that have the same initial condition and material properties as used in runs 18, 19 and 20, $\delta_{ss} = 0.017 + 5\%$ is used in the contact model, which results in different coefficient of restitution for impact Stokes number ranging from 10 to 30. The dimensionless distance δ_0, the corresponding Reynolds number Re, the Stokes number St and the coefficient of restitution e calculated from equation (5.3) based on the simulated result are listed in Table (5.2).

run	δ_0	Re_I	St_I	e	run	δ_0	Re_I	St_I	e
1	0.30	121	100	0.71	18	0.60	22	18	0.46
2	0.50	171	141	0.77	19	1.00	30	25	0.49
3	1.00	241	198	0.79	20	1.60	37	30	0.52
4	0.58	58	42	0.54	21	2.00	42	34	0.53
5	1.10	77	55	0.63	22	3.00	50	40	0.53
6	1.60	90	65	0.69	23	4.00	55	44	0.56
7	2.06	103	74	0.72	24	5.00	59	48	0.59
8	2.66	111	80	0.72	25	2.00	4.5	3.6	0.00
9	2.98	116	83	0.73	26	3.00	5.8	4.6	0.01
10	3.75	134	96	0.75	27	4.00	6.1	4.9	0.02
11	3.75	140	147	0.77	28	5.00	6.4	5.1	0.00
12	5.00	158	166	0.80	29	6.00	6.5	5.2	0.01
13	6.00	169	177	0.79	30	0.60	22	18	0.23
14	7.00	178	188	0.82	31	1.00	30	25	0.31
15	6.00	201	445	0.90	32	1.60	37	30	0.34
16	6.00	213	705	0.97	-	-	-	-	-
17	6.00	217	961	0.99	-	-	-	-	-

Table 5.2: Results of the different simulations.

The coefficient of restitution is plotted as a function of Stokes number as shown in figure (5.10). For runs 15, 16 and 17 with large Stokes number ($400 \sim 10^3$), the coefficient of restitution approaches to the dry value e_d, which indicates the liquid effect is becoming negligible and the elastic force plays the main role and makes the sphere rebound as in a dry collision process. When the Stokes number is in the range of $10 \sim 200$, the hydrodynamic forces exert more effect on the particle and the coefficient of restitution decreases as the Stokes number decreases. For runs 25-29, a higher liquid viscosity was used so that the kinetic energy of the sphere is dissipated by viscous effects from the liquid-solid interaction term. The impact velocity is small and the corresponding impact Stokes number is smaller than 10. There is no rebound and the coefficient of restitution is zero. Thus, the combined effect of the hydrodynamic force term and the elastic-like force term lead to a complete contact model for a impact Stokes number from 1 to 1000.

The relation between the coefficient of restitution calculated from the current simulations and

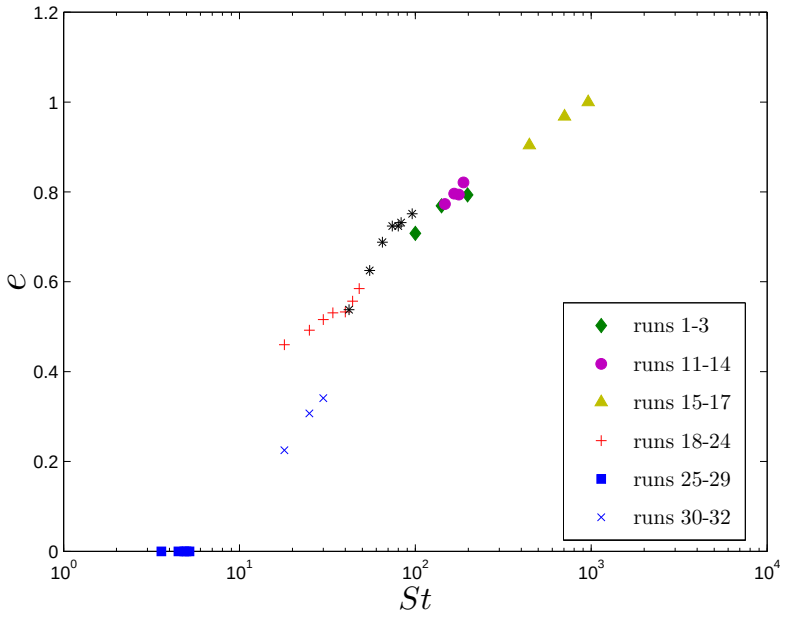

Figure 5.10: Simulation results of coefficient of restitution as a function of Stokes number.

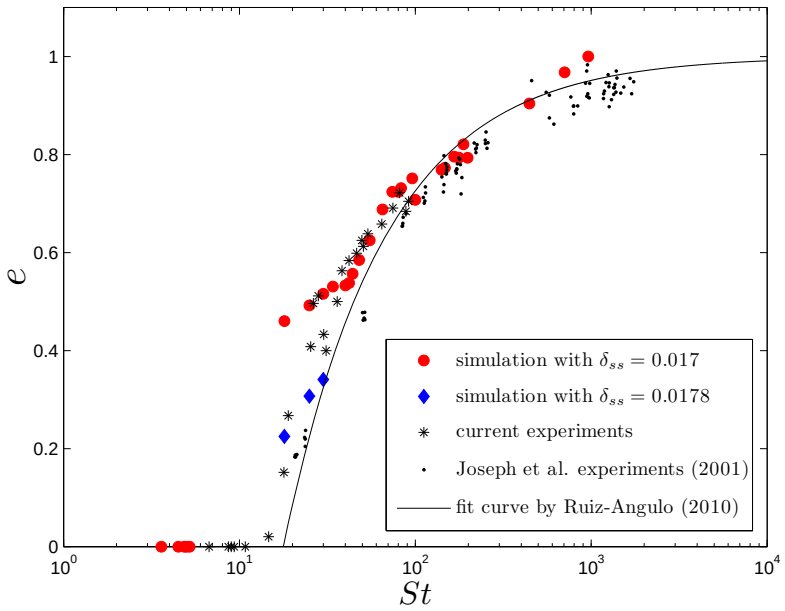

Figure 5.11: Comparison of the relations between coefficient of restitution and particle Stokes number.

the particle impact Stokes number agrees with the empirical trend, as shown in figure (5.11) that compares the simulated results with the measured results from the current experiments and Joseph et al.'s pendulum experiments [2001] for a steel sphere and Zerodur wall. For Stokes number ranging from 90 to 200, the values of the coefficient of restitution calculated from the current simulations overlap with the experimental results of Joseph *et al.* (2001) even though the whole flow field configurations are different (the sphere falls under gravity and collides with the wall vertically in the simulations while in Joseph et al.'s pendulum experiments the sphere collides with the wall horizontally). For Stokes number ranging from 30 to 90 where Joseph *et al.* (2001) has fewer experimental points, the simulated results overlap with the measured results from the current experiments. For Stokes number ranging from 10 to 30, the coefficient of restitution increases with large slope with increasing St and the experimental data are scattered within the small range of Stokes number. The results obtained from the simulations are sensitive to the non-dimensional parameter δ_{ss}. When using $\delta_{\text{ss}} = 0.017 + 5\%$ the simulations produce the coefficient of restitutions that follow the trend of a fit curve of the experiment data in Joseph *et al.* (2001) and Gondret *et al.* (2002) given by Ruiz-Angulo & Hunt (2010) as $e_{fit} = 1 - 8.65/St^{0.75}$.

In summary, the different material properties including the solid elastic property, liquid viscosity and the density ratio are incorporated appropriately in the proposed contact model. The current simulations represent the dependence of the coefficient of restitution on the impact particle Stokes number demonstrating that the contact model captures the essential physics of a particle-wall collision process in a liquid environment.

Chapter 6

Application to normal collision between two particles

The liquid effect on a particle-wall collision process has been studied by investigating the relation between the coefficient of restitution of a collision and the particle impact Stokes number. When there is another solid sphere existing in the flow field instead of the solid wall, the normal collision process between the two spheres show different particle behaviors since the influence of the target sphere on the surrounding flow field is different especially when the target sphere is not fixed in its initial position. Yang & Hunt (2006) performed particle-particle collision experiments with two spheres hanging in a glycerol-water mixture. They defined a binary Stokes number by considering the hydrodynamic effect on the two approaching spheres and found that the coefficient of restitution of a particle-particle collision has a similar dependence on the binary Stokes number to the relation between e and St found in immersed particle-wall collision process.

In the previous chapters, a normal collision process between a solid sphere and a solid wall in a liquid environment has been simulated using the fast immersed boundary method. The proposed contact model that incorporates both the liquid-solid interaction with the wall-effect correction and the solid-solid elastic force predicts the dependence of the coefficient of restitution on the particle impact Stokes number accordant with the empirical trend. A normal collision between two spheres also generates an axisymmetric flow field. The numerical method described in Chapter 3 can be used to solve for the flow field and the coupled particle dynamics as the impact sphere approaches the target. After modifying the liquid-solid interaction and the elastic force terms by considering

the effect of the target sphere, the contact model is applied to simulate a normal collision process between the two spheres. The coefficient of restitution calculated from the simulations are compared with Yang & Hunt (2006)'s experimental results. Unique particle behaviors for a particle-particle collision process at small Stokes number are represented.

6.1 Immersed particle-particle normal collision

To complement previously investigated particle-on-wall immersed collisions, Yang & Hunt (2006) investigated liquid-immersed head-on particle-particle collision processes, which provide good reference for the current simulations. This section briefly introduces the experiment setup and the definition of the coefficient of restitution and the Stokes numbers for a particle-particle collision process employed in Yang & Hunt (2006).

The normal particle-particle collision experiment performed by Yang & Hunt (2006) is shown schematically in figure (6.1). Two spheres were suspended by thin strings as two pendulums in a viscous fluid. A wide range of impact conditions were achieved by changing the release angle, the solid materials and the liquid. A typical result of the trajectories of the two particles is shown in figure (6.2).

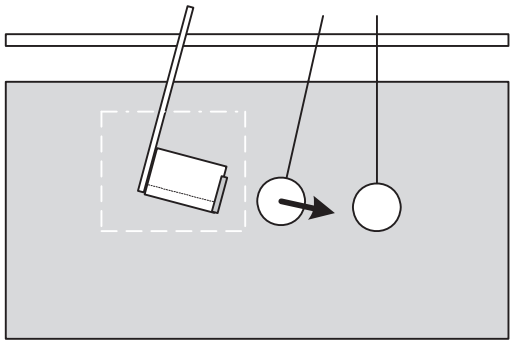

Figure 6.1: Schematic experiment setup from Yang & Hunt (2006)

The impact and rebound velocities of the two spheres, U_{i1}, U_{r1}, U_{i2} and U_{r2}, are taken as the slopes of the fit lines (in a least-squares sense) of the trajectories over a time interval from 10 to 15

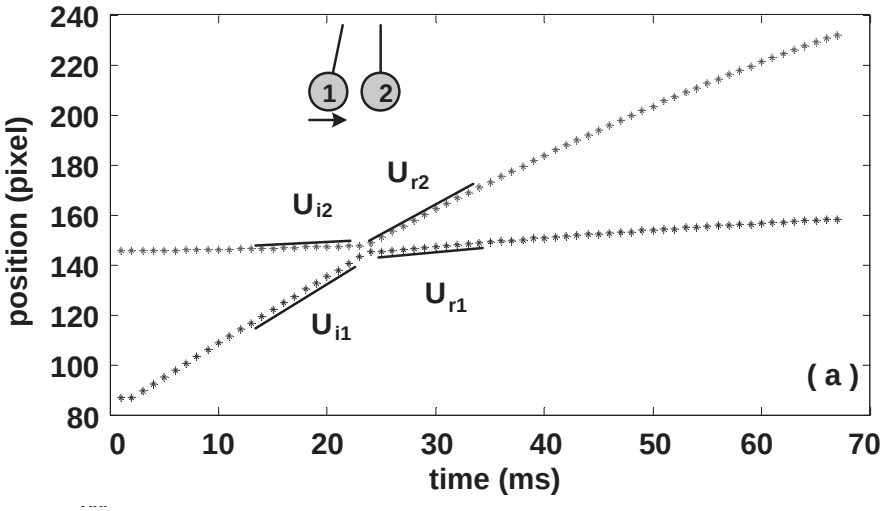

Figure 6.2: The trajectories of the two particles from Yang & Hunt (2006).

ms. The effective coefficient of restitution for such a binary collision is defined as:

$$e = -\frac{U_{r1} - U_{r2}}{U_{i1} - U_{i2}} \tag{6.1}$$

in analogy with the conventional definition for a binary dry collision.

The binary particle Stokes number for the colliding sphere was defined as:

$$St_B = \frac{m^*(U_{i1} - U_{i2})}{6\pi\mu a^{*2}} \tag{6.2}$$

in which the particle pair is characterized as a single particle with effective mass $m^* = (1/m_1 + 1/m_2)^{-1}$ and reduced radius $a^* = (1/a_1 + 1/a_2)^{-1}$ that moves at an approach velocity $U_{\rm rel} = (U_{i1} - U_{i2})$. In analogy with the single-particle Stokes number that is the ratio of the particle inertia to the liquid viscous effect, the binary Stokes number represents the ratio of the available momentum in the solid phase to the viscous dissipation calculated by multiplying an effective viscous force $6\pi\mu a^* U_{\rm rel}$ with a forcing duration $a^*/U_{\rm rel}$. When the two spheres have the same size, the binary Stokes number can be written as:

$$St_B = \frac{2}{9}\frac{\rho_p^*}{\rho_f} Re_{\rm rel} \tag{6.3}$$

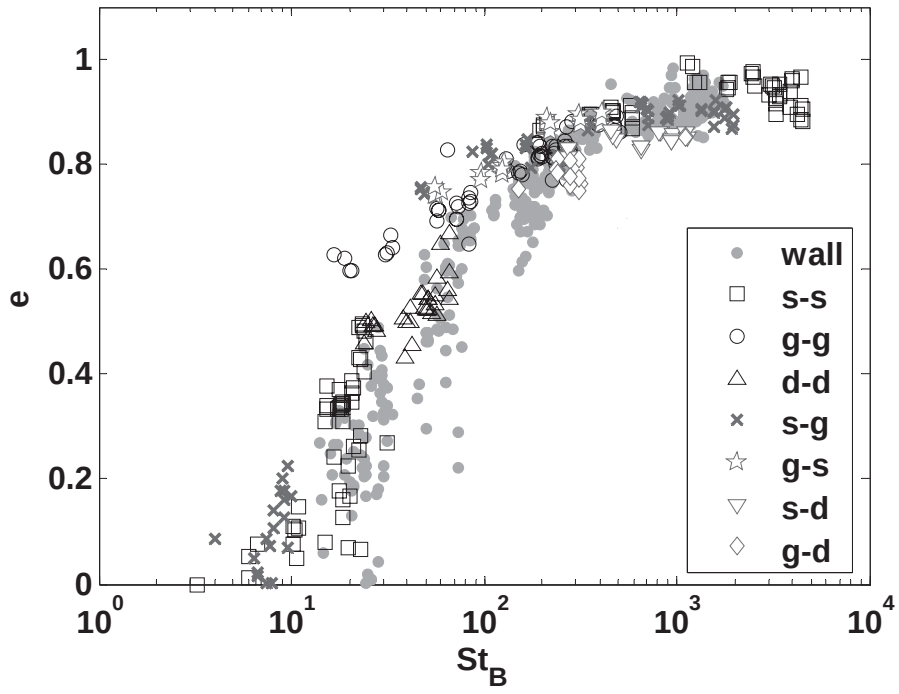

Figure 6.3: Comparison of the inter-particle and the particle-wall immersed collisions. The figure is taken from Yang (2006).

where $\rho_p^* = (1/\rho_1 + 1/\rho_2)^{-1}$ is an effective solid density and $Re_{\text{rel}} = DU_{\text{rel}}/\nu$ is the relative Reynolds number. The relation between the binary Stokes number and the relative Reynolds number is consistent with the conventional definition, $St = (\rho_p/\rho_l)Re/9$.

The functional relation between the effective coefficient of restitution and the binary Stokes number obtained from their experiments follows the empirical trend found for particle-wall collisions, as shown in figure (6.3). Collisions between different solid materials including steel, glass and delrin were marked with different indicators. Detailed discussion of this figure can be found in Yang (2006).

6.2 Modification of the contact model

To simulate a normal collision between two particles as described in the previous section with the current numerical method, the pendulum motion in the vertical direction is neglected so that the two spheres are assumed to move horizontally along the line across their centers and the surrounding flow

is axisymmetric. The assumption is appropriate since the simulation focuses on a collision process only from 30 ms before contact to 30 ms after contact. The displacement in the vertical direction during this time period is less than $0.015D$ as found from the experimental data of Yang (2006).

The sphere motion in the horizontal direction is described by the equation:

$$m_{p,m}\frac{d\tilde{V}_m}{d\tilde{t}} = \tilde{f}_{\mathrm{SL},m} + \tilde{f}_{\mathrm{SS},m} \tag{6.4}$$

where $m = 1$ and $m = 2$ stand for impact sphere and target sphere, respectively; $\tilde{f}_{\mathrm{SL},m}$ and $\tilde{f}_{\mathrm{SS},m}$ are the liquid-solid interaction and solid-solid elastic force terms proposed for the contact model in the form of equation (4.14) and equation (4.19) as:

$$\tilde{f}_{\mathrm{SL}} = H\left(\frac{\delta}{\delta_{\mathrm{SL}}}\right)\tilde{f}_{\mathrm{THR}} + [1 - H\left(\frac{\delta}{\delta_{\mathrm{SL}}}\right)]\tilde{f}_{\mathrm{SIM}}, \tag{6.5}$$

$$\tilde{f}_{\mathrm{SS}} = F\left(\frac{\delta}{\delta_{\mathrm{SS}}}\right)e_d W_o. \tag{6.6}$$

However, when the fixed target wall is replaced by a movable sphere, the hydrodynamic forces and the elastic force change correspondingly. To apply the above contact model, the analytical expressions for $\tilde{f}_{\mathrm{THR}}$ and W_o are modified to accounting for the geometry and movability effect of the target sphere.

6.2.1 Liquid-solid interaction with the target sphere effect

In a particle-particle collision process, the existence of a target spherical particle affects the liquid-solid interaction force exerted on the impact sphere. However, the influence is different from the wall effect since the surrounding fluid can pass around the target particle and the movability of the target particle further complicates the coupled evolution of the flow field. Thus, Yang's formulas for the hydrodynamic forces with a wall effect, equations (4.4), (4.8) and (4.11) in Chapter 4 are modified as:

$$\tilde{f}_{D,m} = -6\pi\mu a_m U_m \lambda(\delta^{**}, Re^*_{m,h}), \tag{6.7}$$

$$\tilde{f}_{AM,m} = -\frac{1}{2} m_{l,m}[1 + 3W(\delta^{**})]\frac{dU_m}{dt} + \frac{3}{4} m_{l,m} U_m \frac{U_{\text{rel}}}{a^*}\frac{dW(\delta^{**})}{d\delta^{**}} \tag{6.8}$$

$$\tilde{f}_{H,m} = -6\pi\mu a_m K_H(\delta^{**})^{3/2}\int_0^t \frac{dU_m}{d\tau} K(t-\tau)d\tau, \tag{6.9}$$

where the subindex $m = 1$, 2 stands for the impact sphere and the target sphere; $\delta^{**} = h/a^*$ is the gap between the two spheres non-dimensionalized by the reduced radius $a^* = (1/a_1 + 1/a_2)^{-1}$, which replaces $\delta^* = h/a$ used in the original wall correction term; $U_{\text{rel}} = U_1 - U_2$ is the relative velocity of the two spheres ; $Re^*_{m,h} = hU_{\text{rel}}/\nu$ is the gap Reynolds number. The correction terms $\lambda(\delta^{**}, Re^*_{m,h})$, $K_H(\delta^{**})$, $W(\delta^{**})$, and $dW(\delta^{**})/d\delta^{**}$ depend on δ^{**} in the same manner as given in equations (4.3), (4.12), (4.6) and (4.7). The effect of the target sphere converges to the wall correction form when the radius a_2 increases to infinitely large.

The analytical result is compared with a simulated result in which the trajectories of the particles are prescribed with an experimental result from Yang (2006). As shown in figure (6.4), the analytical and the simulated results match each other for moderate gap and deviate with diminishing gap after $\delta < 0.05D$, which is similar to the result found in a particle-wall collision. Thus the modified formulas for the hydrodynamic forces are adopted in the liquid-solid interaction term as:

$$\tilde{f}_{\text{SL},m} = H\left(\frac{\delta}{\delta_{\text{SL}}}\right)\tilde{f}_{\text{THR},m} + [1 - H\left(\frac{\delta}{\delta_{\text{SL}}}\right)]\tilde{f}_{\text{SIM},m}, \tag{6.10}$$

where $\tilde{f}_{\text{THR},m} = \tilde{f}_{D,m} + \tilde{f}_{AM,m} + \tilde{f}_{H,m}$ and $\tilde{f}_{\text{SIM},m}$ is the simulated force on the corresponding particle with indicator m. The same Heaviside function defined by equation (4.15) as shown in figure (4.9) is employed to blend the theoretical result and the simulated results in a manner similar to that described in Chapter 4. The non-dimensional parameter δ_{SL} is conservatively taken as $0.1D$.

Thus, the hydrodynamic forces exerted on the two spheres are calculated directly from the simulation when the gap between the two spheres is still large; the analytical results start to be counted as the impact sphere approaches the target and $\tilde{f}_{\text{SL},m} = \frac{1}{2}\tilde{f}_{\text{THR},m} + \frac{1}{2}\tilde{f}_{\text{SIM},m}$ at $\delta = 0.1D$; when the two sphere are about to collide, the hydrodynamic forces are taken as the values calculated from the analytical expressions.

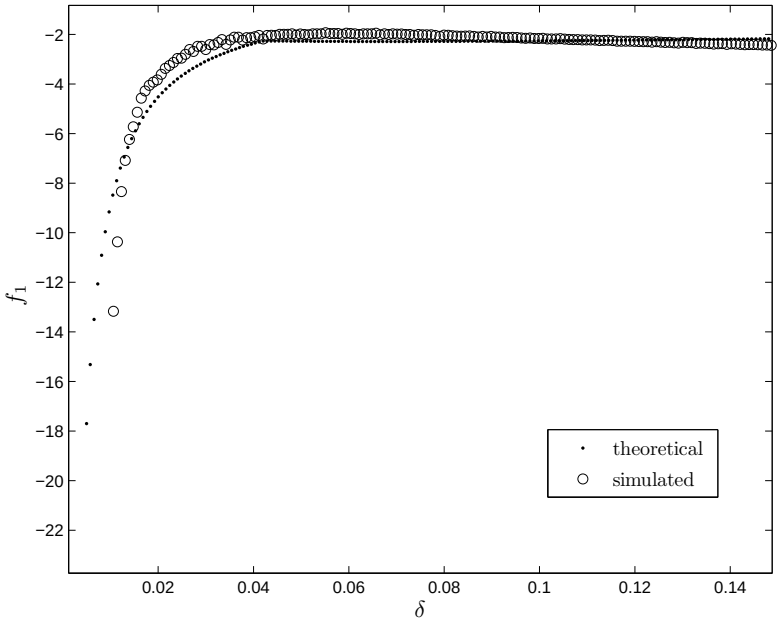

(a) hydrodynamic force on impact sphere

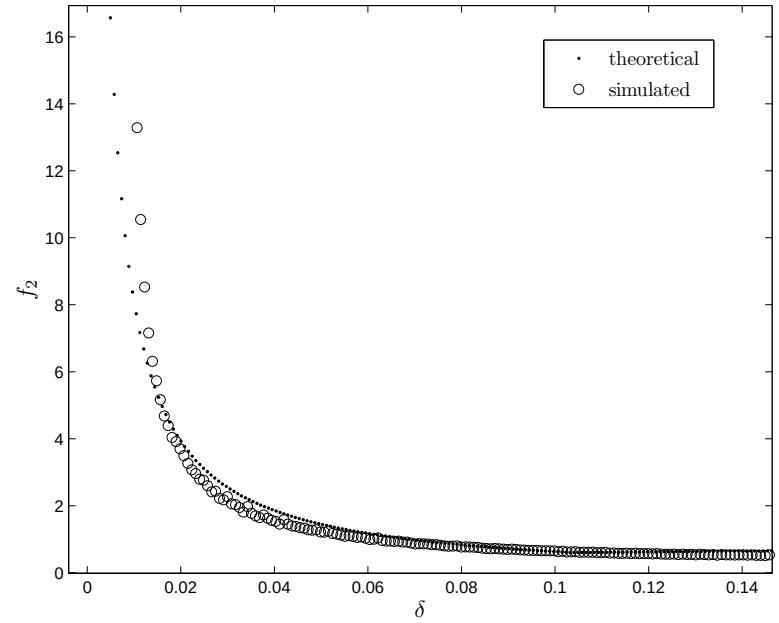

(b) hydrodynamic force on target sphere

Figure 6.4: Comparison between the analytical and simulated results for the hydrodynamic force in a particle-particle collision

6.2.2 Elastic effect between two spheres

To modify the elastic force W_o in the solid-solid interaction term (equation 4.19), the Hertz elastic contact theory is considered for a normal contact between two elastic spheres as shown in figure (6.5). The pressure distribution on the contact area is:

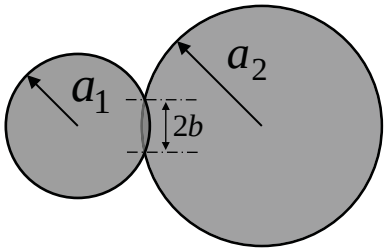

Figure 6.5: Schematic of a contact between two elastic spheres

$$P = P_o(1 - \frac{r^2}{b^2})^{1/2} \tag{6.11}$$

with $P_o = \frac{2}{\pi}E^* \left(\frac{\varepsilon}{a^*}\right)^{1/2}$, where $b = \sqrt{a^*\varepsilon}$ is the radius of contact area, a^* is the reduced radius and ε is the indent depth. The impact force can be calculated by integrating the pressure over the contact area:

$$W = \int_0^b P_o(1 - \frac{r^2}{b^2})^{1/2} 2\pi r dr = \frac{4}{3}E^* b^2 \left(\frac{\varepsilon}{a^*}\right)^{1/2} = \frac{4}{3}E^* \sqrt{a^*}\varepsilon^{3/2}. \tag{6.12}$$

This result is the same as the impact force for a elastic sphere contacting with a solid wall given in equation (4.16) except that the radius of the sphere a in (4.16) is replaced by the reduced radius a^*. Thus, the maximum elastic force between the two spheres is solved using the same approach as discussed in Chapter 4:

$$W_{o2p} = \frac{4}{3}E^* \left(\frac{15m^* U_{\text{rel}}^2}{16E^* a^{*3}}\right)^{3/5} \tag{6.13}$$

where the reduced mass, m^*, reduced modulus E^* and reduced radius a^* are used together with the relative velocity U_{rel}.

The solid-solid interaction term in the contact model for a particle-particle collision is modified

to the form:

$$\tilde{f}_{\mathrm{ss}} = F\left(\frac{\delta}{\delta_{\mathrm{ss}}}\right) e_d W_{o2p} \tag{6.14}$$

where, the function $F\left(\frac{\delta}{\delta_{\mathrm{ss}}}\right)$ is defined the same as equation (4.20) in particle-wall collision model as shown in figure (4.11).

Thus, when the gap between the two spheres is greater than δ_{ss}, the elastic interaction between the two spheres is irrelevant; when the gap decreases below the threshold value, δ_{ss}, an elastic-like force increases from zero exponentially to the dry collision value for $\delta = 0$. The non-dimensional parameter δ_{ss} is determined in the following section.

6.3 Simulation and results

With the above contact model, the normal collision process between two sphere with different binary Stokes numbers are simulated. The resulting trajectories of the impact and rebound particles are compared with the experimental data of Yang & Hunt (2006) so that the non-dimensional parameter δ_{ss} is calibrated by choosing the value that presents the best fit to the experimental trajectory. The effective coefficient of restitution calculated from the simulations with different solid materials and different initial conditions is compared with the experimental results. The special dynamic behaviors of the two particles in a collision process with small binary Stokes number are obtained accordant with the observation in the experiments.

6.3.1 Simulation setup

Yang & Hunt (2006) measured the trajectories of the impact and target particles in their immersed head-on collision experiments. For an example, the result of a collision event named 'gg3462' from Yang & Hunt (2006) is plotted in figure (6.6).

To compare a simulation for a normal particle-particle collision to the experimental results, the simulation is set up as follows. Three-level multi-grid computation domains are employed with the two particles with identical radius placed along the axis of symmetry. The first-level domain is

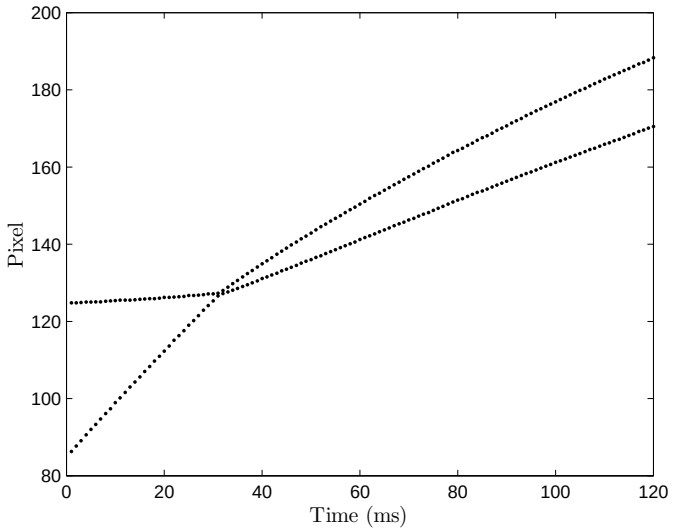

Figure 6.6: The trajectories of the impact and target spheres from Yang & Hunt (2006).

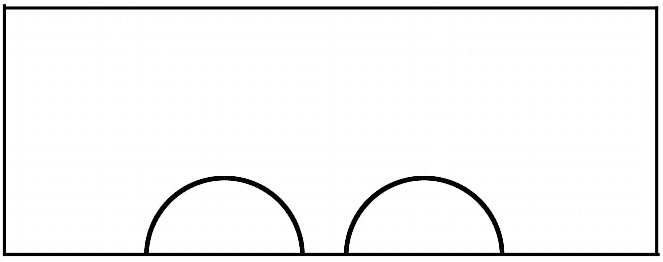

Figure 6.7: First level computation domain for a particle-particle collision.

shown in figure (6.7). According to the available experimental data, the impact sphere starts from an initial velocity, V_{Io}; the target sphere has a zero initial velocity. The motion equation of the two spheres is:

$$m_{p,m}\frac{d\tilde{V}_m}{d\tilde{t}} = \tilde{f}_{\text{SL},m} + \tilde{f}_{\text{SS},m} \tag{6.15}$$

where m = 1,2, $\tilde{f}_{\text{SL},m}$ and $\tilde{f}_{\text{SS},m}$ are given in equation (6.10) and (6.14) as the modified contact model described in the previous section. The equation is non-dimensionalized with $L_o = D$, the diameter of the spheres, and $t_o = D/V_{Io}$ as:

$$\tau_m\frac{dV_m}{dt} = f_{\text{SL},m} + f_{\text{SS},m}. \tag{6.16}$$

where $\tau_m = \rho_{p.m}/\rho_l$ is the density ratio. The Navier-Stokes equations for the flow field non-dimensionalized with $L_o = D$ and $t_o = D/V_{Io}$ have a non-dimensional parameter, $Re = V_{Io}D/\nu$, that is determined by the initial condition and the material properties given in the experimental data. For the case given in figure (6.6), the two spheres are both glass spheres and the diameter of the spheres is 12.7 mm corresponding to 148 pixel in the image. The liquid properties are given as $\mu = 0.004$ Pa·s and $\rho_l = 1112$ kg/m^3. The initial velocity is 0.110 m/s. Thus, the input Reynolds number for the simulation is $Re = 249$. The elastic properties of the spheres can be found in Yang (2006). The dimensionless time step in the simulation is 0.001 and the CFL number is less than 0.5 for every time step.

The trajectories calculated from the simulation vary with different δ_{SS}. For the three values of δ_{SS} used in the simulations, $\delta_{\text{SS}} = 0.017$, 0.024 and 0.030, a larger value of δ_{SS} produces a smaller relative velocity between the impact and target spheres after collisions. After comparing with the experimental results, this dimensionless parameter is calibrated as $\delta_{\text{SS}} = 0.024$, which produces the best fit as shown in figure (6.8). Compared with $\delta_{\text{SS}} = 0.017$ for a particle-wall immersed collision process, the threshold value δ_{SS} for a inter-particle collision process is larger. That can be explained by the fact that the minimum distance achieved during a particle-particle collision process is larger than the value for a particle-wall collision because of the geometry difference and the movability of

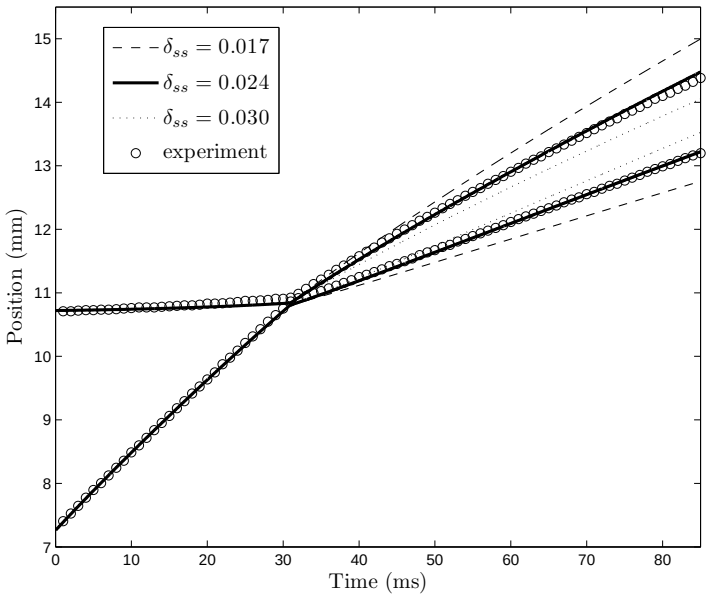

Figure 6.8: Trajectories from the simulations and the experiment

the target.

6.3.2 Unique behaviors of two spheres colliding in a liquid

Yang & Hunt (2006) observed unique behaviors of the two colliding spheres in a liquid environment when the binary Stokes number is small. The target sphere moves prior to contact when St_B ranges from $2 \sim 10$ since the pressure front building up in the interstitial liquid layer transmits the momentum of the impact sphere to the target sphere. After contact, the two spheres stick together and move with identical velocity, which Yang and Hunt called 'group velocity', U_G. Such a pre-collision target motion does not occur in a dry collision process in which the surrounding medium effect is negligible.

The current simulation can represent the pre-collision target motion and the after-collision group motion as shown in figure (6.9). Two simulations are run to compare the different liquid effect as the liquid viscosity changes. The two glass spheres are placed at the same initial positions with $0.2D$ distance between each other in the two cases and the impact sphere has the same initial velocity. In figure 6.9(a), the liquid viscosity is $\mu = 0.089$ Pa·s and the impact particle Reynolds number is

12. The target sphere has a slight displacement before the impact sphere reaches it. After contact, the two spheres move with a group velocity $U_G = 18$ mm/s. When increasing the liquid viscosity to $\mu = 0.480$ Pa·s, the velocity of the target sphere increases as the impact sphere approaches. The momentum of the impact sphere is transmitted to the target by the interstitial liquid. Finally, the two spheres move at a group velocity $U_G = 4.5$ mm/s even there is no contact and the distance between the two spheres stays at $0.07D$. The binary Stokes number for the two cases are $St_B = 10$ for figure 6.9(a) and $St_B = 0$ for 6.9(b). The coefficient of restitution for these two cases are both zero although the spheres are still moving after collision.

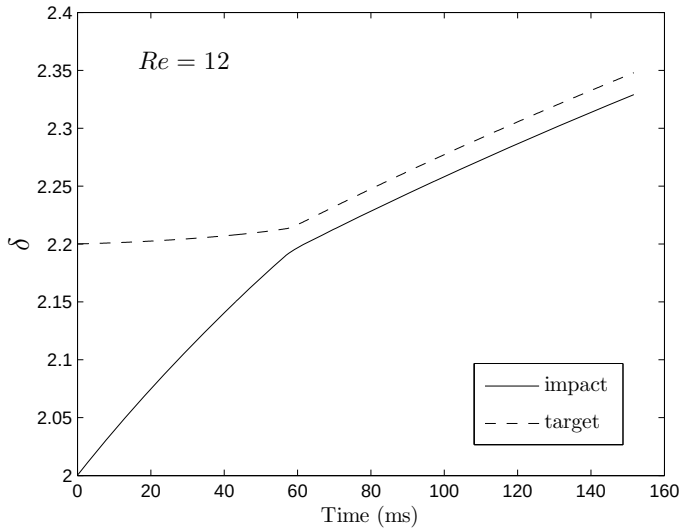

(a)

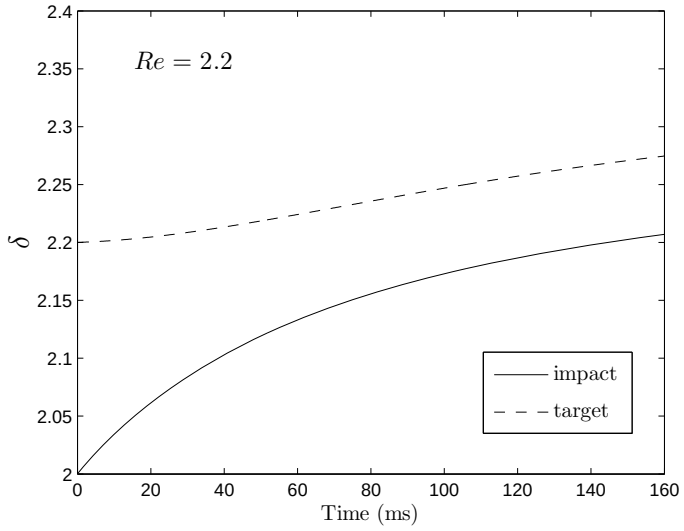

(b)

Figure 6.9: Group motion of the two spheres after contact. The solid line and dashed line represent the trajectories of the impact and target spheres, respectively.

6.3.3 The effective coefficient of restitution

Simulations with different material properties and initial conditions are run to obtain normal head-on collisions with a wide range of binary Stokes numbers. The limitation of the numerical method restricts the particle Reynolds number to be less than 300 to obtain an axisymmetric flow filed. The effective coefficient of restitution is obtained based on the slopes of the trajectories as

$$e = -\frac{U_{r1} - U_{r2}}{U_{i1} - U_{i2}}$$

where the slopes are obtained as shown in figure (6.2) with time interval 10 ms. The binary Stokes number is calculated as the definition in equation (6.2) as:

$$St_B = \frac{m^*(U_{i1} - U_{i2})}{6\pi\mu a^{*2}} = \frac{2}{9}\frac{\rho_p^*}{\rho_f} Re_{\text{rel}}$$

where

$$Re_{\text{rel}} = \frac{\rho_l D U_{\text{rel}}}{\mu}$$

with the relative velocity $U_{\text{rel}} = U_{i,1} - U_{i,2}$ determining the difference between the slopes of the two impact trajectories. The input parameters for the simulation and the results of e and St_B are listed in Table (6.1). Steel and glass spheres are used as impact or target sphere in the different runs so that the reduced density $\rho_p^* = (1/\rho_1 + 1/\rho_2)^{-1}$ has different value as the result of the combination of different materials.

run	μ(cP)	ρ_l(g·cm^{-3})	ρ_p^*(g·cm^{-3})	V_{Io}(cm·s^{-1})	Re_{Io}	St_B	e	comment
1	4.1	1.11	7.78	8.4	264	197	0.87	steel-steel
2	4.1	1.11	3.83	9.6	294	104	0.75	steel-glass
3	4.1	1.11	2.54	8.0	249	59	0.68	glass-glass
4	43.0	1.20	7.78	11.3	33	22	0.33	steel-steel
5	43.0	1.20	3.83	8.7	26	7.5	0.00	steel-glass
6	43.0	1.20	2.54	7.0	22	2	0.00	glass-glass

Table 6.1: Simulations for head-on collision between two spheres.

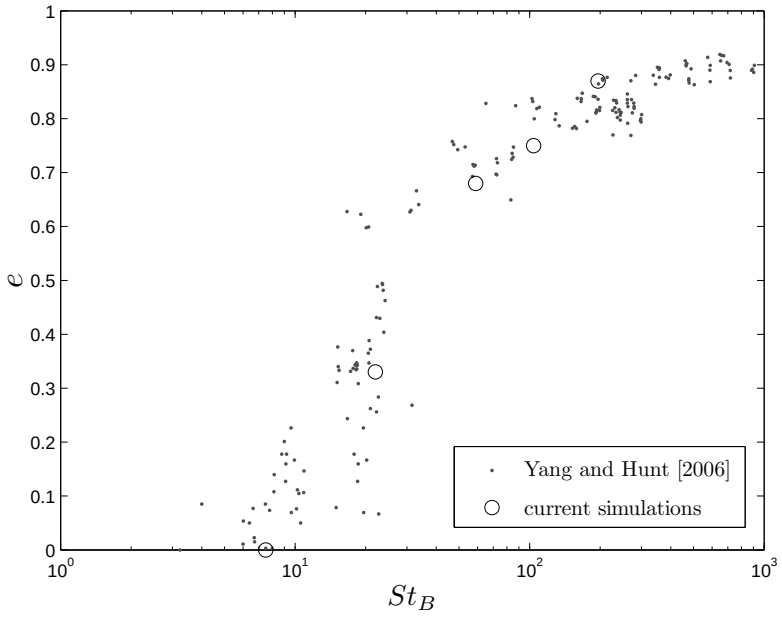

Figure 6.10: Coefficient of restitution as a function of binary Stokes number

The calculated coefficient of restitution is presented as a function of the binary Stokes number and compared with the experimental data of Yang & Hunt (2006), as shown in figure (6.10). For binary Stokes numbers ranging from 50∼200, the effective coefficient of restitution varies from 0.68 to 0.87 within the range of the experimental results. At $St_B = 22$, the coefficient of restitution is $e = 0.33$ much less than the computations for larger St_B. When the binary Stokes number is less than 10, the relative velocity between the target and impact spheres is zero so that the effective coefficient of restitution is zero. The dependence of e on St_B is consistent with the empirical trend. The experimental data scatter over a wide rang for $5 < St_B < 30$, which was explained in Yang & Hunt (2006) as a sphere impacting at lower Stokes numbers is sensitive to the sphere surface roughness, the roundness and the disturbances in the ambient flow yielding a larger error bar. The uncertainty of experiments in calculating velocity leads to errors in calculating e and St and for low Stokes numbers, e increases with large slope with increasing St so that even small error makes the data scatter in a wide range. The current simulation results provide a good estimation for the effective coefficient of restitution for immersed collisions within this lower binary Stokes number range.

Thus, it is concluded that the modified contact model appropriately incorporates the geometry

and movability effect of the target sphere so that it captures the essential contact mechanism for particle-particle collisions in a viscous liquid environment.

Chapter 7

Conclusions

7.1 Summary

The process of a solid sphere normally colliding with a solid wall in an liquid environment is investigated through experiments and numerical simulations in the current study. The goal of this study is to develop an accurate and robust collision model that can be used in future simulations of liquid-solid flows.

Experiments of a sphere moving under gravity and colliding with a bottom wall in a mixture of glycerol and water are performed using an electronic-magnetic release system to drop a steel sphere from zero velocity without rotation. The fall and rebound of the sphere is recorded by a high speed videography system and the trajectory of the sphere is obtained from the video using an image process technique.

A higher frame rate for the recording camera is employed in the experiments so that sufficient position points are obtained especially when the sphere is about to collide with the wall. A velocity decrease prior to contact is observed by fitting the position points with a high order polynomial. This observation confirms that the velocity decrease prior to contact found in the pendulum-wall collision experiments performed by Joseph *et al.* (2001) also exits when a sphere falls under gravity to a wall. The existence of the wall influences the hydrodynamic forces that are exerted on the sphere; these forces exceed the gravitational force with diminishing gap between the sphere and the

wall, which results in a deceleration on the sphere before it collides with the wall.

The effect of the viscous liquid on the motion of the particle during a collision process is further investigated by calculating the coefficient of restitution of the collisions. The coefficient of restitution, e, defined as the ratio of the rebound to impact velocity, provides a measure of the energy dissipated during a collision process. When presented as a function of impact Stokes number, St, the obtained coefficient of restitution shows a monotonic decrease as the Stokes number decreases, indicating an increase in dissipation of the particle kinetic energy with greater viscous effect. At a critical Stokes number, all the kinetic energy is dissipated and there is no rebound; correspondingly, the coefficient of restitution is zero. A dependence between e and St has been reported in the previous literature. The current experiments confirms the dependence by presenting more data for Stokes numbers ranging from 5 to 100 in which the coefficient of restitution changes remarkably with varying Stokes numbers.

The complexity of the flow field around the sphere affects the nature of the rebound. An accurate description of the evolution of the surrounding flow field facilitates the understanding of an immersed particle collision process.

A fast immersed boundary projection method is modified and applied in cylindrical coordinates to solve the incompressible Navier-Stokes equations for an axisymmetric flow. The hydrodynamic force exerted on a sphere moving in the liquid can be calculated from the simulation. After coupling with the equation of motion of the sphere, both the evolution of the flow field and the sphere dynamics can be simulated accurately and with high efficiency.

A contact model is proposed to simulate the normal collision between a solid sphere and a wall in a liquid environment. Based on the analytical formulas reported in the literature that evaluate the effect of the presence of the wall on the Stokes drag force, the added mass and the history force, the contact model computes the hydrodynamic forces on the particle when it is too close to the wall as an amendment for the hydrodynamic force calculated from the simulation. The model also includes an elastic force to account for the elastic deformation of the solids, which stores some of the impact energy of the particle and allows the particle to rebound. By including this contact model,

the process of a particle settling and rebounding from a wall in a viscous liquid is simulated. The calculated rebound motion is examined with the measured trajectory from the current experiments; this comparison is used to calibrate an important dimensionless parameter, δ_{ss}, for the contact model.

The numerical simulation captures the trajectory of the sphere with multiple bounces and facilitates the calculation of the vorticity dynamics associated with the particle moving downwards and upwards, which has not been investigated in prior studies. Moreover, the velocity decrease before contact, observed in the experiments, is reproduced in the simulation. The hydrodynamic forces on the sphere calculated from the contact model increases dramatically with diminishing gap between the sphere and the wall. The sphere starts to decelerate as the result of the presence of the wall before it collides with the wall.

When applied to a wider range of impact Stokes number, the coefficient of restitution calculated from the simulation increases as a function of the Stokes number, and shows good agreement with the experimental results found both in the current experiments and by other researchers. Thus, it is concluded that the contact model appropriately incorporates the different material properties including the solid elasticity, the liquid viscosity and the density ratio so that the simulation truly describes the normal immersed collision between a particle and a wall with different particle impact Stokes number as long as the surrounding flow field remains axisymmetric.

A head-on particle-particle collision happening in a liquid environment is simulated by employing a modified contact model. The geometry and movability of the target sphere are taken into account in the contact model by (i) replacing the gap between the impact sphere and a wall non-dimensionalized with the diameter of the sphere by the gap between the impact and target spheres non-dimensionalized with the reduced diameter of the two spheres; (ii) using the relative velocity between the two sphere instead of the velocity of the impact sphere; (iii) using a larger value of δ_{ss} as calibrated with the experimental results.

The numerical simulations of a particle-particle collision produce the unique behaviors of the two colliding spheres including the pre-contact target motion and after-contact group motion that were

observed in other researchers' experiments. The effect of the surrounding liquid on these behaviors is investigated by using different values of the liquid viscosity in the simulations. It is found that a higher value of the viscosity keeps the impact sphere from contacting the target sphere and leads to a smaller group motion velocity as a result of viscous dissipation.

The effective coefficient of restitution of a particle-particle collision predicted by the simulations compares favorably with the results reported by other researchers. When correlated with the binary Stokes number, St_B, the effective coefficient of restitution shows a monotonic decrease with diminishing St_B that is analogous to the results of particle-wall collisions.

In summary, according to both the current experiments and the numerical simulations, the incompressible viscous liquid is found to play an important role in a collision process. In a particle-wall collision, the velocity of the impact sphere decreases as the result of the remarkably increasing hydrodynamic force as the sphere approaches the wall. In a particle-particle collision, the target sphere moves prior to contact as the result of the hydrodynamic force from the surrounding liquid so that the relative velocity between the two sphere decreases as the impact sphere approaches the target. When the liquid is very viscous, the two spheres finally move at identical velocity with a constant distance between them so that the relative velocity is zero and there is no contact between the two spheres. This group motion without contact is analogous to the case in which a sphere settling to a solid wall decelerates and rests on the wall. The liquid effect on a collision process is quantitatively investigated by correlating the coefficient of restitution with the impact Stokes number. Both the experimental and simulated results show a strong dependence of the coefficient of restitution on the Stokes number. A large liquid viscosity dissipates more kinetic energy of the colliding system and results in a lower rebound. The decrease of the coefficient of restitution is more pronounced for the Stokes numbers lower than 100. The similar trends found in the particle-wall and particle-particle collisions indicates that the contact mechanisms for the two kinds of collision are similar.

The good agreement between the simulated and experimental results demonstrates the proposed contact model reproduces the particle dynamic behaviors during a particle-wall collision process. It

is concluded that the contact model appropriately incorporates the contact mechanism in a numerical simulation without solving the thin lubrication layer and the elastic deformation of the solid parts. Moreover, a modified contact model using reduced material properties, the relative velocity for the solid phase and a larger dimensionless parameter, δ_{ss}, reproduces the unique behaviors during inter-particle collision processes and the functional relation between the effective coefficient of restitution and the binary Stokes number. Thus, the proposed contact model can be generally applied to different collision processes after incorporating the geometry and movability effect of the target and calibrating the parameter δ_{ss}, which is considered as the additional part of an effective diameter for the impact sphere.

7.2 Future work

There are several directions for the further application of the numerical method and the proposed contact model.

The values adapted for the parameter, δ_{ss}, in the contact model for different kinds of collision are different. To find the dependence of δ_{ss} on the geometry and movability of the target by employing spheres with different sizes and densities could be enlightening for further revealing the contact mechanism for different immersed collisions processes.

The Navier-Stokes equations solved in the current numerical simulations include only the mass and momentum equations. The equation of energy conservation can be added in the system to account for the heat transfer problem related to a collision process. Using the simulation, the motion of the fluid could be input to the energy equation to investigate the effect of the impinging wake on the transport from a heated surface. Similarly the simulation could be used to investigate erosion caused by a particle impacting on erodible bed.

The current numerical simulation is limited to solve only an axisymmetric flow problem. A three-dimensional code could be developed to simulate oblique collision and impacts at higher Reynolds number. The contact model is expected to be able to describe the collisions with three dimensional flow effect. If it is the case, then a flow with more particles in the liquid can be simulated and

the macroscopic properties, such as the effective viscosity, of the mixture can be obtained from the simulation.

Bibliography

Al-Samieh, M. F. & Rahnejat, H. 2002 Physics of lubricated impact of a sphere on a plate in a narrow continuum to gaps of molecular dimensions. *J. Phys. D: Appl. Phys.* **35**, 2311–2326.

Ardekani, A. M. & Rangel, R. H. 2008 Numerical investigation of particle-particle and particle-wall collisions in a viscous fluid. *J. Fluid Mech.* **576**, 437–466.

Bagchi, P. & Balachandar, S. 2003 Inertial and viscous forces on a rigid sphere in a straining flow at moderate reynolds numbers. *J. Fluid Mech.* **481**, 105–148.

Barnocky, G. & Davis, R. H. 1988 Elastohydrodynamic collision and rebound of spheres: experimental verification. *Phys. Fluids* **31** (6), 1324–1329.

Barnocky, G. & Davis, R. H. 1989 The influence of pressure-dependent density and viscosity on the elastohydrodynamic collision and rebound of two spheres. *J. Fluid Mech.* **209**, 501–519.

Basset, A. 1888 A treatise on hydrodynamics. *Deighton Bell* **2**.

Beyer, R.P. & LeVeque, R.J. 1992 Analysis of a one-dimensional model for the immersed boundary method. *SIAM J. Numer. Anal.* **29** (2), 332–364.

Boussinesq, J. 1885 Sur la rsistance qu'oppose un fluide indfini au repos, sans pesanteur, au mouvement vari d'une sphre solide qu'il mouille sur toute sa surface, quand les vitesses restent bien continues et assez faibles pour que leurs carrs et produits soient ngligeables. *C. R. Acad. Sci. Paris* (100), 935.

Brenner, H. 1961 The slow motion of a sphere through a viscous fluid towards a plane surface. *Chem. Eng. Sci* **16**, 242–251.

Chang, W., Giraldo, F. & Perot, B. 2002 Analysis of an exact fractional step method. *J. Comput. Phys.* **180**, 183–199.

Chaplin, J. R. 1999 History forces and the unsteady wake of a cylinder. *J. Fluid Mech* **393**, 99–121.

Clift, R., Grace, J. R. & Weber, M. E. 1978 *Bubbles, Drops and Particles*. Academic Press.

Coimbra, C. F. M., L'Esperance, D., Lambert, R. A., Trolinger, J. D. & Rangel, R. H. 2004 An experimental study on stationary history effectes in high frequency stokes flows. *J. Fluid Mech.* **504**, 353–363.

Colonius, T. & Taira, K. 2008 A fast immersed boundary method using a nullspace approach and multi-domain far-field conditions. *Comput. Methods Appl. Mech. Engrg.* **197**, 2131–2146.

Cox, R. & Brenner, H. 1967 The slow motion of a sphere through a viscous fluid towards a plane surface ii: Small gap widths, including inertial effects. *Chem. Eng. Sci* **22**, 1753–1777.

Crowe, C., Sommerfeld, M. & Tsuji, Y. 1998*a* *Multiphase flows with droplets and particles*. CRC Press.

Crowe, C., Sommerfeld, M. & Tsuji, Y. 1998*b* *Multiphase flows with droplets and particles*. Florida: CRC Press.

Davis, R. H., Serayssol, J. & Hinch, E. J. 1986 The elastohydrodynamic collision of two spheres. *J. Fluid Mech.* **163**, 479–497.

Glowinski, R., Pan, T.W. & Periaux, J. 1998 Distributed lagrange multiplier methods for incompressible viscous flow around moving rigid bodies. *Comput. Method Appl. Mech. Engrg.* **151**, 181–194.

Gondret, P., Lance, E. Hallouinand M. & Petit, L. 1999 Experiments on the motion of a solid sphere toward a wall: From viscous dissipation to elastohydrodynamic bouncing. *Physics of Fluids* **11** (9), 2803–2805.

Gondret, P., Lance, M. & Petit, L. 2002 Bouncing motion of spherical particles in fluids. *Physics of Fluids* **14** (2), 643–652.

Hertz, H. 1882 Ueber die beruhrung fester elastischer korper (on the contact of elastic solids). *Journal reine und angewandte Mathematik* p. 156.

Hinch, E. J. 1993 The approach to steady state in oseen flows. *J. Fluid Mech* **256**, 601–604.

Johnson, K. L. 1985 *Contact Mechanisc*. Cambridge University Press.

Johnson, T. A. & Patel, V. C. 1999 Flow past a sphere up to a reynolds number of 300. *J. Fluid Mech.* **378**, 19–70.

Joseph, G. 2003 Collisional dynamics of macroscopic particles in a viscous fluid. PhD thesis, California Institute of Technology.

Joseph, G. G. & Hunt, M. L. 2004 Oblique particle-wall collisions in a liquid. *J. Fluid Mech.* **510**, 71–93.

Joseph, G. G., Zenit, R., Hunt, M. L. & Rosenwinkel, A. M. 2001 Particle-wall collisions in a viscous fluid. *J. Fluid Mech.* **443**, 329–346.

Kim, I., Elghobashi, S. & Sirignano, W. A. 1998 On the equation for sphericalparticle motion: effect of reynolds and acceleration numbers. *J. Fluid Mech* **367**, 221–253.

Lai, M. & Peskin, C.S. 2000 An immersed boundary method with formal second-order accuracy and reduced numerical viscosity. *J. Comput. Phys.* **160**, 705–719.

Lawrence, C. J. & Mei, R. W. 1995 Long-term behaviour of the drag on a body in inpulsive motion. *J. Fluid Mech* **283**, 2307–2327.

Leweke, T., Thompson, M. C. & Hourigan, K. 2004 Vortex dynamics associated with the collision of a sphere with a wall. *Physics of Fluids* **16** (9).

Lian, G., Adams, M. J. & Thornton, C. 1996 Elatohydrodynamic collision of solid spheres. *J. Fluid Mech.* **311**, 141–152.

Lorenzini, G. & Mazza, N. 2004 *Debris Flow Phenomenology and Rheological Modelling*. WIT Press.

Lovalenti, P. M. & Brady, J. F. 1993 The hydrodynamic force on a rigid particle undergoing arbitrary time-dependent motion at small reynolds numbers. *J. Fluid Mech* **256**, 561–605.

Lundberg, J. & Shen, H. H. 1992 Collisional restitution dependence on viscosity. *J. Eng. Mech.* **118**, 979.

McLaughlin, M. H. 1968 An experimental study of particlecwall collision relating to flow of solid particles in a fluid. Engineer's degree thesis, California Institute of Technology.

Mei, R. & Adrian, R. J. 1992 Flow past a sphere with an oscillation in the free-stream velocity and unsteady drag at finite reynolds number. *J. Fluid Mech.* **237**, 323–341.

Michaelide, E. E. 1997 Reviewcthe transient equation of motion for particles, bubbles, and droplets. *Trans, ASME: J. Fluids Eng* **119**, 223–247.

Milne-Thomson, L. M. 1968 *Theoretical hydrodynamics*, 5th edn. New York: Dover Publications.

Mittal, R. & Iaccarino, G. 2005 Immersed boundary methods. *Annu. Rev. Fluid Mech.* **37**, 239–261.

Nguyen, N.-Q. & Ladd, A.J.C. 2002 Lubrication corrections for lattice-boltzmann simulations of particle suspensions. *Physical Review E* **66** (046708).

Peskin, C. S. 1972 Flow patterns around heart valves: a numerical method. *J. Comput. Phys.* **10**, 252–271.

Roma, A. M., Peskin, C. S. & Berger, M. J. 1999 An adaptive version of the immersed boundary method. *J. Comput. Phys.* **153**, 509–534.

Ruiz-Angulo, A. & Hunt, M. L. 2010 Measurements of the coefficient of restitution for particle collisions with ductile surfaces in a liquid. *Granular Matter* In press.

Stokes, G.G. 1851 On the effect of the internal friction of fluids on the motion of pendulums. *Transactions of the Cambridge Philosophical Society* **9** (8).

Stokes, G. G. 1880 *Collected Mathematical and Physical papers*. Cambridge University Press.

Taira, K. 2008 The immersed boundary projection method and its application to simulation and control of flows around low-aspect-ratio wings. PhD thesis, California Institute of Technology.

Taira, K. & Colonius, T. 2007 The immersed boundary method: A projection approach. *J. Comput. Phys.* **225**, 2118–2137.

TenCate, A., Nieuwstad, C. H., Derksen, J. J. & Akker, H. E. A. Van Den 2002 Paticle imaging velocimetry experiments and lattice-boltzmann simulations on a single sphere settling under gravity. *Physics of Fluids* **14** (11).

Thompson, M. C., Leweke, T. & Hourigan, K. 2007 Sphere-wall collisions: vortex dynamics and stability. *J. Fluid Mech.* **575**, 121–148.

Wells, J.C. 1993 Mathematical modelling of normal collison of smooth elastic sphere in liquid. *Powders and Grains* pp. 45–50.

Yang, F.-L. 2006 Interaction law for a collision between two solid particles in a viscous liquid. PhD thesis, California Institute of Technology.

Yang, F.-L. & Hunt, M. L. 2006 Dynamics of particle-particle collisions in a viscous liquid. *Physics of Fluids* **18** (121506).

Zenit, R. & Hunt, M. L. 1999 Mechanics of immersed particle collisions. *Trans. ASME: J. Fluid Engng* **121** (1), 179–184.